2016

Physics-based and Data-driven Methods with Compact Computing Emphasis for Structural Health Monitoring

Golnaz Shahidi
Lehigh University

Physics-based and Data-driven Methods with

Compact Computing Emphasis for Structural Health Monitoring

By

S. Golnaz Shahidi

Presented to the Graduate and Research Committee

of Lehigh University

in Candidacy for the Degree of

Doctor of Philosophy

in

Structural Engineering

Lehigh University

May 2016

DISSERTATION SIGNATURE SHEET

Approved and recommended for acceptance as a dissertation in partial fulfillment of the requirements for the degree of Doctor of Philosophy.

_____
Date

_____
Dr. Shamim N. Pakzad

_____
Dr. John L. Wilson

_____
Accepted Date

Committee Members:

_____
Dr. Clay J. Naito

_____
Dr. Dan M. Frangopol

_____
Dr. Leon Lai

Acknowledgements

The research described in this dissertation was conducted at the Research Center for Advanced Technology for Large Structural Systems (ATLSS), Department of Civil and Environmental Engineering, Lehigh University, Bethlehem, PA. The funding for the research was partially provided by Pennsylvania Infrastructure Technology Alliance (PITA) and National Science Foundation. This financial support is gratefully appreciated.

First and foremost, I wish to express my gratitude to my PhD advisor, Dr. Shamim Pakzad, for his knowledge, guidance, and constructive suggestions during my studies at Lehigh. I would also like to thank Dr. John Wilson, my co-advisor, for the assistance he provided at all levels of my graduate program. A very special thanks goes out to Dr. James Ricles for his invaluable advice and insightful discussions during our collaboration on the Washington Monument project. I also appreciate the time and suggestions of the members of my PhD committee, Dr. Clay Naito, Dr. Dan Frangopol, and Dr. Leon Lai throughout these years.

I would like to thank Peter Bryan for all of his computer and technical assistance, and my fellow graduate students for their help and support. The support provided by Darrick Fritchman and the ATLSS laboratory technical staff is much appreciated.

I am deeply grateful to my parents and my sister for the support they provided me through my entire life from near and far, and last but not least, I would like to thank my husband and best friend, Mohsen, for his patience, love, and encouragement.

Table of Contents

Table of Figures

Abstract

This doctoral dissertation contributes to both model-based and model-free data interpretation techniques in vibration-based Structural Health Monitoring (SHM). In the model-based category, a surrogate-based finite element (FE) model updating algorithm is developed to improve the computational efficiency by replacing the FE model with Response Surface (RS) polynomial models in the optimization problem of model calibration. In addition, formulation of the problem in an iterative format in time domain is proposed to extract more information from measured signals and compensate for the error present in the regressed RS models. This methodology is applied to a numerical case study of a steel frame with global nonlinearity. Its performance in presence of measurement noise is compared with a method based on sensitivity analysis and it is observed that while having comparable accuracy, proposed method outperforms the sensitivity-based model updating procedure in terms of required time. With the assumption of Gaussian measurement noise, it is also shown that this parameter estimation technique has low sensitivity to the standard deviation of the measurement noise. This is validated through several parametric sensitivity studies performed on numerical simulations of nonlinear systems with single and multiple degrees of freedom. The results show the least sensitivity to measurement noise level, selected time window for model updating, and location of the true model parameters in RS regression domain, when vibration frequency of the

system is outside the frequency bandwidth of the load. Further application of this method is also presented through a case study of a steel frame with bilinear material model under seismic loading. The results indicate the robustness of this parameter estimation technique for different cases of input excitation, measurement noise level, and true model parameters

In the model-free category, this dissertation presents data-driven damage identification and localization methods based on two-sample control statistics as well as damage-sensitive features to be extracted from single- and multivariate regression models. For this purpose, sequential normalized likelihood ratio test and two-sample t-test are adopted to detect the change in two families of damage features based on the coefficients of four different linear regression models. The performance of combinations of these damage features, regression models and control statistics are compared through a scaled two-bay steel frame instrumented with a dense sensor network and excited by impact loading. It is shown that the presented methodologies are successful in detecting the timing and location of the structural damage, while having acceptable false detection quality. In addition, it is observed that incorporating multiple mathematical models, damage-sensitive features and change detection tests improve the overall performance of these model-free vibration-based structural damage detection procedures.

In order to extend the scalability of the presented data-driven damage detection methods, a compressed sensing damage localization algorithm is also proposed. The objective is accurate damage localization in a structural component instrumented with

a dense sensor network, by processing data only from a subset of sensors. In this method, first a set of sensors from the network are randomly sampled. Measurements from these sampled sensors are processed to extract damage sensitive features. These features undergo statistical change point analysis to establish a new boundary for a local search of damage location. As the local search proceeds, probability of the damage location is estimated through a Bayesian procedure with a bivariate Gaussian likelihood model. The decision boundary and the posterior probability of the damage location are updated as new sensors are added to processing subset and more information about location of damage becomes available. This procedure is continued until enough evidence is collected to infer about damage location. Performance of this method is evaluated using a FE model of a cracked gusset plate connection. Pre- and post-damage strain distributions in the plate are used for damage diagnosis.

Lastly, through study of potential causes of damage to the Washington Monument during the 2011 Virginia earthquake, this dissertation demonstrates the role that SHM techniques plays in improving the credibility of damage assessment and fragility analysis of the constructed structures. An FE model of the Washington Monument is developed and updated based on the dynamic characteristics of the structure identified through ambient vibration measurement. The calibrated model is used to study the behavior of the Monument during 2011 Virginia earthquake. This FE model is then modified to limit the tensile capacity of the grout material and previously cracked sections to investigate the initiation and propagation of cracking in several futuristic earthquake scenarios. The nonlinear FE model is subjected to two

ensembles of site-compatible ground motions representing different seismic hazard levels for the Washington Monument, and occurrence probability of several structural and non-structural damage states is investigated.

Chapter 1

Introduction

In-service structural systems are inevitably prone to deterioration and damage with use, time, and in many cases due to extreme events happening throughout their lifetime. Therefore, Structural Health Monitoring (SHM) research community aims to develop methodologies that allow fast and easy - and ultimately automated - condition assessment of structures in order to maximize the probability of detection of structural damage in its early stages and minimize the restoration and maintenance costs. For this purpose several non-destructive techniques (Trimm 2003) have been established over past decades ranging from visual inspection (Balageas 2006) to more advanced methods such as ultrasonic testing (Yehia et al. 2007), acoustic emission (Carpinteri et al. 2011), and vibration-based methods (Doebling et al. 1998). In monitoring of civil structures and infrastructure systems, vibration-based methods have attained significant attention in recent decades. The reason is manifold, to mention a few:

- unlike other methods, vibration-based SHM techniques are not restricted to have direct access to the location of damage (Trimm 2003)
- with advancement in the sensing technology, vibration measurement of large-scale structure can be completed with a reasonable budget (Kim et al. 2007)

- these methods seem more promising for development of a general automated SHM framework (Magalhaes et al. 2012)

Vibration-based SHM includes instrumentation, response measurement, data processing, and interpretation. Key components of SHM techniques in processing the monitoring vibration data fall into three categories: (1) identification of dynamic characteristics of the monitored structures, (2) detection, localization, and quantification of the damage in the system, and (3) updating the finite element (FE) simulations of the structures based on their measured responses.

While two or more of these methods commonly contribute in monitoring projects, each of these components offer unique benefits in understanding the structural characteristics and behavior. Therefore, research in all three aspects is ongoing to develop methodologies that are efficient and applicable to a wide range of structural systems. FE calibration methods attracted significant attention in the recent decades, mainly because having a FE model calibrated with reference to the actual structure, enables a variety of applications such as futuristic reliability study, assessment of retrofit alternatives, and designing structural control strategies. Moreover, parameter estimation through model calibration serves as the basis for many model-based damage detection algorithms which aim to assess the structural damage in a more objective way than non-parametric damage detection procedures.

Structural damage detection is one of the main goals of SHM projects. Over last decades numerous vibration-based algorithms have been proposed to fulfill this goal.

These techniques can be classified based on their damage indicators (local/global), or their approaches (physics-based or data-driven). While physics-based approaches seem more appropriate for in-depth investigation of behavior of a particular structure, low computational demand associated with the data-driven approaches make them more suitable for developing automated damage localization frameworks and dealing with ever-growing volumes of monitoring data.

1.1. Scope of the research

This doctoral dissertation contributes in two of the main components of vibration-based SHM data interpretation methods: FE model updating and data-driven damage detection.

A surrogate-based FE model updating algorithm is developed to improve the efficiency of model updating techniques. While this algorithm is developed to update non-linear FE models in time domain, the overall framework is applicable to structures with linear or non-linear behavior. Efficiency of this method is compared with sensitivity-based FE model updating. Moreover, robustness of the algorithm with respect to the frequency content of the input excitation and noise in the measurement is studied. Furthermore, application of this method in updating the FE model of the Washington Monument is demonstrated.

Second contribution of this dissertation is in model-free damage detection techniques, specifically in establishing and comparing the effectiveness of several data-driven damage indicators and statistical tests for SHM applications. The

comparison is performed on a scaled steel frame tested in the laboratory of Advanced Technology for Large Structural Systems (ATLSS) at Lehigh University. In addition, a compressed sensing damage detection algorithm is proposed that process minimum amount of data from a dense sensor network to accurately localize the structural damage. Application of this compressed damage localization technique for single and multiple damage cases are demonstrated through FE simulations of a steel gusset plate connection.

Lastly, through study of potential causes of damage to the Washington Monument during the 2011 Virginia earthquake, this dissertation demonstrates the role that SHM techniques plays in improving the credibility of damage assessment and fragility analysis of the constructed structures.

1.2. Organization of the dissertation

Chapter 2 of this dissertation presents a review of the existing literature on finite element model (FEM) updating and damage detection.

Chapter 3 describes the developed algorithm for non-linear model updating in time-domain. Performance of this algorithm is validated numerically through an example of a scaled steel frame.

Chapter 4 investigates the robustness of the model updating methodology presented in chapter 3 with respect to input excitation and measurement noise. For this purpose, several sensitivity studies were performed on structures with single and

multiple degrees of freedom. Robustness estimation is investigated in scenarios where structure is excited with harmonic as well as seismic loading.

Chapter 5 describes a study conducted to investigate the potential causes of damage to the Washington Monument following the 2011 Virginia earthquake.

Chapter 6 describes contributions of this research in the model-free methods in structural damage detection.

Chapter 7 presents the proposed damage detection methodology with compact sensing approach.

Chapter 8 concludes the dissertation with a summary of the presented research, conclusions, and future work.

Chapter 2

Literature Review

Over recent decades numerous vibration-based structural damage detection techniques have been proposed that can be classified based on the features they interpret as damage indicators and/or their approaches (physics-based or data-driven). In physics-based (also called model-based) procedures, selected parameters of an FEM of the system are updated with respect to the measured responses to identify the existence and extent of the structural damage (Jaishi and Ren (2007); Kim and Kawatani (2008);Weber and Paultre (2010); Moaveni et al. (2012)). On the other hand, data-driven (also called model-free approaches) use the measured responses directly in numerical algorithms so that there is no need for prior information about the structure's properties or suspected location of damage (Bodeux and Golinval (2003); Lu and Gao (2005); Deraemaeker and Preumont (2006); Kumar et al. (2012)).

There are advantages and disadvantages about each category of methods. The model-based methods are usually more laborious to implement and require certain a priori knowledge of structural properties, and location of damage; however, these methods are more objective in the interpretation of their results. In addition, the calibrated model can be used for design of repair scenarios or estimating the remaining life of the damaged structure. The main advantage of the second group is their

efficiency, and that they can be readily applied to measured signals without any prior information. This property has made them more suitable in analyzing the data from dense sensor networks to identify relatively localized damage; a scenario in which a model-based algorithm can hardly perform successfully within reasonable computational effort. Moreover, the application of the data-driven methods as a general automated damage detection platform is more promising. One the other hand, these model-free techniques would be ineffective without statistical analyses to determine a change threshold for the extracted features.

Another classification for SHM damage detection methods is based on the features that are used to monitor the condition of the structures. Modal parameters (vibration frequencies, mode shapes, mode shape curvatures, etc.) have been widely used as damage sensitive features in the SHM field (West (1984); Pandey and Biswas (1995); Doebling et al. (1998)). However, since these damage indicators are global in nature, they are generally unable to detect local damages (Farrar et al. (1994)). Additionally, they require measurement data with high signal to noise ratio as well as moderate damage levels to identify the damage in the system (Farrar et al. (1994); Alvandi and Cremona (2006)). Research is still ongoing to extract features from structural responses that are sensitive enough to local and minor damage, yet robust to the common changes in the structural responses and measurement noise. Examples of such damage indicators are statistical features generated from sensor networks data (Nair et al. (2006); Figueiredo et al. (2011); Kiremidjian et al. (2011); Yao and Pakzad (2013); Dorvash et al. (2013a)). Such features seem more promising for applications

on in-service structures, as with the recent advancement in sensing technology, literature reports numerous successful implementations of sensor networks on large-scale structures (for example, Lynch et al. (2006); Cruz and Salgado (2009); Pakzad (2010); Jang et al. (2011); Labuz et al. (2011); Hu et al. (2013))

The contribution of this dissertation is in both categories of model-based and model-free methods in SHM. In the model-based category, a surrogate-based model updating technique is proposed for efficient calibration of non-linear FEMs, and in the second category, model-free damage identification and localization methods based on two-sample control statistics are presented. In addition, these data-driven techniques are also extended to consider compressed damage localization, when the system is monitored using a dense sensor network.

Next sections review the related literature in the area of non-linear FEM updating and data-driven damage localization.

2.1. Finite Element Model Updating

Finite element model updating is an inverse problem of modifying the uncertain parameters of a FE model in order to improve the correlation between certain analytical response features and their experimental counterparts. Over recent decades several computational procedures have been developed to update parameters of analytical models based on experimental results. These procedures can be categorized according to their domain of applicability. In linear model updating experimentally identified modal quantities (mainly natural frequencies and mode shapes) are used as

reference features to update finite element models of structures (Bell et al. 2007; Zimmerman and Lynch 2009; Weber and Paultre 2010; Moaveni and Behmanesh 2012; Moaveni et al. 2012). This technique is widely used especially with improvement of sensing technology and rapid deployment of wireless sensor networks in recent decades which made it more convenient to obtain valuable information about behavior of in-service structures (Lynch et al. 2003; Lynch and Kenneth 2006 ; Whelan and Janoyan 2009; Zaurin and Catbas 2010 ; Jang et al. 2011; Dorvash et al. 2012). Direct and iterative methods for linear model updating are well-documented in the literature (Imregun and Visser 1991; Friswell and Mottershead 1995). In direct methods as the elements of the structural matrices are updated in one step, the structural connectivity may be violated and make it difficult to interpret the updated matrices (Baruch 1978; Baruch 1984; Berman and Nagy 1983; Friswell et al. 1998; Yang and Chen 2009). Therefore, iterative model updating methods which directly modify the preselected parameters of FE models are more popular (Brownjohn and Xia 2000; Zhang et al. 2000; Brownjohn et al. 2001; Jaishi and Ren 2006; Hua et al. 2009; Wang et al. 2010; Ribeirio et al. 2012; Zona et al. 2012). These techniques are mainly based on the sensitivity analysis and linearization of the generally non-linear relationship between measured responses and the uncertain model parameters (Mottershead et al. 2010). Such methods are generally computationally intensive, and may cause convergence difficulties since they are based on iterative determination of local gradients (Ren and Chen 2010). Moreover, in the presence of any non-linearity in the structure the procedures based on modal information fail to yield the parameters associated with non-linear behavior of the model and other measures are required to

update the model. Silva et al. (2009) performed a comparison between different metrics for use in non-linear model updating using vibration test data and concluded that such metrics are effective in updating the structural models with local and weak non-linearities. Therefore, our objective is to present a procedure to overcome these problems in updating non-linear systems.

One of the proposed approaches to decrease the computational effort in model updating problems is to replace the FE model with a mathematical expression which approximates the relationship between pre-selected inputs and output of the FE models. This approach was successfully implemented in the structural optimization problems where function approximations reduce the cost of function evaluations to find the global optimum of the problem (Roux et al. 1998; Heinonen and Pajunen 2011). In FEM updating, the parameters of the surrogate model are directly modified with respect to the measured data. One of the commonly used surrogate models are polynomial functions constructed based on Response Surface (RS) methodology which is originally a statistical method for exploring the relation of explanatory variables of a system and its responses. To find a mathematical model to represent this relationship, there are several subsets that can be chosen from the entire design space. Techniques of design of experiments (DOE) can be employed to provide specific designs consisting of limited number of points in the whole design space with reasonable distribution under the assurance of modeling accuracy (Box and Draper 1987; Montgomery 2001). This method is promising in modifying FE model parameters. Guo and Zhang (2004) and Ren and Chen (2010) present studies of

comparison between RS-based and Sensitivity-based linear model updating techniques. They found that while the RS-based method gives likewise accurate predictions, it requires far fewer number of FE analyses and the rate of convergence is significantly higher. Zhang et al. (2005) concluded that RS modeling considerably decreases the computational effort regarding implementation of genetic algorithm for model updating. The results of application of this procedure on a numerical case study revealed that unlike the sensitivity-based method, RS-based genetic algorithm model updating successfully reached the global optima. Marwala (2004, 2010) present a comparison of the computational expense and accuracy of RS based FE model updating with methods using evolutionary optimization algorithms on full FE model for updating. This study implements a genetic algorithm to optimize multilayer neural-network based RS models in two case studies of a linear beam and a linear unsymmetrical H-shaped structure. Comparison of the results concluded that the proposed method requires the least computational load, while the predicted modal properties are of the same order of accuracy as those obtained by simulated annealing and genetic algorithm.

While in the previous studies, designs such as central composite and d-optimal were used to generate the input levels for RS modeling, Ren et al. (2011) demonstrated that for complex structures with large number of uncertain parameters uniform design economizes the computation of constructing RS models.

The application of RS-based model updating has been also studied for damage detection. Cundy (2002) applied this method on damage identification of a simulated

mass–spring–damper system and a tested cantilever beam in the laboratory. The study found that damage identification using RS modeling is successful in locating damage and quantifying its severity with some degree of accuracy and robustness to the experimental variability (i.e. noise). Fang and Perera (2009) presented a systematic structural damage identification technique based on RS methodology comprising four sequential steps of feature selection, parameter screening, primary RS modeling and updating of the intact and damaged structures.

There are few examples of application of RS-based model updating in the literature for structures with non-linearities. Schultze et al. (2001) introduced a new approach called feature extraction for parameter selection in model updating problems based on 2^k factorial design. This approach was used to select the significant parameters to update a model consisting of a cylindrical steel impactor and a foam layer assembled on a mounting plate attached to a drop table under impact on a concrete floor. Quadratic RS models were then used to estimate the response features to update the selected parameters of the model. Zhang and Guo (2007) proposed a model updating procedure based on Principal Component Decomposition and RS method to update a frame model with thin wall components showing strain-rate-dependence non-linearity under impact test.

2.2. Data-driven Structural Damage Detection

Another contribution of this dissertation is in presenting model-free (i.e. Data-driven) damage identification and localization methods based on two-sample control

statistics. In such data-driven methods, first time series analysis or signal processing techniques are employed to extract damage sensitive feature from measured signals. Choosing an effective damage feature is crucial for successful damage detection. These features can be used to establish control statistics which were originally used to monitor a change in a process. Once a significant change is encountered in the process (here the damage indicators), the control statistic can capture this change with the use of a threshold value. Once the threshold value is crossed, the process can be deemed out of control. These charts can be used to compare the choice of damage sensitive features in damage detection schemes because different features will have different sensitivities and produce different damage detection and localization results.

There are many different parameters that have been used by researchers as damage sensitive features for model-free damage detection. In order to find and use dynamic characteristics of a structure as damage features, Huang (2001) proposed a procedure that uses the multivariate AR model for numerical simulations of a six-story shear building subjected to white-noise and low-pass filtered white-noise input, while simulated acceleration and velocity responses were used in separate scenarios to study the effect of signal type. Similarly, He and De Roeck (1997) uses multivariate autoregressive models to find the modal parameters of a water transmission tower from measured acceleration responses during ambient vibration. Furthermore, Hung et al. (2004) identifies modal parameters from measured input and output data using a vector backward autoregressive with exogenous model. This method was experimentally validated using measured acceleration responses of a five-story scaled

steel frame under a shake table test. Zheng and Mita (2007) fit Auto regressive moving average (ARMA) models to the time series of acceleration responses of the structure and use the distance between the ARMA models to detect the existence of the damage, which is consequently localized by minimizing the cross-correlation of multiple excitations through pre-whitening filtering. Gul and Catbas (2011) create ARX models based on acceleration responses of different sensor clusters of the healthy structure, these models are then used for predicting the data from the damaged structure, while the difference between the fit ratios are used as damage sensitive features. Effectiveness of autoregressive models are investigated in several other studies by using the time history of acceleration responses of the system to generate damage indicators (for example, Fugate et al. (2001); Nair et al. (2006); Zheng and Mita (2009); De Lautour and Omenzetter (2010) ; Dorvash et al. (2013b)); however, there are also successful applications of these models for damage localization in the literature which use time histories of measured strain signals (Sohn et al. (2001); Noh et al. (2009); Dorvash et al. (2013c)). While some of these studies use data from real-world systems for validation (Sohn et al. (2001); Gul and Catbas (2011)), most of the proposed damage detection techniques are verified through laboratory testing of specimens with different levels of complexity from retrofitted reinforced concrete column (Fugate et al. 2001) to four–story two-bay by two-bay steel braced frame (Nair et al. 2006).

After extracting the damage features from the signals measured over time, significance of variation in the features should be examined to distinguish any change

that is outside the range of random variation of measurements. For this purpose, there are several types of control statistics that can be used for change point detection (Amiri and Allahyari 2011). These statistics can be used to detect a single change or multiple changes in the mean or variance of the feature vectors. One of the first charts generated, the standard univariate Shewhart $\bar{X}$ control chart, was introduced in 1924 by Walter Shewhart to detect a change in the mean of a population (Wilcox 2003). Since then, control schemes have found widespread application in different disciplines and become more effective. Fugate et al. (2001) is an example of application of Shewhart control chart in damage detection of a concrete bridge column. One major flaw in using univariate control statistics is that they can only monitor one variable at a time. If one were to observe a set of quality characteristics that have components with the potential to be interrelated, the univariate control schemes become obsolete. Although it could be argued that univariate control charts could be applied independently to each component of the multivariate data, misleading results may be obtained in some cases due to failure to allow for the inherent relationship among the components of the multivariate data (Zamba and Hawkins 2006). Therefore, in this research muliti-dimensional damage features are condensed into a single feature to develop univariate control statistics.

One control chart used in this study is a Likelihood Ratio Test (LRT) of which there are many types. Srivastava and Worsley (1986) propose a form of the LRT that is more effective in detecting a shift involving only the mean vector, while other researchers present improved LRT-based statistical methods capable of detecting

shifts in the mean and variance of a vector of observations (Sullivan and Woodall (1996); Hawkins and Zamba (2005); Zhang et al. (2010); Zhou et al. (2010)). Zou et al. (2006) presents a control chart based on change point models for monitoring the intercept, slope or standard deviation of the linear profiles and names the proposed method the standardized likelihood ratio test. The literature related to application of such change point techniques for structural damage detection is scarce (El-Ouafi Bahlous et al. 2007). This dissertation uses the Normalized Likelihood Ratio Test (NLRT) from Sullivan and Woodall (1996), which has not been used in SHM schemes. The details of this method are presented in the next section.

Another change point analysis used in the present research is based on a two-sample t-test; a form of statistical hypothesis testing to distinguish significant differences in the means of two sets of data. Montegomery and Loftis (1987) show the applicability of this t-test for detecting trends in water quality variables. Additionally, Hawkins and Zamba (2005) use the t-test in conjunction with the generalized likelihood ratio test in order to distinguish between a shift in the mean and the variance in a gold mining quality control example. In effect, there are many different variations of such statistical tests that can be used based on different initial assumptions about the mean and variance of the data. For example, the Satterthwaite-Welch method (Welch 1974) is used with the assumption that the variance of the two populations is unknown and unequal. However, in this research, the Student's t-test is used in which it is assumed that the variance of the two populations is unknown but equal.

Chapter 3

Generalized Response Surface Model Updating Using Time Domain Data

The objective of this chapter is to present a procedure to construct accurate yet less computationally demanding surrogate models to replace FE models in non-linear model updating problems. For this purpose, RS model updating is used and extended into non-linear FE updating through time domain data. FE model updating using RS modelling consists of two main steps: first, a polynomial model is constructed based on a finite number of FE runs. Then, the objective function in the form of the residuals of measured responses and corresponding RS models is optimized. However, the solution of optimization procedure is not reliable unless the RS model regressed in the first step is able to predict the response of FE model well. Therefore, the main issue regarding construction of RS models is how to create accurate surrogate models. The number of levels for each parameter and also the order of RS polynomial models result in models with different accuracy. Consequently, the procedure for finding an appropriate design to build the surrogate model in regard with the nature of problem requires a number of trials and errors with different designs and subset models. Such procedures increase the computational cost associated with RS modeling, as the cost of a RS model depends on the total number of FE runs required to achieve the desired

accuracy. Several design families are available such as full factorial, fractional factorial, central composite design, Box Behnken design, etc (Montgomery 2001). Full factorial design consists of all possible combinations of levels of parameters. Other designs are mainly based on a subset of design points sampled from a full factorial design. Figure 3.1 displays the design points of three different designs for a problem with three model parameters. This figure shows that full factorial, Box Behnken and central composite designs have 27, 15 and 20 design points respectively. It is seen that while full factorial design contains more design points, it is beneficial in uniformly sampling from the corners of the domain as well as the central area. In this study a systematic procedure is proposed to sample the design points in the domain of model parameters which adopt a full factorial design with minimum number of levels for each parameter followed by adding design points to the domain when required after evaluation of the regressed RS models.

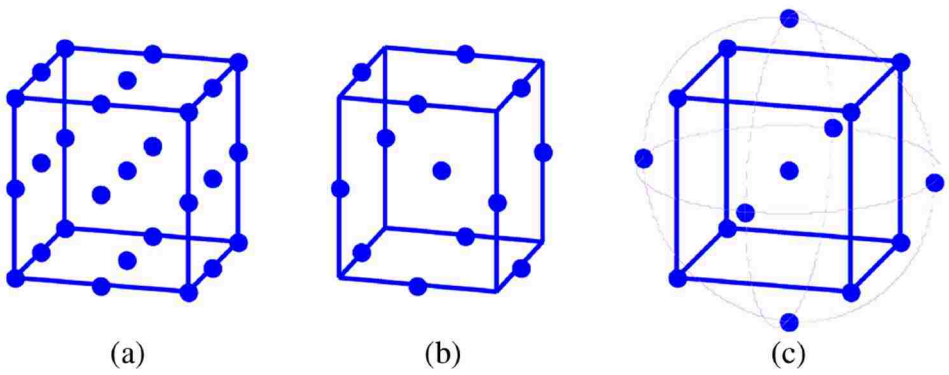

Figure 3.1. Full factorial (a), Box Behnken (b) and central composite (c) design for a model with three parameters

Another issue appears in using pre-defined designs while dealing with the bounds of the variables in the optimization problem. It should be noted that the regressed RS

model can only replace the FE model in the joint region of the input data used in the regression (Montgomery et al. 2004). In many of the experimental designs, not all levels of the parameters are present in the design; therefore, updating the RS model in the original regions of model parameters can cause extrapolation beyond the regression domain. Figure 3.2 illustrates the original and joint region of parameters for a model with two parameters. The figure shows that while both points A and B are in the area made by original regions of model parameters, point A is outside of the regression domain. To prevent this phenomenon, called the hidden extrapolation, another constraint should be imposed on the optimization problem to specify the infeasibility of the solution outside the joint region of the variables.

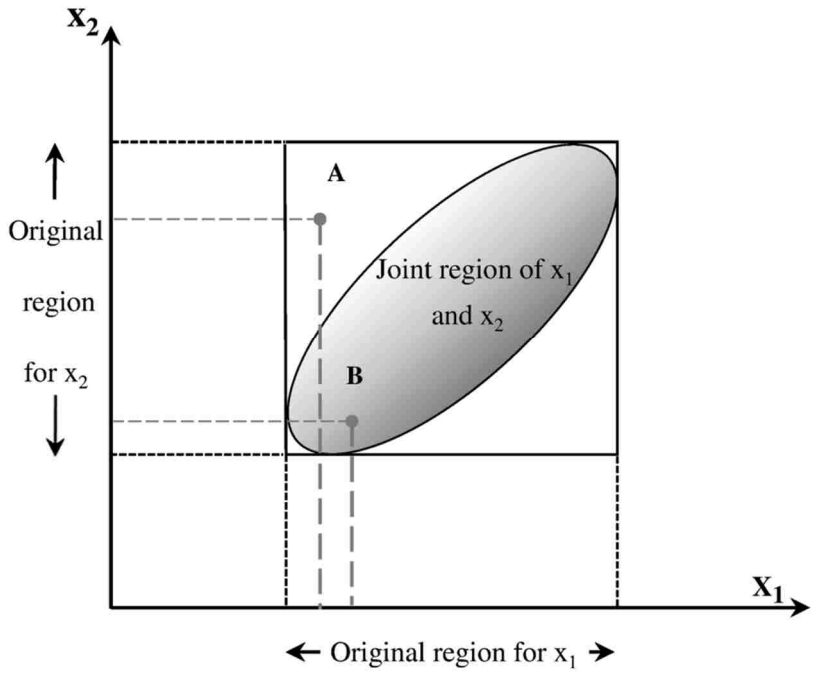

Figure 3.2. An example of extrapolation in multiple regression

In this chapter, a procedure is proposed for designing the levels of input parameters and constructing the RS model. Since the proposed procedure is based on the full factorial design of parameters, it addresses the hidden extrapolation problem by expanding the joint region of parameters into a set containing the original regions of all the parameters. This method results in a RS model capable of generating the response of FE model analysis in a specific domain of input variables. Furthermore, it is also proposed to formulate and solve the optimization problem of model modification through time history of responses iteratively. This approach is beneficial in extracting more information from the measured experimental signals as opposed to the traditional approaches in which the whole measured signals are summarized into one or more response features. Another advantage of this approach is that it is not limited to the type of model behavior or analysis. It can be applied to linear or non-linear models under static or dynamic analysis.

3.1. Generalized Response Surface Model Updating

To provide the model updating process with more information from measured data, it is proposed to update FE models through time history of measured responses. The experimental input force is used to generate the equivalent responses of FE model at different levels of the model parameters. In every time step a RS model is constructed to produce the corresponding response of the FE model at that time step

$$RS_l = h_l(\Theta) \tag{3.1}$$

Eq. (3.1) denotes the generalized RS model at the l^{th} time step, where h is the polynomial surrogate model in that time step and Θ represents a vector of model parameters selected for modification. By completing this process for every response, an objective function is formulated to minimize a function of residuals of RS-based and experimental response features at every time step. Eq. (3.2) represents this minimization problem which should be solved inside the domain of model parameters.

$$\min_{\theta} \; f_l(H_l(\Theta), Y_{\exp l}) \tag{3.2}$$

In Eq. (3.2) H_l and $Y_{\exp l}$ are vectors containing all the surrogate models and corresponding experimental responses at the l^{th} time step.

Prior to RS modeling, the appropriate design and model order should be found so that the regressed RS models are accurate at the associated time steps. The computational procedure proposed here to construct accurate RS models and update them in time domain is called *Generalized Response Surface Model Updating (GRSMU)* (Shahidi and Pakzad 2014a). This method is categorized into three parts: model construction, evaluation, and optimization. The next subsections describe these three steps in detail.

3.2. RS Model Construction

The steps of model construction and evaluation are completed for each time step to find appropriate levels and order of the RS models. To start RS modeling, an initial region for the pre-selected uncertain parameters of the FE model should be chosen. This region, in which the FE model is replaced by the RS model, is called *RS domain*. To regress the polynomial RS models, a number of points are sampled in the RS domain based on full factorial design of the model parameters. The regression model in matrix notation for the l^{th} time step is given by

$$y_l = X\beta_l + \varepsilon_l \qquad (3.3)$$

$$\text{where } X = [x_1, x_2, ..., x_n]$$

In Eq. (3.3) y_l is $n \times 1$ vector of observations at the l^{th} time step of the history of response y and $x_i = g(\theta_{i1}, \theta_{i2}, ..., \theta_{im}) = [1 \;\; x_{i1} \;\; x_{i2} \;\; ... \;\; x_{ik}]$ is $1 \times (k+1)$ row vector mapped to the i^{th} design point by vector-valued function g. $(\theta_{i1}, \theta_{i2}, ..., \theta_{im})$ denotes the domain of g as $m \times 1$ vector of the updating parameters and x_{ij} in general is a polynomial function of one of the updating parameters at the i^{th} design point. β_l is $(k+1) \times 1$ vector of regression coefficients and ε_l is $n \times 1$ vector of random errors corresponding to the l^{th} time step. Parameters *m*, *n* and *k* are the number of the updating parameters, the design points in the RS domain and the terms included in the RS models, respectively.

The RS model construction starts with a full factorial design with three levels for each parameter. FE model with the parameters of each design point is analyzed repeatedly to generate y_l vector in Eq. (3.3) which is the vector of FE model responses corresponding to the experimental ones at the l^{th} step of the time history of y. The regression begins with including linear terms of the updating parameters in the RS models. The regressed RS model associated with the l^{th} time step approximates the response of the FE model at that time step for any points inside the RS domain

$$RS_l(\theta_{01}, \theta_{02}, ..., \theta_{0m}) = x_0 \hat{\beta}_l \tag{3.4}$$

In Eq. (3.4), $x_0 = g(\theta_{01}, \theta_{02}, ..., \theta_{0m}) = [1 \quad x_{01} \quad ... \quad x_{0k}]$ is the vector of polynomial terms included in the RS model at a point inside the RS domain with coordinates $(\theta_{01}, \theta_{02}, ..., \theta_{0m})$. $\hat{\beta}_l$ is the least square estimator of the regression coefficients at the l^{th} time step (Montgomery et al. 2004; Kariya and Karuta 2004; Johnson and Bhattacharyya 2009). The regressed RS model prior to replacing the FE model should be evaluated in terms of adequacy of the fit and predictability of the response with respect to the new data.

3.3. RS Model Evaluation

One of the objectives of *GRSMU* is to find polynomial models capable of approximating the FE model responses with good accuracy while having minimum design points and model order. Therefore, model construction begins with regressing linear RS models onto a design space containing three levels for each parameter and

the performance of the regressed models are checked. If the RS models are not accurate enough to substitute the FE model throughout the entire time history, the sampled design points and model order will be changed.

Initially the performance of the RS models is checked at the design points. For this purpose $e_l = X\hat{\beta}_l - y_l$ the residuals of the RS and FE models at the l^{th} time step is calculated. Large residuals indicate that the regression is not successful at the design points.

The overall adequacy of the RS models can be further evaluated by adjusted R^2 statistics. This parameter is used to measure the effect of adding new variables to the model. As more terms are added to the model, unadjusted R^2 always increases regardless of the degree of the contribution of the additional variables. In contrast, adjusted R^2 will only increase by adding a variable to the model if the addition of that variable adds to the explanatory power of the regression model (Montgomery et al. 2004). Use of such statistics is common in validation of the regressed polynomial RS models in FE model updating (Zhang and Gue (2004, 2007); Fang and Perera 2009; Ren and Chen 2010; and Ren et al. 2011). Eq. (3.5) gives R^2_{adj} statistics for the RS model regressed at the l^{th} time step of the analysis.

$$R^2_{adjl} = 1 - \frac{SS_{\mathrm{Re}sl}/(n-k-1)}{SS_{Tl}/(n-1)} \tag{3.5}$$

where $SS_{\mathrm{Re}sl} = y_l^T y_l - \hat{\beta}_l^T X^T X \hat{\beta}_l$ and $SS_{Tl} = y_l^T y_l - \frac{(\sum_{i=1}^{n} y_{il})^2}{n}$

In Eq. (3.5) $SS_{\mathrm{Res}l}$ and SS_{Tl} are residual and total sum of squares in the l^{th} time step. SS_{Tl} measures the variation in the response of the FE model about the mean value and $SS_{\mathrm{Res}l}$ indicates the variation in the response that the regressed RS model fails to explain. Since in Eq. (3.5) $SS_{Tl}/(n-1)$ is constant regardless of how many variables were included in the model, $R^2_{\mathrm{adj}l}$ increases if the additional variables reduce the term $SS_{\mathrm{Res}l}/(n-k-1)$. If $R^2_{\mathrm{adj}l}$ is close to one, it implies a perfect regression. Therefore, when $R^2_{\mathrm{adj}l}$ is much smaller than one, the RS model is not accurate in estimating the FE responses at the design points. After completing R^2_{adj} calculation through the time domain history, if the regressed RS models are not fitted well to the design points, higher order terms of the model parameters should be added to the RS models and the model evaluation repeated.

After finding the appropriate model order, the prediction quality of the RS models should be checked. For this purpose, residuals are calculated at points that did not contribute in the regression. These points, which are called intermediate points, are sampled from RS domain in different sets. Each set represents the intermediate levels for one parameter. To sample a set of new points corresponding to a parameter, one of the original data points is replicated, and then the selected parameter is replaced by the average of one pair of its original levels. Intermediate points which result in larger residuals than the original design points indicate that although the RS model has been fitted well to the original data, it cannot predict the FE responses for new points. Therefore, the design of levels of parameters should become finer. As the same design

and model order is used throughout the entire time history, the maximum normalized residuals are compared at original and intermediate levels all through the time history. Since the intermediate design points of each parameter are generated with the constant values for other parameters in that set, the decision of adding more levels to the design is made for each parameter separately and the design space will not get populated blindly.

By repeating this procedure, the appropriate RS model with high quality in regression and prediction is constructed for every time step of the data. This procedure is completed for every response feature. It should be noted that by implementing this algorithm, the RS models of all the response features at all the time steps can be constructed and evaluated simultaneously.

3.4. RS Model Optimization

Iterative model construction and evaluation results in construction of an accurate RS model for the measured response in every time step. The optimization problem is, then, formulated and solved at every time step leading to histograms of the updated parameters. Eq. (3.6) formulates the optimization problem corresponding to the l^{th} time step subjected to the constraints regarding the bounds of parameters in RS domain.

$$\begin{aligned} &\min_{\theta_j} \quad f_l = \sqrt{\sum_{i=1}^{s} \left(\frac{RS_{il}(\theta_1, \theta_2, \ldots, \theta_m) - y_{\exp il}}{y_{\exp il}}\right)^2} && i = 1,2,\ldots,s \\ &s.t. \quad \theta_{jlb} \le \theta_j \le \theta_{jub} && j = 1,2,\ldots,m \end{aligned} \tag{3.6}$$

In Eq. (3.6) $RS_{il}(\theta_1, \theta_2, ..., \theta_m)$ denotes the RS model built for the l^{th} time step and the i^{th}response feature and $y_{\exp il}$ is the i^{th}response measured at the l^{th} time step. By formulating the FE model updating in this explicit format, the problem can be solved using any optimization algorithm for non-linear constrained systems.

Figure 3.3 presents *GRSMU* in a flowchart. RS model construction and evaluation are completed in the time domain to find the proper design and model order. Then the accurate RS models are regressed and the optimization problem is solved for every time step. The optimization step can be repeated in a smaller region for model parameters based on the results of the first round of minimization. Using the design and polynomial functions established in the first cycle, only the following steps are needed: (1) generate the FE responses for new levels; (2) fit the new RS models through the time history; and (3) optimize the new objective function iteratively. These steps are illustrated by the highlighted blocks in Figure 3.3. The procedure can be repeated until the variation of updated parameters falls within the desired threshold. When the analysis is static, the steps of model construction and evaluation are completed once, and the optimization step is done through the time history of the measured data. It should be noted that shrinkage of the RS domain is an extension to the optimization step to achieve more accurate estimates for the updated parameters. To avoid inefficient computations, this extension should be performed in cases that the updated parameters are not accurate enough. This can be assessed by using the statistical inferences drawn from the histograms of the updated parameters as input to

the finite element model and investigating the correlation of the corresponding responses of the model with the measured results.

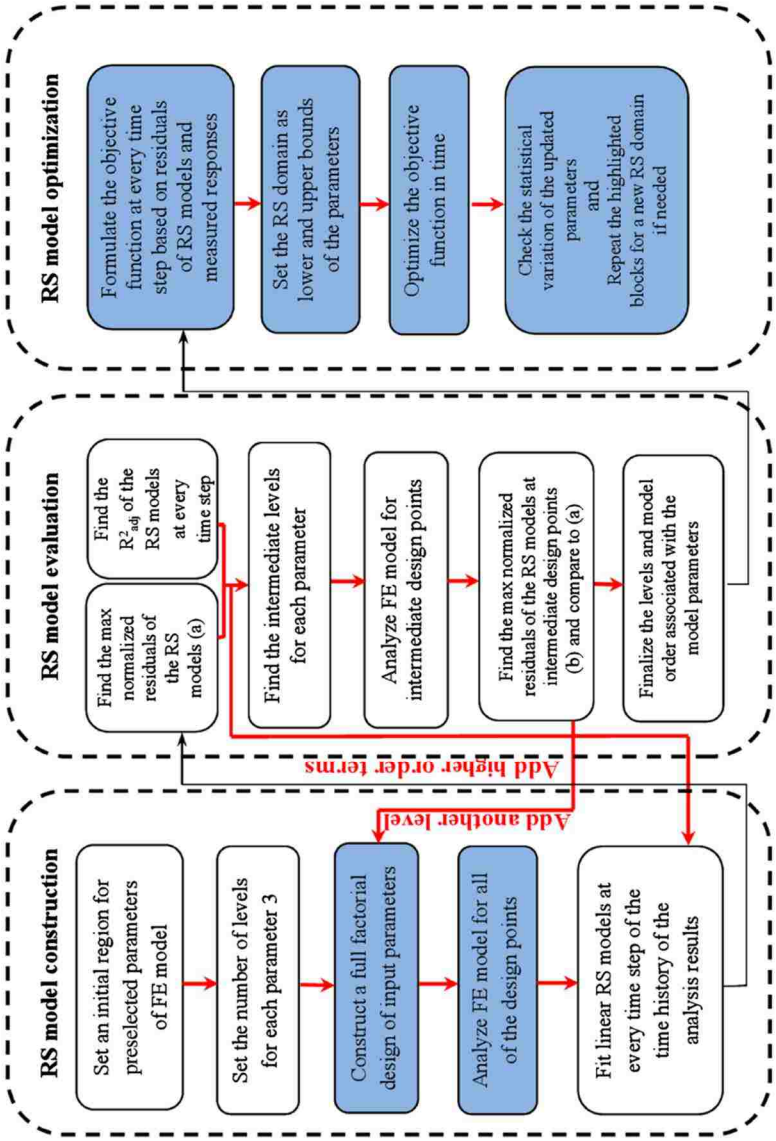

Figure 3.3. Methodology for *GRSMU*

3.5. Validation of the Proposed Model Updating Procedure

Several studies on linear FE model updating based on RS models established numerical validation studies on simple structures such as a simply supported or continues beams (Ren and Chen 2010; Ren et al. 2011; and Deng and Cai 2010). They mainly verified the proposed methods for one set of true model parameters, which is assumed to be around the center of the pre-selected RS domain where the RS model's prediction is more accurate than other points in this domain. In this study a simulated numerical case study of a steel frame with bilinear behavior was chosen to validate *GRSMU*. Since in the general framework of RS modeling the full FE model is replaced with the surrogate RS models, complexity of the structure primarily only adds to the computational cost of the FE runs, but does not change the fundamental principles of the formulation of the problem. As the location of true model parameters in the RS domain is always unknown in the inverse problem of model updating, different cases for the initial domain of the model parameters are assumed to evaluate the performance of *GRSMU* in updating the selected parameters. Details of the simulated case study along with the results of the updating procedures are presented in the following subsections.

3.5.1. Non-linear steel frame

The case study presented here is a steel frame with non-linear material properties under dynamic loading. The frame consists of one span with overall length of 228.6 cm (7' 6") supported by columns that are 83.8 cm (2' 9") long. The cross section of

the beam and column members is uniform hollow 5.08 cm (2") tube, with 0.21 cm (0.083") wall thickness. The column supports are fixed and the frame is considered a "plane frame" which constrains out-of-plane and torsional degrees of freedom. The steel has bilinear behavior with the yield stress of 344.8 MPa (50 ksi). Modulus of elasticity (E) and post yielding stiffness ratio of steel (b) were chosen as the updating parameters. To simulate the experimental data, these parameters were set to 217.2 GPa (31500 ksi), and 0.125 for E and b respectively. The loading is a concentrated harmonic lateral load with amplitude 22.2 kN (5 kips) and 5 sec period, applied at the beam column joint. The amplitude of the load is selected so that under lateral loading the stress in the columns and beam exceeds the yield stress. To update the selected parameters, simulated time histories of displacement at two locations on the frame were assumed as the experimental data. Figure 3.4 shows the configuration of the steel frame, loading and the responses used in the updating procedure.

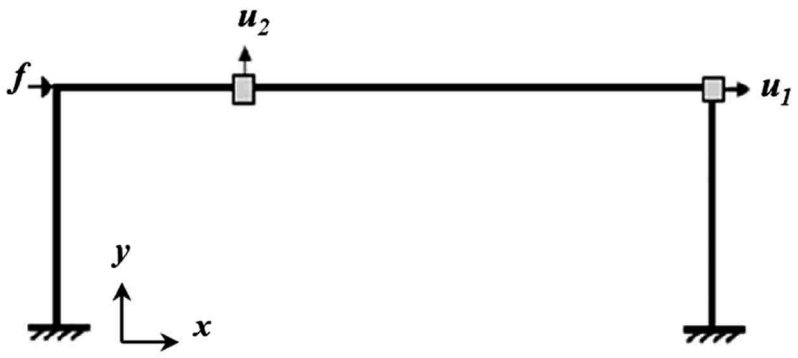

Figure 3.4. Configuration of the non-linear steel frame

3.5.2. Simulated model

A 2-dimensional mathematical model was developed by Opensees (Mazzoni et al. 2009) software. The model consists of 8 nodes and 7 elements dividing beam and columns members into two and three segments, respectively. Each node has three degrees of freedom, u_x, u_y and θ_z which allows for translation and rotation in xy plane. Elements were modeled as nonlinearBeamColumn having Steel01 uniaxialMaterial properties to construct a bilinear steel material object with kinematic strain hardening as shown in Figure 3.5. Five integration points were assigned along each element to model the distributed plasticity. A fiber section procedure was used to build the tubular steel section from 152 fibers patched together. A transient analysis object was used to apply the Newmark method integrated with the modified Newton-Raphson algorithm to solve the non-linear equitation of motion under harmonic loading. In order to avoid convergence problems during time history analysis of the non-linear frame in the model construction step, a small time step of 2.5e-4 sec were used for the dynamic analysis followed by data resampling with 400Hz sampling rate.

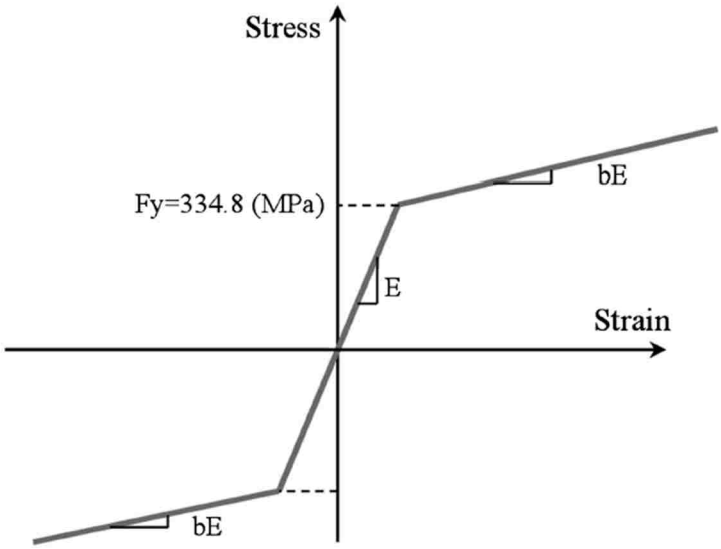

Figure 3.5. Material model for the steel

3.5.3. FE updating of the non-linear frame

Since the initial assumption for the model parameters plays an important role in performance of model updating procedures, the non-linear model was updated multiple times assuming different domains for the model parameters. Figure 3.6 shows four scenarios that were designed for this purpose. In the first scenario, the initial domain of the updating parameters was set to 186.2 to 227.5 GPa (27000 to 33000 ksi) for *E* and 0.05 to 0.25 for *b* to reflect different levels of uncertainty in estimation of these parameters.

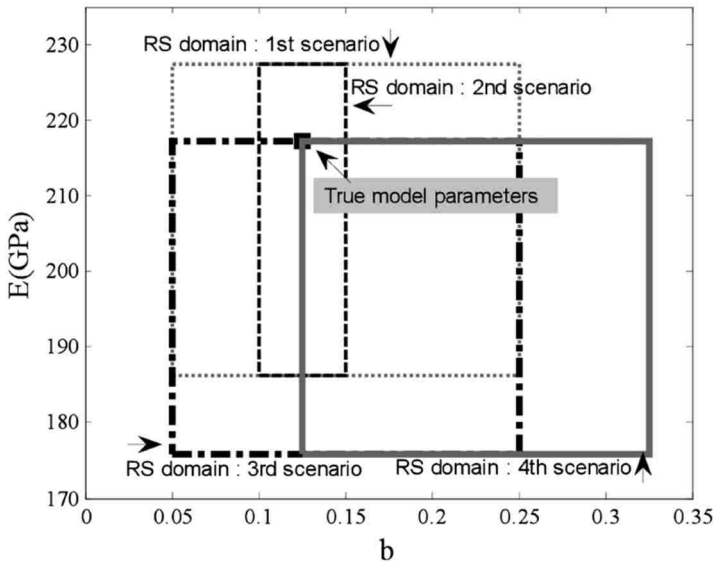

Figure 3.6. Configuration of RS domains in the validation scenarios

The RS model construction starts with full factorial design of parameters having three levels for each parameter. Figure 3.7 demonstrates the time history of displacements u_1 and u_2 for a FE model taking the levels of the 3×3 design along with the window selected for RS model construction, evaluation and optimization. This window was chosen from the time history of displacements so that the responses of the FE model are well separated at different design levels to avoid numerical errors in the optimization step. The selected time window contains 700 data samples all used for the RS model construction, evaluation and optimization.

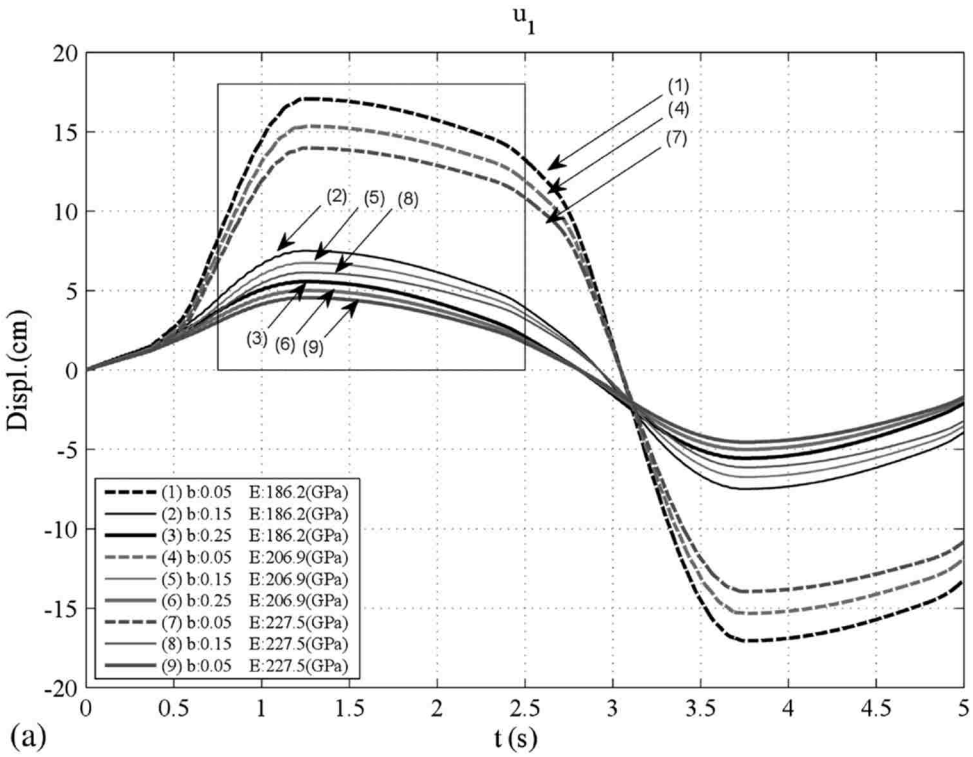

Figure 3.7(a). Time history of response of the non-linear FE model (u_1) at 3 × 3 design points

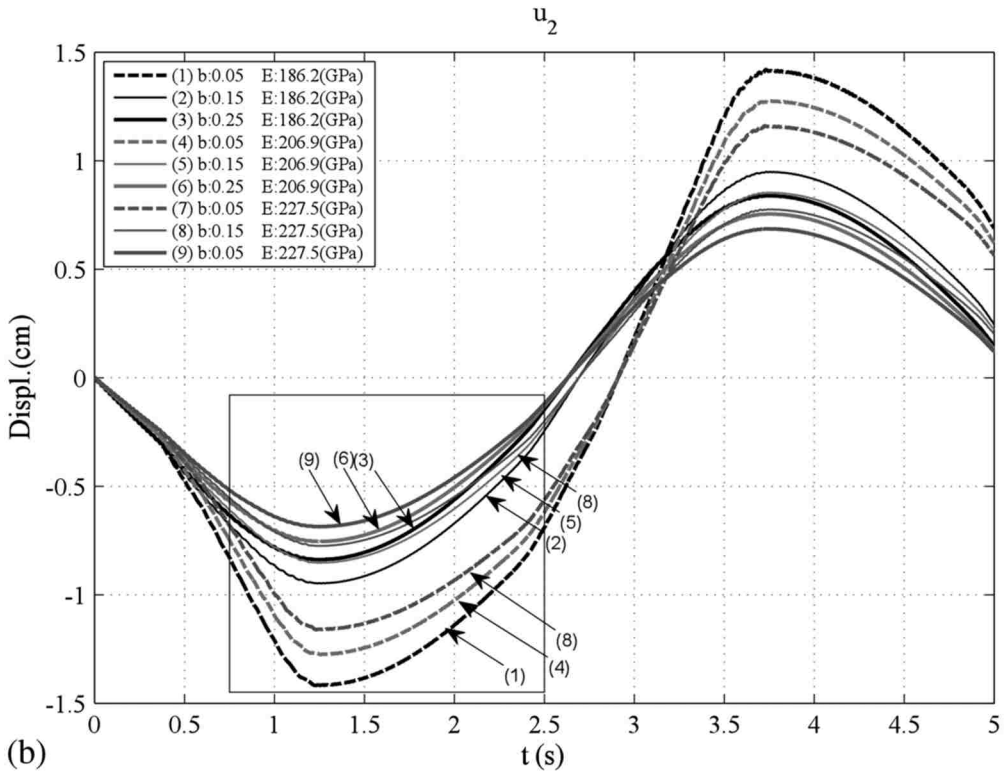

Figure 3.7(b). Time history of response of the non-linear FE model (u_2) at 3×3 design points

RS models having the linear terms of *E* and *b* were regressed through the selected time domain window. The large residuals associated with the regressed models indicate that the RS models are not accurate to replace the FE model in the time window. Consequently, quadratic terms were added to the polynomial models and regression was repeated. R^2_{adj} statistics of the RS models constructed based on 3×3 design points are plotted in Figure 3.8. This figure shows that adding the quadratic terms to the linear models significantly improves the accuracy of the RS models at the design points. It is also observed that including the cubic terms in the RS models decreases R^2_{adj} statistics due to over parameterization. Therefore, the RS models with

quadratic terms of the model parameters were selected for the performance evaluation at intermediate levels.

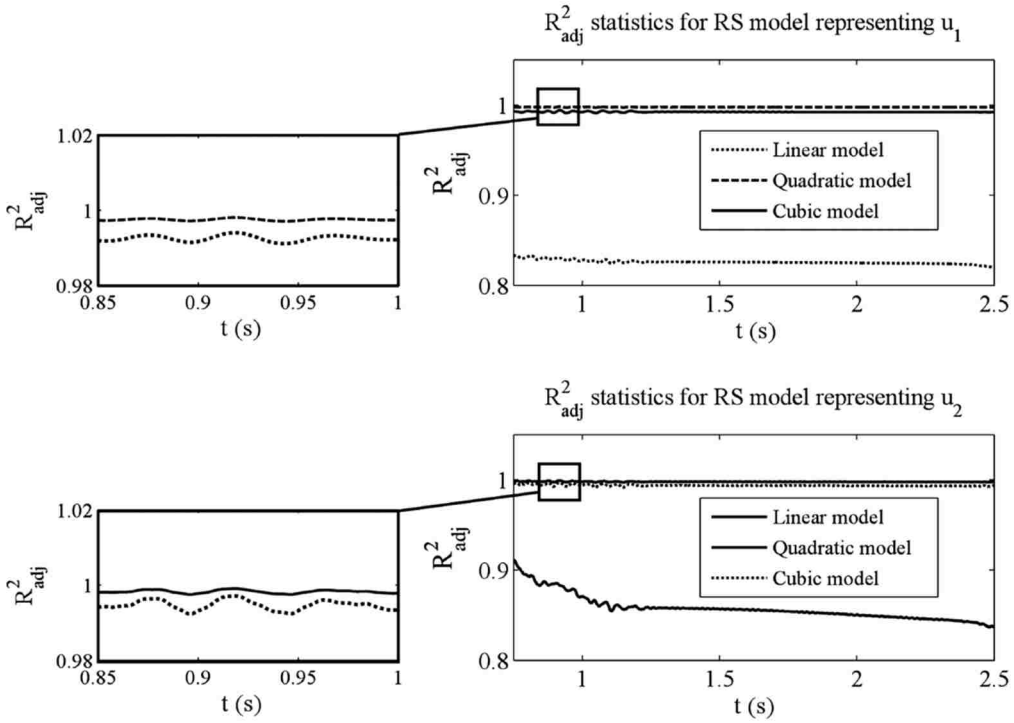

Figure 3.8. R^2_{adj} statistics for linear and quadratic RS models

Figure 3. 9 compares the maximum normalized residuals at original and intermediate levels of the 3×3 design for the quadratic RS models through the time window. In this figure dark bars show the residuals at original design points while gray bars represent the residuals at the intermediate design points. The RS models generate u_2 with smaller residuals; however, they are not successful in predicting both u_1 and u_2 at the intermediate levels corresponding to b. Therefore, the levels associated with stiffness ratio, b, in the RS domain should be finer. The steps of model construction and evaluation are repeated with 4×3 design which shows the RS models

are not accurate at intermediate levels of parameter b. Figure 3.10 displays the maximum normalized residuals of RS and FE model for a 5×3 design. The RS models contain terms up to order 4 and 2 for stiffness ratio, *b*, and modulus of elasticity, *E*, respectively. Figure 3.10 shows that the RS models perform well at both original and intermediate levels. Therefore, these models are accurate for the optimization procedure. Figure 3. 11 shows the responses of the FE model and the final RS model in the RS domain at t=2.5 sec.

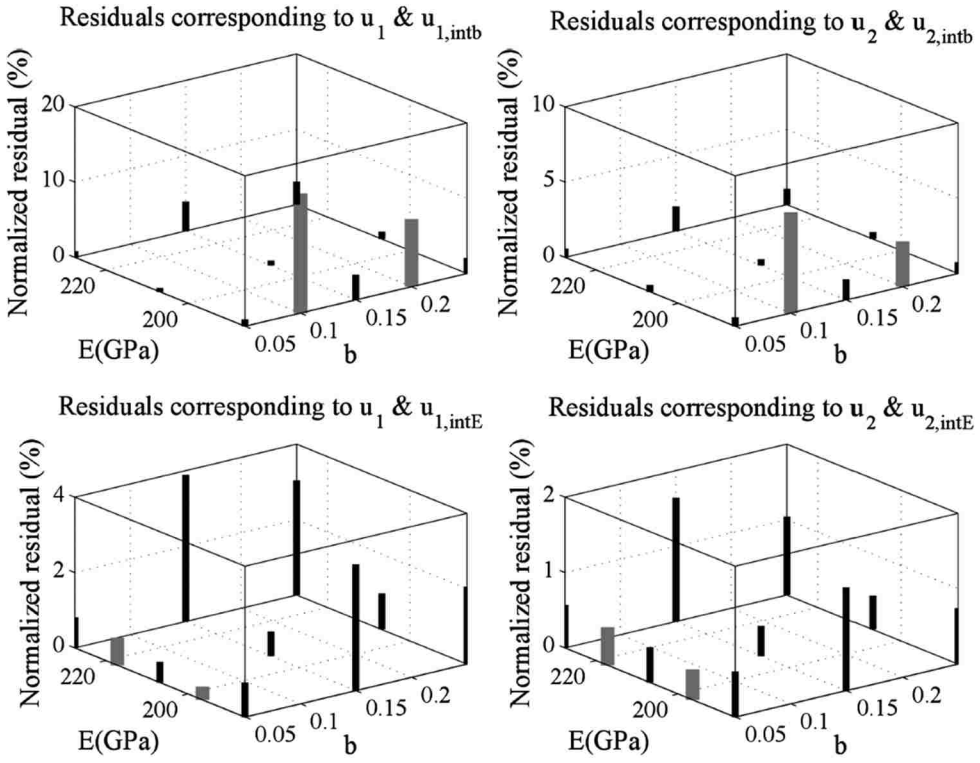

Figure 3.9. Maximum normalized residuals of original and intermediate levels using 3 × 3 design

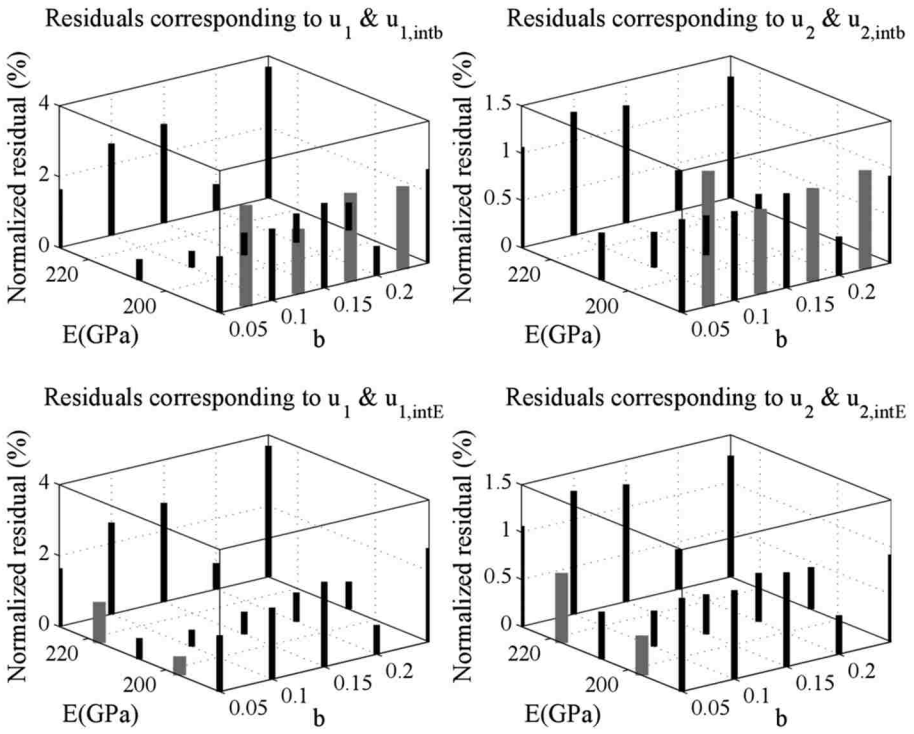

Figure 3.10. Maximum normalized residuals of the original and intermediate levels using 5 × 3 design

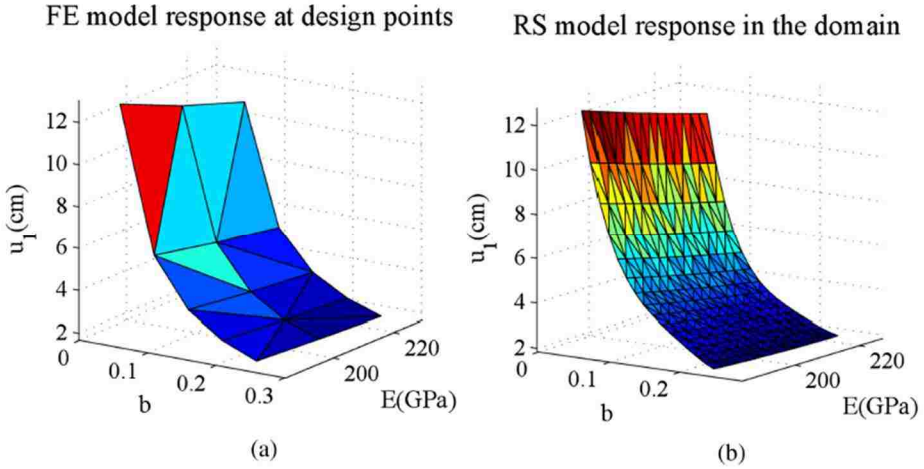

Figure 3.11. FE and RS model responses for u_1 at t=2.5 sec.

The constrained optimization problem in Eq. (3.6) was formulated and solved using *Active-set* constrained optimization algorithm (Nocedal and Wright 2006). Figure 3.12 shows the histogram of the updated parameters resulted from solving the optimization problem in every time step of the selected window in the first scenario. This histogram shows where the updated parameters locate in the RS domain. The updated model parameters are distributed in a considerably narrower region than the initial region used in the RS model construction.

In order to decrease the variation of the updated parameters, the design and model order established in the previous section for E and b are used to repeat the optimization problem. The new domain for E and b is centered on the mean value of the updated parameters in the first round of optimization. Since in the first round there were 3 and 5 levels associated with E and b, the new domain of these parameters is designed so that E and b have regions equal to 1/2 and 1/4 of their initial regions. Therefore, the RS domain is reduced into 207.4 to 228.1 GPa (30080 to 33080 ksi) for E and .095 to 0.145 for b. Figure 3.13 shows the result of the second round of model updating in the first scenario in terms of the mean and the coefficient of variation of the updated parameters. The variations of the updated parameters are decreased, and the mean value of the parameters shows negligible deviation from the true model parameters.

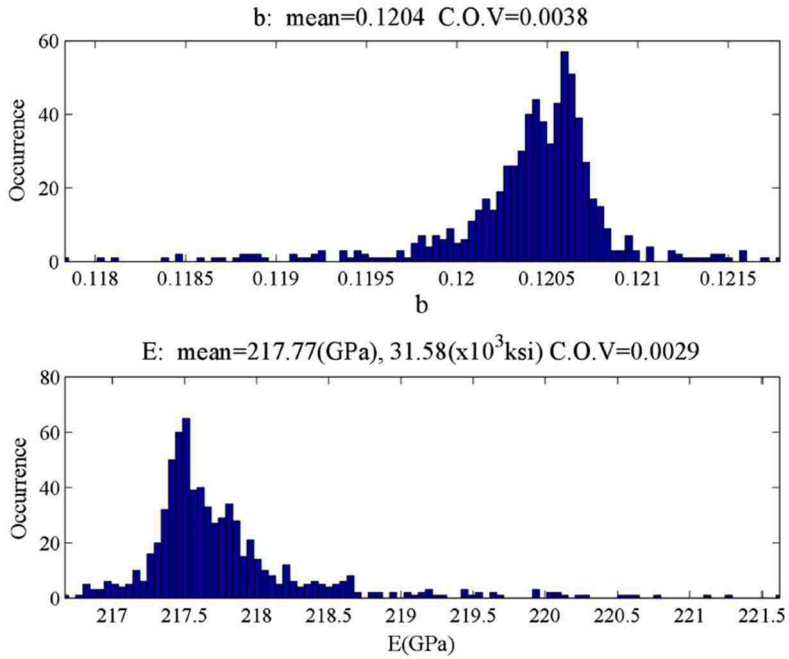

Figure 3.12. Scenario 1– first optimization round

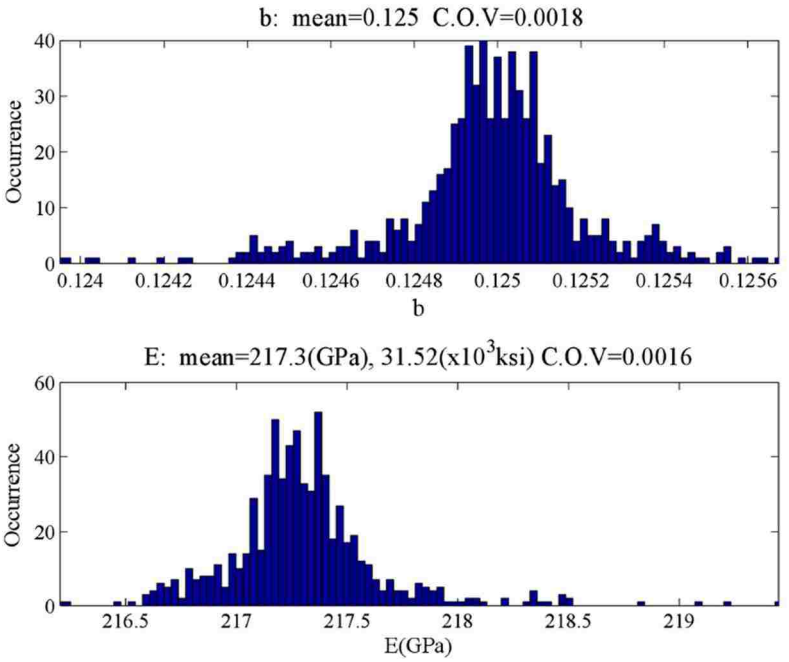

Figure 3.13. Scenario 1– second optimization round

In the second scenario, the initial regions for the model parameters are decreased to 186.2 to 227.5 GPa (27000 to 33000 ksi) for *E* and 0.1 to 0.15 for *b*. In this scenario the model construction and evaluation resulted in 3×3 design and quadratic RS models. Figure 3.14 shows the histogram of the updated parameters where their mean values converge to the true model parameters in the first round of optimization.

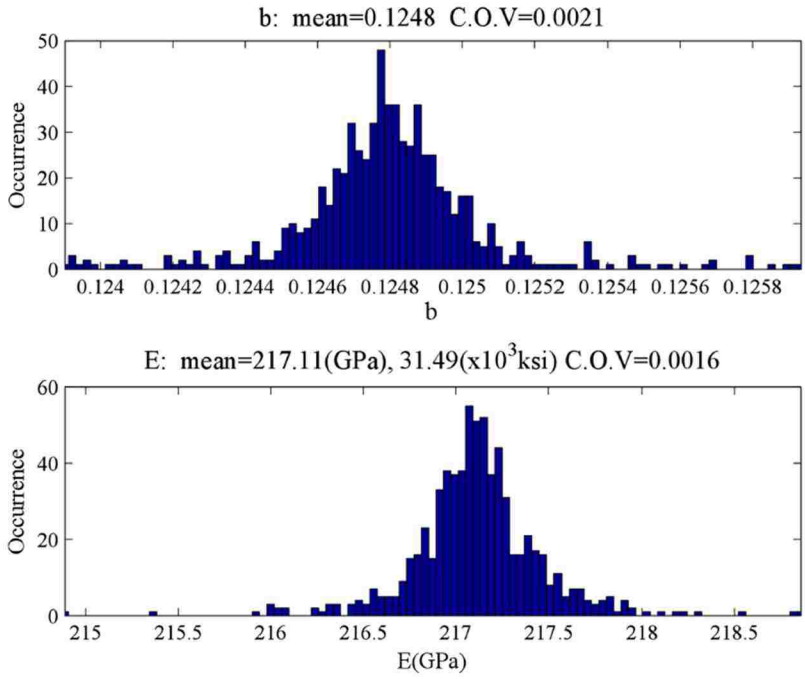

Figure 3.14. Scenario 2– first optimization round

In the third scenario, one of the true model parameters is located on the boundary of the selected RS domain. The RS domain in this case is from 175.8 to 217.2 GPa (25500 to 31500 ksi) for *E* and .05 to 0.25 for *b*. The model construction and evaluation resulted in 5×3 design and model order 4 and 2 for *b* and *E*, respectively. Figure 3.15 and 3.16 show the result of the first and second optimization rounds. The first optimization cycle successfully locates a region for the true model parameters to

which the solution of the second round of optimization converges. As it is seen in the 1st and 3rd cases, shrinkage of the selected domain, reiteration of RS modeling and optimization result in convergence to the true model parameters. However, in other situations if the true model parameters do not lie in the new region, the constrained optimization problem of RS model optimization converges to the closest corner of the RS domain to the true model parameters and results in reduction of the uncertainty associated with the initial assumptions of model parameters.

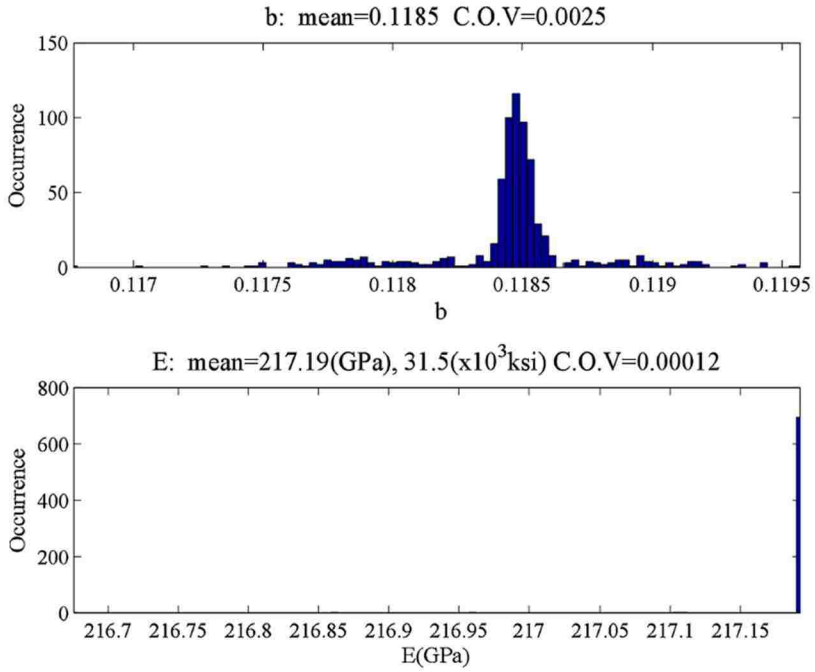

Figure 3.15. Scenario 3– first optimization round

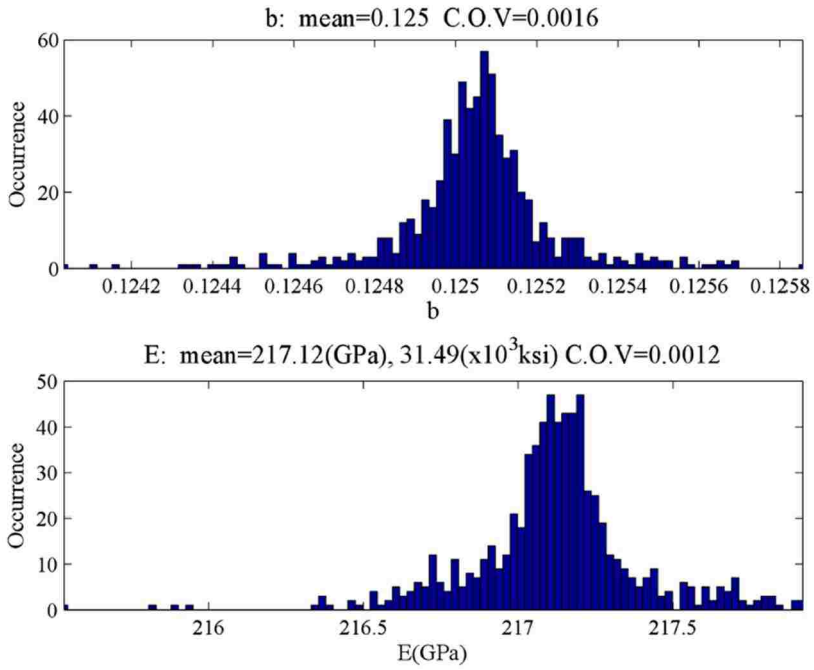

Figure 3.16. Scenario 3– second optimization round

RS domain in the last scenario is designed so that both true model parameters are located on the boundaries of the RS domain. In the initial RS domain E and b vary from 175.8 to 217.2 GPa (25500 to 31500 ksi) and 0.125 to 0.325 respectively. Based on the model construction and evaluation 3×3 design and quadratic RS models were selected. Figure 3.17 displays the result of the model updating in this scenario where the procedure performs wells in modifying the initial regions for the model parameters regardless of the location of the true parameters inside the RS domain used to fit the RS models.

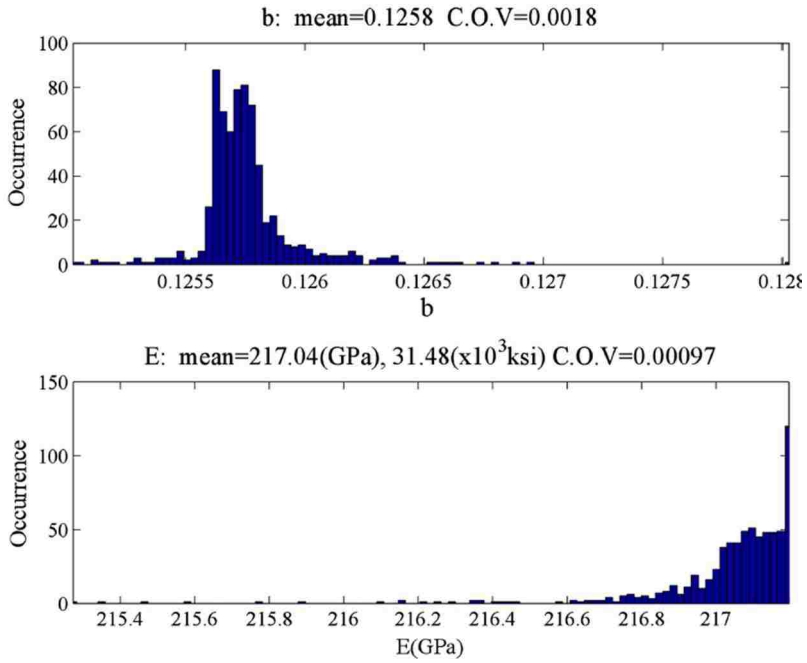

Figure 3.17. Scenario 4– first optimization round

In the cases studied in this chapter, the corners of the RS domain were used to establish a multi-start optimization process using active-set algorithm. Since the resulted histograms from the multi-start optimization procedures were not sensitive to the choice of the initial point, in this case study applying a global search technique was not necessary. It should be noted that in these case studies, RS model updating succeeds in finding the unique solution of the inverse problem. However, in some model updating problems, a "family" of solutions could satisfy the optimization objectives. Global search of the domain of model parameters discovers possible scenarios of meaningful updated parameters for the FE model to generate similar response features. The use of RS models readily enables application of any optimization techniques to explore the domain of model parameters which may not be

feasible using the full FE model. However, RS models are at best approximating the FE model responses. They reduce the computation effort of the search for model parameters in a lower resolution domain. While this may alter some of the possible optimal results, application of RS models in FE model updating proves helpful in better parameter estimations than the initial model assumptions in predicting the measured responses.

3.5.4. Performance of the proposed algorithm compared with sensitivity method

To verify the performance of *GRSMU*, the non-linear model studied in the previous section was updated using sensitivity method and the results of the two procedures were compared. For each scenario described before the sensitivity method model updating was applied using the vertices of the RS domain as the initial point. The case of the second scenario with the smallest RS domain was the only one where the sensitivity method converges to the true model parameters using any of the starting points. In the other scenarios when the initial point is relatively far from the true model parameters the procedure does not converge to these parameters. These results were summarized in Table 3.1.

Table 3.1. Comparison of the performance of GRSMU and the sensitivity method (Noise-free simulated data)

	Relative error (%) in updated parameters					
	Starting point		***Sensitivity method***		***GRSMU***	
	b	E (GPa)	b	E (GPa)	b	E (GPa)
Case 1	0.05	186.2	0.3	0.1	0	0.1
	0.25	186.2	N. C.[a]			
b: 0.05 to 0.25	0.05	227.5	0.3	0.3		
E: 186.2 to 227.5 GPa	0.25	227.5	N. C.			
Case 2	0.1	186.2	0.2	0	0.2	0
	0.15	186.2	0.5	0		
b: 0.1 to 0.15	0.1	227.5	0	0.2		
E: 186.2 to 227.5 GPa	0.15	227.5	0.2	0.3		
Case 3	0.05	175.8	0.1	0	0	0
	0.25	175.8	N. C.			
b: 0.05 to 0.25	0.05	217.2	0.2	0.3		
E: 175.8 to 217.2 GPa	0.25	217.2	N. C.			
Case 4	0.125	175.8	0.2	0.3	0.6	0
b: 0.125 to 0.325	0.325	175.8	N. C.			
E: 175.8 to 217.2 GPa	0.325	217.2	N. C.			

[a] N. C. : No Convergence

Furthermore, to evaluate the performance of *GRSMU* in the presence of noisy measurement data, different levels of Gaussian noise were introduced into the simulated experimental responses and the updating procedures in cases 1 and 4 were obtained. The sensitivity-based method was also repeated for data from a time window, such that the updated parameters of each time step were used as the initial point for the next one. The results of these procedures are summarized in Table 3.2.

Table 3.2. Comparison of the performance of *GRSMU* and the sensitivity method (Simulated data with different noise levels)

	True model Parameters b=0.125 E=217.2(GPa)*					
	Starting point			***Sensitivity method***		
					Relative error (%) in updating parameters	
	b	E(GPa)	noise level(%)	time(sec)	b	E(GPa)
Case : 1			1	4704	0.80	-0.3
b: 0.05 to 0.25	0.05	186.2	5	6538	0.80	0.6
E: 186.2 to 227.5 GPa			10	7043	104.00	-13.2
Case : 4			1	4723	0.00	0.8
b: 0.125 to 0.325	0.125	175.8	5	6221	21.60	-5.5
E: 175.8 to 217.2 GPa			10	9174	68.80	-10.4
	Starting point			***GRSMU***		
					Relative error (%) in updating parameters	
	b	E(GPa)	noise level(%)	time(sec)	b	E(GPa)
Case : 1			1	1177	0.16	-0.04
b: 0.05 to 0.25	0.05	186.2	5	1132	4.64	-1.94
E: 186.2 to 227.5 GPa			10	1115	10.72	-3.72
Case : 4			1	288	3.52	-1.40
b: 0.125 to 0.325	0.125	175.8	5	274	15.20	-5.59
E: 175.8 to 217.2 GPa			10	274	25.60	-7.72

When the noise level is low (1%) for case 1 both methods are similarly accurate (less than 1% relative error), while for case 4 the error in updated parameters based on *GRSMU* goes up to 3.5% . It should be noted that scenario 4 was designed to have both true model parameters on the boundaries of the domain and as it can be seen in Table 3.1 the results of the sensitivity-based method for this scenario are highly dependent on the choice of starting point for convergence. In the case of moderate noise level (5%) *GRSMU* outperform the sensitivity-based method in scenario 4.

Lastly, with high level noise assumption, *GRSMU* yields significantly more accurate results in both scenarios. The performance of these procedures was further compared in terms of the time required to complete the updating process. As seen in Table 2 *GRSMU* shows to be considerably more time efficient than the other method, for instance in case 1 (1% noise) performing 70 steps of sensitivity-based updating took 4704 seconds, whereas the overall time required for model construction, evaluation and optimization for 700 time steps based on *GRSMU* took 1177 seconds.

The advantage of using *GRSMU* is that this procedure successfully finds a smaller region for the model parameters regardless of the size of the RS domain, location of the true model parameters and the starting point in the optimization process. Moreover, the results of *GRSMU* have corrective information for the initial estimate of the RS domain whereas with a relatively far estimate for the parameters the sensitivity method may yield meaningless results. Finally, while *GRSMU* requires significantly less computational time than sensitivity-based updating method, it shows more robustness to moderate and high level noise.

3.5.5. Performance of the proposed algorithm in presence of modeling error

Modeling errors proves unavoidable in any FE model simulations. Therefore, study of the proposed method's performance in existence of such errors is of value. For this purpose, 1st and 4th scenarios introduced earlier were reiterated by using another FE model to generate the measured responses. This model consists of 28 elements with 602 fibers in their sections modeled with Steel02 uniaxialMaterial

properties which adopts uniaxial Giuffre-Menegotto-Pinto steel material model (Mazzoni et al 2009). Three time windows were selected for the optimization from 0.75 sec to 7.625 sec, each having 700 time steps. Due to modeling error introduced to generate reference responses, maximum error associated with u_1 and u_2 in the selected time windows are 29.88% and 27.76% relative to the responses from FE model without any modeling errors. Root mean square of the error is 6.80% and 6.18 % over all three windows. The results of these case studies in terms of the relative error in estimation of the parameters are shown in Table 3.3. The error is larger compared to cases without modeling error (shown in Table 3.2) except for error in estimation of b in case 4 with moderate and high measurement noise levels.

Table 3.3. Relative error in estimation of the parameters in presence of modeling error and measurement noise

	Noise Level (%)	Relative error (%) in updating parameters	
		mean	
		b	E
Case : 1	1	1.42	-3.82
b: 0.05 to 0.25	5	6.01	-4.59
E: 186.2 to 227.5 GPa	10	10.87	-4.60
Case : 4	1	6.62	-5.21
b: 0.125 to 0.325	5	14.41	-7.77
E: 175.8 to 217.2 GPa	10	23.75	-9.20

3.6. Summary and Conclusions

This chapter presents a procedure for designing RS models capable of generating the results of FE analysis with good accuracy. Also, formulating the model updating

problem in an iterative format in time domain is demonstrated to update non-linear FE models. This procedure is called *General Response Surface Model Updating (GRSMU)*.

GRSMU was applied to a numerical case study of a steel frame with global non-linearity. In the first and second steps an appropriate design and RS model order were successfully established. The optimization in time window performed well in all simulated scenarios. The first round of optimization resulted in a considerably narrower bounds for the uncertain parameters of the model than the initial boundaries set at the beginning of the procedure. Repeating the RS model construction with known order and design for the new bounds of parameters and solving the optimization problem resulted in updated parameters with slight deviation from the true model parameters.

In order to verify the performance of *GRSMU* , the simulated scenarios was repeated based on a sensitivity-based model updating technique assuming different levels of noise in the measurement data. Unlike *GRSMU*, the convergence of the sensitivity-based method depends on the choice of the starting point. Moreover, the results of *GRSMU* have corrective information for the initial estimate of the RS domain whereas with a relatively far estimate for the parameters the sensitivity method may yield meaningless results. Finally, while *GRSMU* is considerably more time efficient than sensitivity-based updating method, it shows more robustness to moderate and high level noise. The performance of *GRSMU* was also studied in a simulation study in presence of modeling error. It was observed that in the case study

presented here, *GRSMU* is successful in estimating the unknown parameters of the model, with a larger estimation error than the cases without modeling error, particularly when measurement noise level was low.

Since in the proposed methodology the RS model is optimized in time domain, the procedure is applicable to linear or non-linear models under static or dynamic analysis. Moreover, parameters related to linear and non-linear behavior of the system can be updated simultaneously as done in the simulated case study.

It should be noted that although replacing the FE model with a polynomial function is a critical step in simplifying the model updating problem, the fact that the RS model is at best an approximation should not be overlooked. Therefore, construction and evaluation of RS models iteratively in time domain is proposed here to compensate for the error caused by approximation of the FE model responses.

Chapter 4

Effect of Measurement Noise and Excitation on Generalized Response Surface Model Updating

This chapter evaluates the sensitivity of the model updating algorithm presented in the previous chapter (GRSMU) with respect to measurement noise (Shahidi and Pakzad, 2014b). This evaluation is critical, as noise contamination is inevitable in any measurement procedure. In addition, the effect of input excitation frequency content and further application of this method in updating a non-linear frame under seismic loading are presented.

In RS-based FE model updating, RS models replace the full FE model in a pre-selected domain of unknown model parameters, here called RS domain. These RS models are constructed using least square techniques (Montgomery et al., 2004) by regressing a polynomial function on a set of points sampled from the RS domain. Techniques of designs of experiments (Montgomery, 2001) can be employed in order to sample these points. However, finding the appropriate model order associated with each parameter and design of model parameters' levels that produce accurate RS models, require a number of trials and errors which may contradict the primary

motivation for using the RS models to decrease the computational cost of FE model analyses in model calibration.

GRSMU is proposed to systematically design the levels and model order of the RS models, and extend the application of RS modeling for non-linear model updating in time through RS model construction and optimization iteratively at every time step of the analysis. In order to construct accurate RS models capable of predicting the response of the FE model throughout the RS domain, GRSMU adopts a full factorial design with minimum number of levels and linear RS models. This procedure is subsequently followed by evaluation of the regressed RS models in terms of accuracy and predictability, and increasing the model order or number of levels associated with each model parameters, when required. When RS model order and design are decided, any non-linear constrained optimization algorithm can be readily adopted to solve this explicitly formulated FE model updating problem formulated in Eq. (4.1) for the l^{th} time step of the non-linear dynamic analysis.

$$\begin{aligned} &\min_{\theta_j} \; f_l = \sqrt{\sum_{i=1}^{s} \left(\frac{RS_{il}(\theta_1, \theta_2, ..., \theta_m) - y_{\exp il}}{y_{\exp il}} \right)^2} && i = 1,2,...,s \\ &s.t. \quad \theta_{jlb} \le \theta_j \le \theta_{jub} && j = 1,2,...,m \end{aligned} \tag{4.1}$$

In this equation $RS_{il}(\theta_1, \theta_2, ..., \theta_m)$ denotes the RS model associated with the l^{th} time step of the analysis representing the i^{th} analytical response feature, as a function of the pre-selected uncertain model parameters $(\theta_1, \theta_2, ..., \theta_m)$, θ_{jlb} and θ_{jub} represent the

lower and upper bounds of the j^{th} model parameters in the RS domain, and y_{expil} is the i^{th} response feature measured at the l^{th} time step of the experiment.

4.1. Sensitivity of the GRSMU Estimates to Measurement Noise

This section investigates the effect of measurement noise on the parameter estimation results of GRSMU. This study simulates the measurement error as White Gaussian noise in which the values at any pair of time instances in the noise signal are statistically independent and identically distributed with a zero-mean normal probability distribution.

In order to study the sensitivity of GRSMU estimates to noise, assume a single-DOF dynamic system. As Eq. (4.2) indicates, the measured output of this system (u_m) at any time instance t_i can be considered as a summation of real response (u_m^r) and measurement noise in that time step.

$$u_m(t_i) = u_m{}^r(t_i) + n(t_i) \tag{4.2}$$

where $n(t_i)$ is a random variable representing the amplitude of noise in time t_i having a zero-mean normal distribution with standard deviation σ.

With assumption of known mass, the response of an FE model simulating this system is a function of stiffness (k). Over a small domain of k, a linear RS model can approximate the real response of the system at any time step of the analysis. Eq. (4.3) presents this linear function at time step t_i.

$$RS(k,t_i) = \hat{\beta}_0(t_i) + \hat{\beta}_1(t_i) \times k \qquad k_{lb} \le k \le k_{ub} \tag{4.3}$$

In this equation, k_{lb} and k_{ub} denote the lower and upper bounds of domain of k, where the linear RS model (with coefficients $\hat{\beta}_0(t_i)$ *and* $\hat{\beta}_1(t_i)$) replaces the FE model of the system. Eq. (4.4) formulates the model updating procedure in which parameter estimation is accomplished by minimizing the residual of the predicted and measured responses.

$$\begin{aligned} \min \quad & f(k,t_i) = (\hat{\beta}_0(t_i) + \hat{\beta}_1(t_i) \times k - u_m(t_i))^2 \\ s.t. \quad & k_{lb} \le k \le k_{ub} \end{aligned} \tag{4.4}$$

Since f is a nonnegative function, its minimum value at every time step (t_i) corresponds to the root of $f(k,t_i)$. This statement holds with the assumption that the domain of the RS model includes the root of $f(k,t_i)$. High amplitudes of noise and/or when model parameters locate outside or on the corners of the RS domain can contradict this assumption. In such cases the solution of this constraint optimization problem is k_{lb} or k_{ub} whichever associates with a smaller f.

Therefore, estimation of k based on the measured response k_{est} in time instance t_i is

$$k_{est}(t_i) = \frac{u_m(t_i) - \hat{\beta}_0(t_i)}{\hat{\beta}_1(t_i)} \tag{4.5}$$

It should be noted that if $f(k,t_i)$ in Eq. (4.5) has two roots (k_{lb} and k_{ub}) in the domain, the formulation of the problem does not change. Double roots in the domain

could occur because (1) k_{lb} and k_{ub} generate the same response at time step t_i, or (2) k_{lb} and k_{ub} generate the same response time history. In case (1), as the time history of the responses are not the same in other time steps, through the parameter estimation in time history of the reponse, the true k will be estimated. In case (2), by solving Eq. (4) using a global optimization framework which is able to find multiple optima, both k_{lb} and k_{ub} are estimated. Therefore, in both cases, Eq. (4.5) can be used to demonstrate the estimated stiffness with reference to the measured response of the system.

Since $u_m{}^r(t_i)$, $\hat{\beta}_0(t_i)$ *and* $\hat{\beta}_1(t_i)$ are independent of measurement noise, the expected value of $k_{est}(t_i)$ can be written as

$$E[k_{est}(t_i)] = \frac{u_m{}^r(t_i) - \hat{\beta}_0(t_i)}{\hat{\beta}_1(t_i)} \tag{4.6}$$

therefore, its sensitivity with respect to the standard deviation of White Gaussian noise is

$$\frac{\partial E[k_{est}(t_i)]}{\partial \sigma} = 0 \tag{4.7}$$

This results show that the expected value of the estimated stiffness in time is not sensitive to the measurement noise amplitude. The main assumption in derivation of Eq. (4.7) is zero-mean assumption for the noise signal. Therefore, for any non-Gaussian or non-stationary noise, it is expected to observe similar estimation performance as long as the zero-mean assumption for the underlying probability density function of the noise signal holds. In the following sections, several parametric

sensitivity studies are performed to accomplish this goal with assumption of White Gaussian measurement noise.

4.2. Non-linear Model Updating Using Harmonic Loading

This section describes the implementation of the methodology that was developed in previous section to study the robustness of GRSMU in a single-DOF and a multi-DOF bilinear system. In each case, the response of the system is simulated under several assumptions of measurement noise level and input excitation. The parameter estimation is then completed in two different time-domain windows, and the estimation error is investigated. The following subsections describe the sensitivity study carried out for these systems in detail.

4.2.1. Numerical simulation: Single-DOF system

This section studies the sensitivity of GRSMU estimates to the measurement noise level through a numerical case study of a single-DOF non-linear system under harmonic loading. This single-DOF system is simulated with unit mass (1 lb.sec^2/in = 175.09 kg) and bilinear stiffness material model. Stiffness of the system (k) and yielding force are 4 lb/in (0.7 N/mm) and 4 lb (17.79 N), respectively. The natural period of vibration of this system (T_n) is 3.14 seconds. Post yielding stiffness ratio of the system (α) is selected as an uncertain model parameter varying between 0.2 and 0.8 to be estimated from the time history of the displacement of the mass.

In order to study the impact of the frequency of the input harmonic loading, in different scenarios period of the applied load (T_{load}) varies so that the ratio of the loading frequency over the natural vibration frequency varies from 0.1 to 10. In these scenarios the amplitude of the load is adjusted so that in all the cases maximum displacement of the system in the longer window used for parameter estimation is 3 in (7.62 cm). A time step of 0.001 sec is used in the time history analysis of this non-linear system, which satisfies a convergence test with 10e-6 lb (4.45e-6 N) tolerance for the norm of the unbalanced force in every time step of the dynamic analysis. This time step is small enough, not to affect the accuracy of the results, as selection of a smaller time step did not change the results of the dynamic analysis.

In every scenario, two time-domain windows are used for the parameter estimation: (1) a T_n-sec long window, and (2) a T_{load}-sec long window. The model construction and evaluation steps in the longer window of (1) and (2) in every scenario are completed to obtain the RS models of displacement as functions of α. Subsequently, residuals of simulated measured displacement and regressed RS models are minimized along the selected time window to update α.

The optimization problem of model updating in the T_n-sec long time window is completed with sampling frequency of 100 Hz based on a multi-start optimization framework using interior-point algorithm (Nocedal and Wright 2006). Different levels of the measurement noise are assumed in each case. Noise level denotes the ratio of the root mean square of the simulated Gaussian noise signal to the root mean square of the simulated measured signal. Figures 4.1 to 4.4 show the results of the updating

procedures where α is set equal to 0.625 and 0.2 to simulate the measured displacement signal.

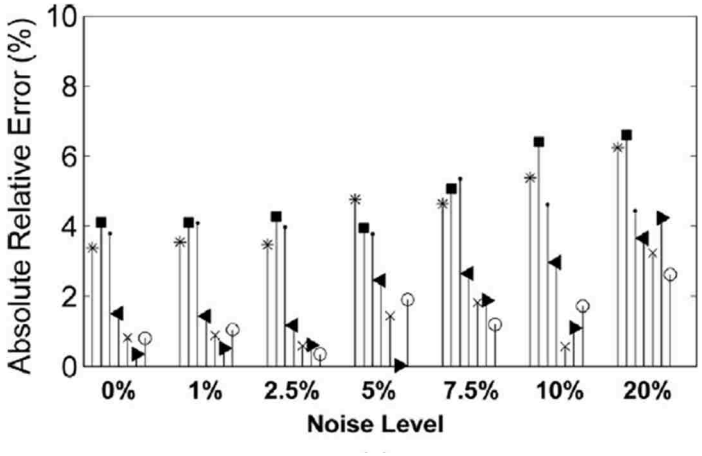

Figure 4.1. Error sensitivity in estimated α (Single-DOF system, αtrue=0.625 and Tn-sec long window): mean

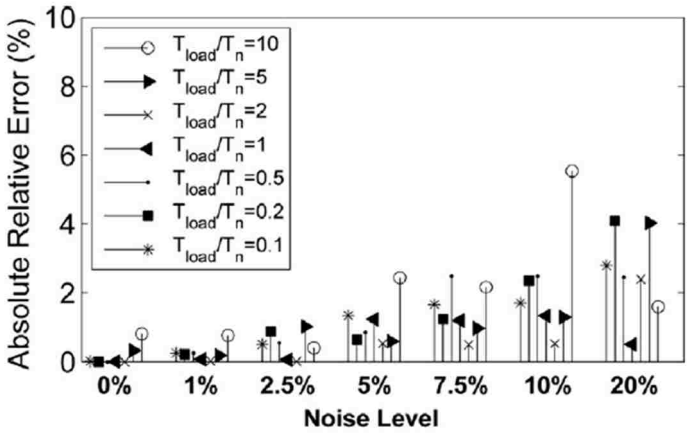

Figure 4.2. Error sensitivity in estimated α (Single-DOF system, αtrue=0.625 and Tn-sec long window): median

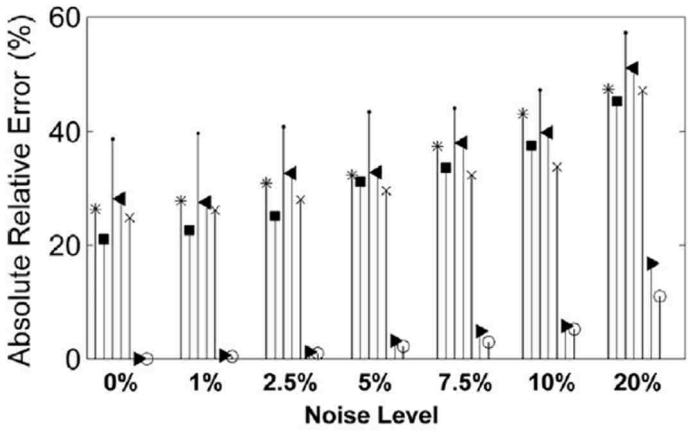

Figure 4.3. Error sensitivity in estimated α (Single-DOF system, αtrue=0.2, and Tn-sec long window): mean

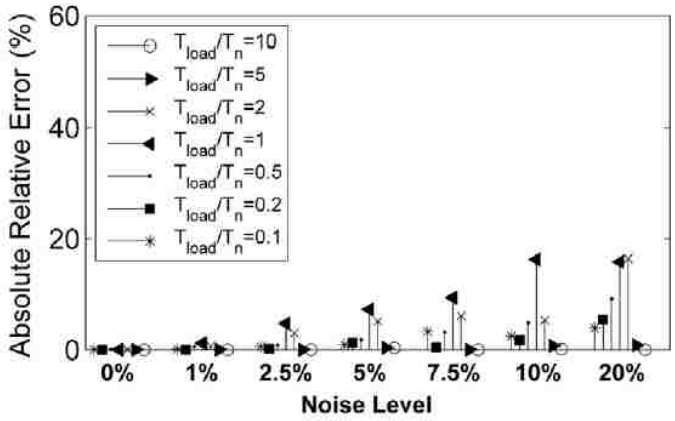

Figure 4.4. Error sensitivity in estimated α (Single-DOF system, αtrue=0.2, and Tn-sec long window): median

The results show that, as indicated by Eq. (4.6), the mean of the updated α is fairly insensitive to the measurement noise level, particularly when it is low or medium. However, when the assumptions made in derivation of Eq. (4.4) are violated, the constrained optimization problem of RS model updating is likely to result in the bounds of the selected RS domain as the optima. This can cause the mean value of the

estimated α deviate considerably from αtrue, while the median - having a breakdown point of 50% -robustly estimates the true α. Therefore, in the following cases, the median of the updated model parameters are reported as the point estimate of the true parameters. These figures also show that, when sampling frequency in the response measurement is high enough relative to the loading frequency, frequency of the input excitation does not significantly influence the accuracy of the estimated parameters, particularly at low levels of measurement noise.

The updating procedure in the previous scenarios is iterated in a time window equivalent to the period of loading (T_{load}) in each case. The optimization frequency in these cases is adjusted to have the same number of time steps as for the cases with T_n-sec long time window. Figure 4.5 and 4.6 display the error sensitivity of the median of the updated parameters to the measurement noise, when the parameter estimation of this single-DOF system is completed in a T_{load}-sec long time window. This figure shows that when α_{true}=0.625, the estimation error is less sensitive to the noise level and the length of the time window compared to the cases when α_{true}=0.2. Furthermore, in the latter cases, the largest estimation error of all of the noise levels is observed when frequency of the loading approaches natural vibration frequency of the system.

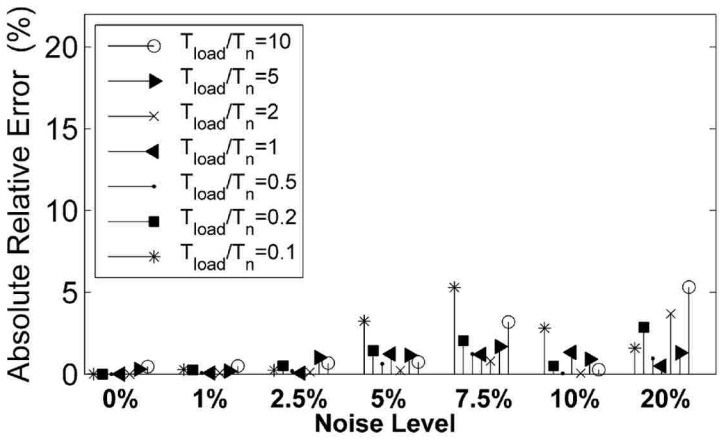

Figure 4.5. Error sensitivity of the median estimated α (Single-DOF system, T_{load}-sec long window): α_{true}=0.625

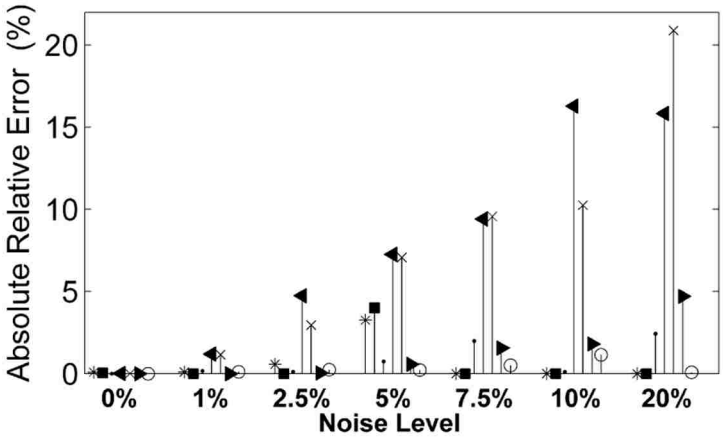

Figure 4.6. Error sensitivity of the median estimated α (Single-DOF system, T_{load}-sec long window): α_{true}=0.2

It should be noted that, amongst all the cases of the single-DOF model updating, the results of the cases with T_{load}/T_n =10 ("slow" loading) consistently show robustness to 20% measurement noise level. When the harmonic load is applied "fast" (T_{load}/T_n =0.1) and T_{load}-sec window is used for parameter estimation, the estimation

error is comparable to the results of the "slow" loading; however, when updating is completed in the constant length time window (T_n sec), the estimation error for the "fast" loading case is larger than the "slow" loading case, at 20% measurement noise level. Figures 4.7 to 4.10 illustrate the normalized median deviation of the parameter estimation in all the cases studied here. Since the median is selected as the point estimate of the updated parameters in each scenario, the absolute median deviation with respect to the median of the histograms of updated α is calculated and normalized by the true model parameters in each case.

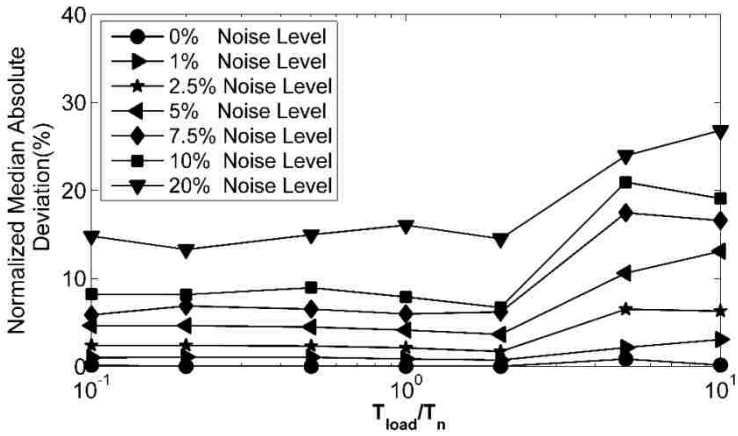

Figure 4.7. Normalized median absolute deviation of the estimated α (Single-DOF system, T_n-sec long window): α_{true}=0.625

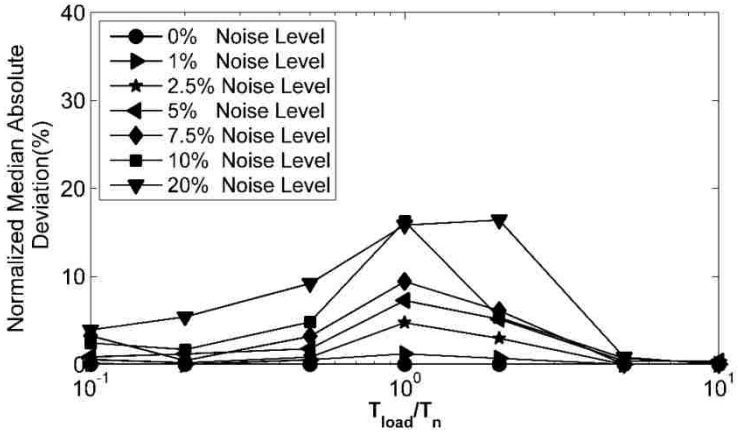

Figure 4.8. Normalized median absolute deviation of the estimated α (Single-DOF system, T_n-sec long window): α_{true}=0.2

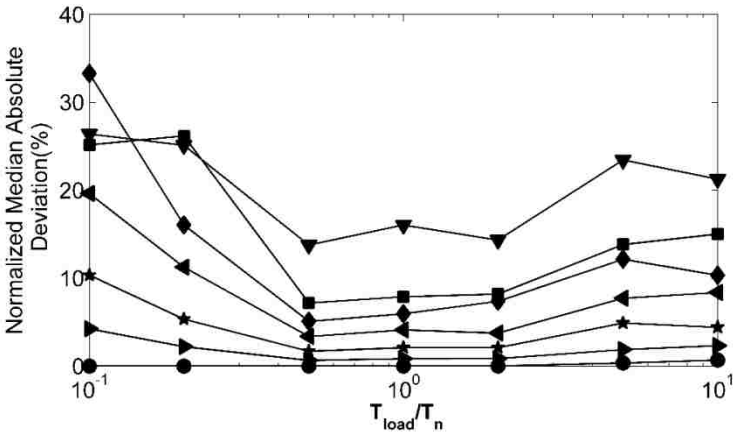

Figure 4.9. Normalized median absolute deviation of the estimated α (Single-DOF system, T_{load}-sec long window): α_{true}=0.625

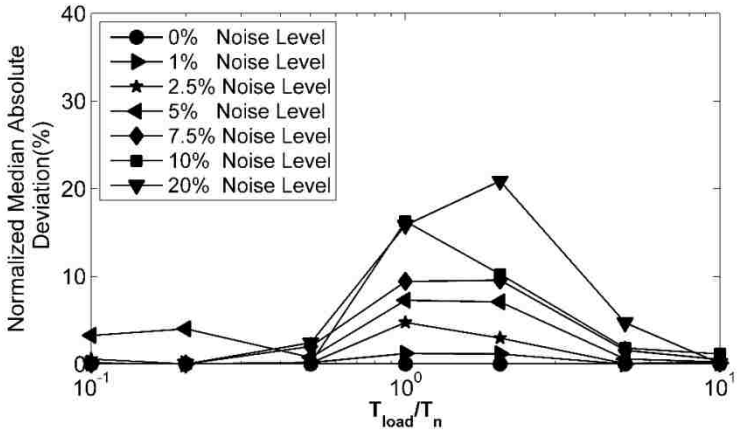

Figure 4.10. Normalized median absolute deviation of the estimated α (Single-DOF system, T_{load}-sec long window): α_{true}=0.2

These figures show that the dispersion of the updated α is roughly insensitive to the selected time window, with the exception of the cases with small ratio of T_{load}/T_n when α_{true}=0.625. Furthermore, the largest deviation corresponds to the cases with the highest level of noise contamination. When α_{true}=0.2, the deviation of the updated α increases considerably as the period of the harmonic loading approaches the vibration period of the system. The reason is that in such cases, the response of this non-linear system in the selected time windows has low sensitivity to permutation of the post yielding stiffness ratio, and thus in the cases with high simulated measurement noise, dispersion of the optimization results increases significantly.

4.2.2. Numerical simulation: Multi-DOF system

In order to further investigate the sensitivity of GRSMU to the measurement noise and input excitation, a multi-DOF system is considered. This simulation is for a cantilever steel beam with non-linear material model under a harmonic load, applying

vertically at its tip. Figure 4.11 shows the configuration of this simulated beam. This beam, with 30 in (76.2 cm) length, has a 2" (5.08 cm) square section. The steel behaves bilinearly with modulus of elasticity (E) and yield stress of 29,000 ksi (200 GPa) and 50 ksi (344.8 MPa), respectively. A uniform dead load on the beam is designed so that the fundamental vibration period of this system (T_1) is 1.57 sec. Post yielding stiffness ratio of the material (α) is selected as uncertain model parameter varying between 0.2 and 0.8. Time history of displacement at the tip of the beam (u(t)) is used to estimate α in this range in scenarios with different ratios of T_{load} /T_1 varying between 0.2 to 20. In all these cases, maximum displacement in the longer model updating window and the true model parameters are the same as for the single-DOF case discussed previously.

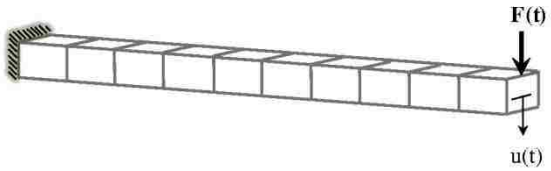

Figure 4.11. Configuration of the simulated cantilever beam

It should be noted that GRSMU framework can be used for parameter estimation in linear and non-linear systems. For linear systems, in addition to using input-output data for model updating, natural frequencies and mode shapes can be used for parameter estimation through GRSMU which requires no prior knowledge of the input excitation. However, in the cases of non-linear systems, to use the time domain data for updating the uncertain model parameters, known input excitation is used to run the

FE model, generate, and validate the RS surrogate models. Therefore, RS model construction and evaluation in all these single- and multi-DOF cases are completed with assumption of known experimental input excitation, and thus the type of excitation (harmonic, random, etc.) does not bear any effect on the proposed methodology for parametric sensitivity study. In order to study the robustness of GRSMU results to the frequency content of the input excitation, single harmonic loading is chosen in this study which allows controlling one parameter (loading period) at a time and studying the potential effect of dynamic amplification of the system on GRSMU estimates, while in each case several levels of measurement noise contamination is also considered. In applying the input harmonic excitation, the period of loading is set while the amplitude is adjusted in each T_{load}/T_1 case to have equal maximum displacement response in the longer model updating window. This load adjustment is required to establish a fair comparison of the parameter estimation accuracy when loading period is widely changing in different cases.

The bilinear material behavior considered in these case studies is plastic, i.e., during the unloading phase the material takes its initial stiffness. Based on this assumption, the instantaneous fundamental period of these single- and multi-DOF systems change between two values; elastic period of vibration and elongated period which is bounded to $[1/\sqrt{0.8} \quad 1/\sqrt{0.2}]T_1 = [1.12 \quad 2.34]T_1$. In order to compare the results of all the cases considered, fundamental period of vibration (in elastic range) is selected. Since the elongation bound is constant in all the considered scenarios, this would not change the interpretation of results in terms of the "fast" or "slow" loading.

A 2-dimensional lumped mass FE model is developed in Opensees software (Mazzoni et al. 2009) using fiber section procedure, Steel01 uniaxialMaterial model, and non-linearBeamColumn elements. This FE model consists of 10 frame elements, 11 nodes, and overall 30 DOFs. A transient analysis object is used to apply the Newmark method integrated with the Krylov-Newton (Scott and Fenves, 2010) to solve the non-linear equiation of motion in each case with a time step of 0.001 sec.

In order to study characteristics of noise signals as samples of a desired Gaussian population, for each case of T_{load}/T_1 ratio, 50 rounds of simulations are conducted for the same noise level. In every scenario, two time windows were used for the parameter estimation: (1) a T_1-sec long window, and (2) a T_{load}-sec long window. The steps of RS model construction and validation in each case is carried out in the longer window between (1) and (2). It should be noted that when $T_{load}/T_1=0.2$, due to rapid change of the stiffness of the beam elements under high frequency loading, the response of beam is not predictable so the regressed RS models fail to estimate the response of the FE model over the entire domain of α. Therefore, RS model evaluation is not possible, and thus the optimization step is not completed in the cases corresponding to loading with this period.

Figures 4.12 and 4.13 show the error sensitivity of the median estimated α for all of the 50 simulations when T_{load}/T_1 is 20, 2, and 0.4, and with the assumption of $\alpha_{true}=0.625$ and 0.2, respectively. These figures show that the estimated α has larger variation as the noise level increases. When $\alpha_{true}=0.2$, the estimation error is sensitive

to the length of the selected time window, such that model updating in a longer time window, results in higher estimation error.

Figures 4.14 to 4.17 display the estimation error of the median of the estimated α in all the 50 cases associated with each noise level and T_{load}/T_1 ratio. These figures show that as the noise level increases, the estimation error increases particularly when α_{true} is at the corner of the selected RS domain. Furthermore, the estimation error in the cases with the largest ratio of T_{load}/T_1 appears to have the least sensitivity to the noise level and the selected time window. The reason is that when the vibration frequency of the system is outside of the frequency bandwidth of the load, the response of the model at different levels of the uncertain model parameters has the same frequency content as for the loading (a "steady-state" response). Therefore, the results of the model parameter estimation in time are robust to high measurement noise level and selected time window.

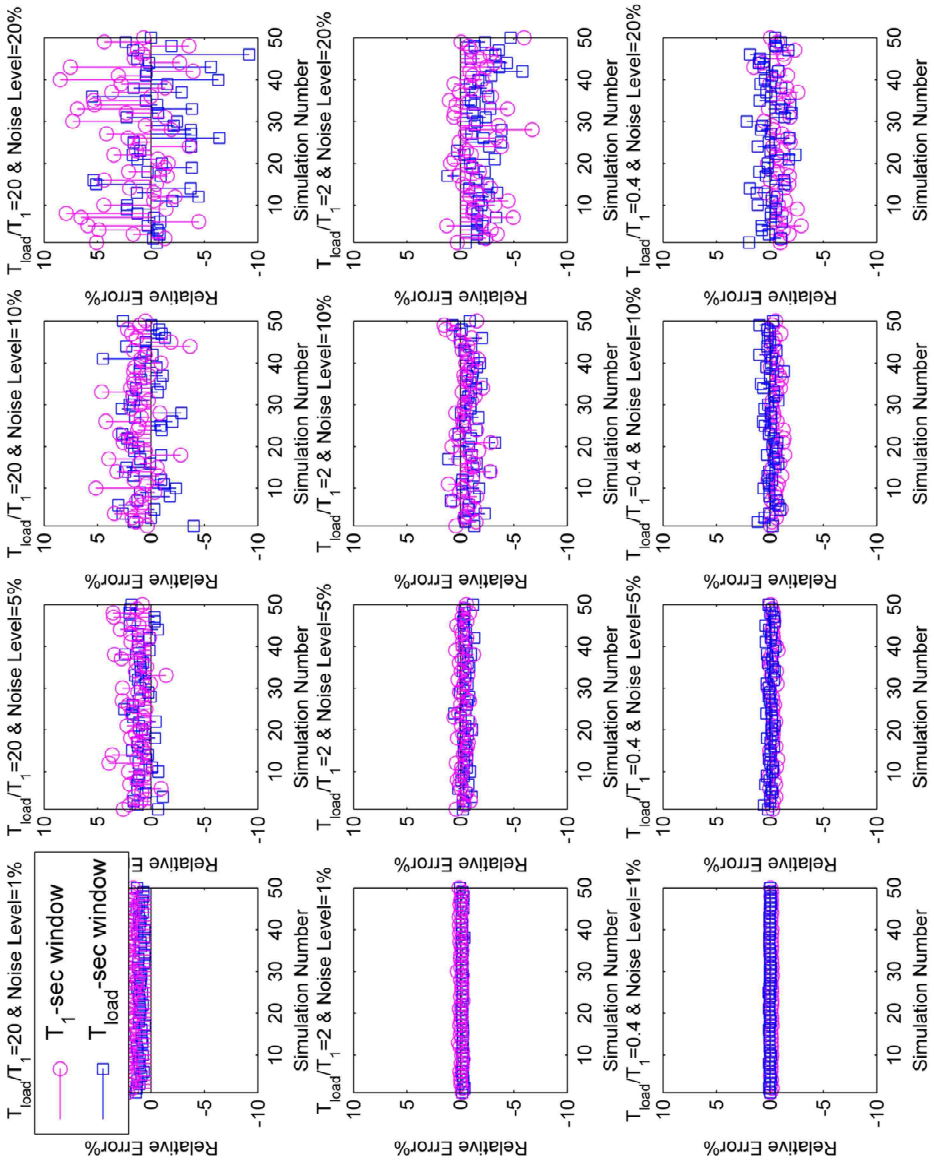

Figure 4.12. Error sensitivity of the median estimated α, 50 noise signal simulations: (Multi-DOF system, α_{true}=0.625)

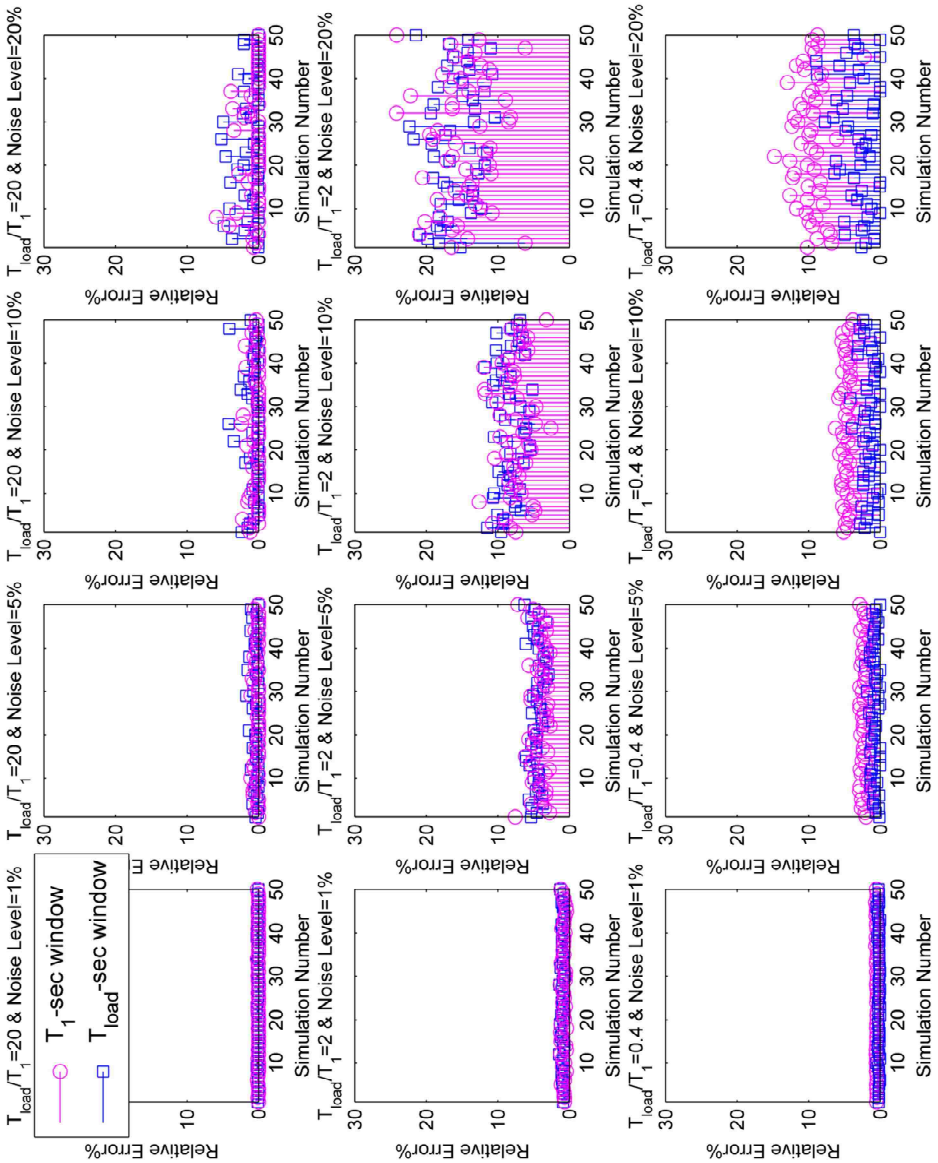

Figure 4.13. Error sensitivity of the median estimated α, 50 noise signal simulations: (Multi-DOF system, α_{true}=0.2)

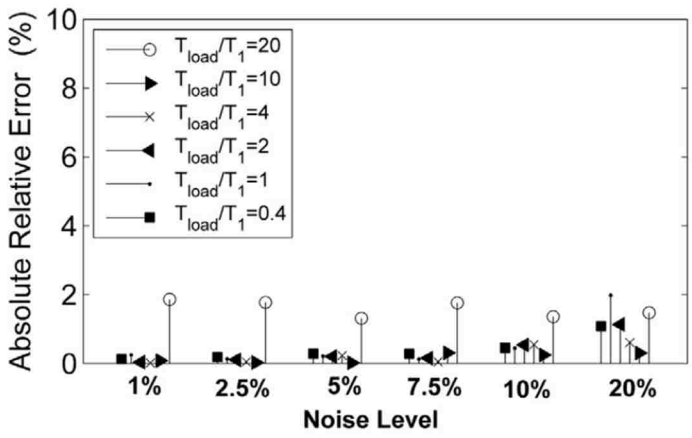

Figure 4.14. Error sensitivity of the median of the median estimated α (Multi-DOF system, α_{true}=0.625): T_1-sec long window

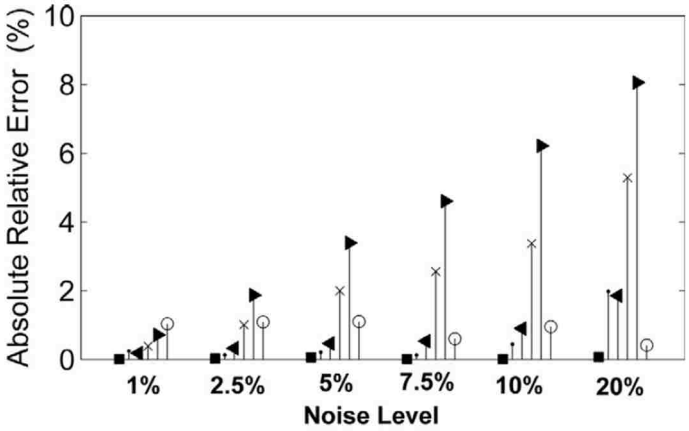

Figure 4.15. Error sensitivity of the median of the median estimated α (Multi-DOF system, α_{true}=0.625): T_{load}-sec long window

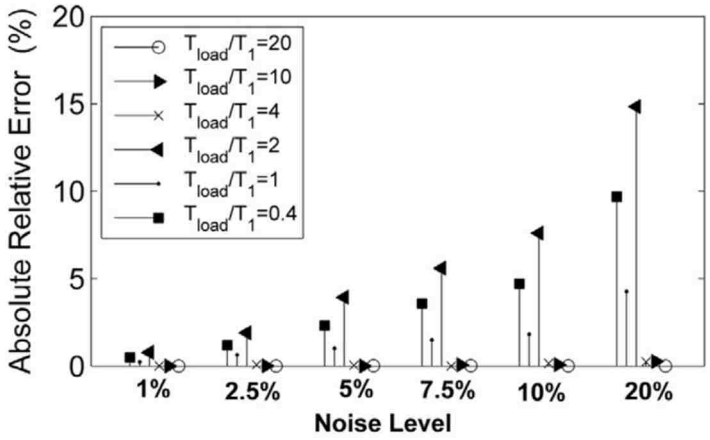

Figure 4.16. Error sensitivity of the median of the median estimated α (Multi-DOF system, α_{true}=0.2) T_1-sec long window

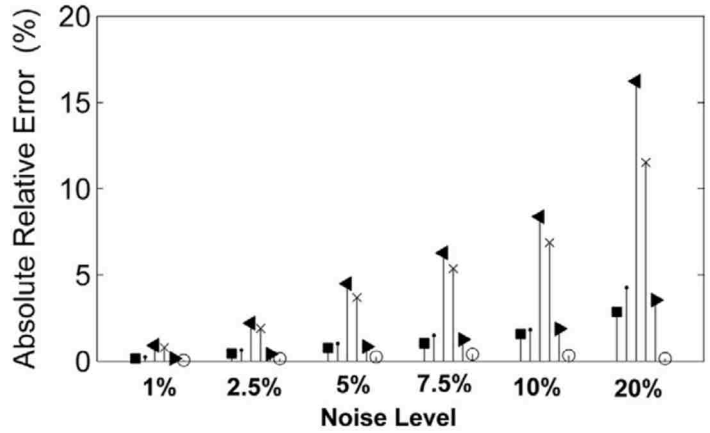

Figure 4.17. Error sensitivity of the median of the median estimated α (Multi-DOF system, α_{true}=0.2) T_{load}-sec long window

4.2.3. Effect of damping

In order to study the effect of damping in the performance of GRSMU, different levels of damping are considered for the non-linear cantilever beam. In these simulations, Rayleigh damping is assumed, and the mass- and stiffness-proportional

damping coefficients are designed so that 1st and 5th natural modes of vibration of the beam have 0.02, 0.05, and 0.1 damping ratios in different cases. Two levels of loading period (T_{load}/T_1), and four levels of noise contamination are considered. Parameter estimation is carried out in T_1-sec and T_{load}-sec long widows. The results of parameter estimation (shown in Figure 4.18) are consistent with the observations in the previous sections; when frequency of loading is high relative to natural frequency of the system, estimation error is sensitive to the length of optimization window.

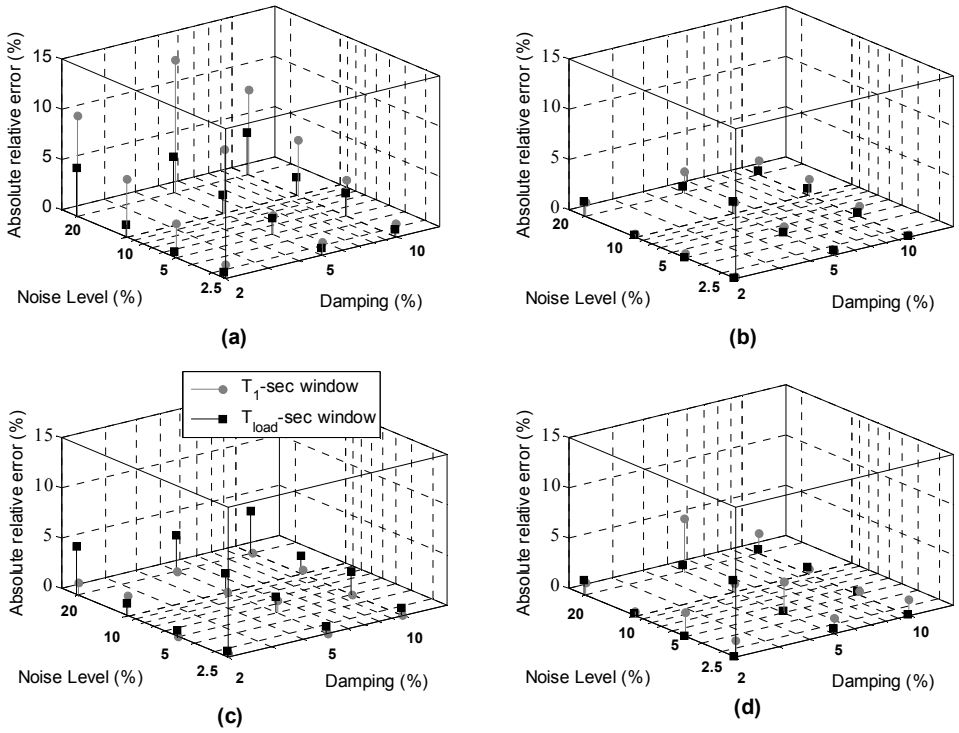

Figure 4.18. Error sensitivity in estimated α: (a) T_{load}/T_1=0.4 and α_{true}=0.2 and (b) T_{load}/T_1=0.4 and α_{true}=0.625 (c) T_{load}/T_1=20 and α_{true}=0.2 and (d) T_{load}/T_1=20 and α_{true}=0.625

4.3. Non-linear Model Updating Using Seismic Data

The previous section demonstrated that GRSMU estimates show robustness to the measurement noise, particularly in the cases where the input excitation has lower frequency content than the fundamental frequency of the system. This implies further application of this method in updating parameters of non-linear models in time under seismic loading. To validate such application, in this section a steel frame with bilinear material model is considered.

Details of the simulated steel frame, description of the factors considered to study the variability of the results, and the results of the updating procedures are presented in the following subsections.

4.3.1. Non-linear frame

The model presented in this section is a steel frame with non-linear material properties under dynamic loading. The frame consists of one span with overall length of 7' 6" (228.6 cm) supported by columns that are 2' 9" (83.8 cm) long. The cross section of the beam and column members is uniform hollow 2" (5.08 cm) tube, with 0.083" (0.21 cm) wall thickness. The column supports are fixed and the frame is considered a "plane frame" which constrains out-of-plane and torsional degrees of freedom. The steel has bilinear behavior with the yield stress of 50 ksi (344.8 MPa). Modulus of elasticity (E) and post yielding stiffness ratio of steel (b) are chosen as the updating parameters. The input excitation in this model is a dynamic load resulting from selected earthquake records applied to the left column-beam joint. To update the

pre-selected parameters of the model, simulated time histories of displacement at two locations on the frame are used. Figure 4.19 shows the configuration of the frame, loading and responses used for updating the FE model.

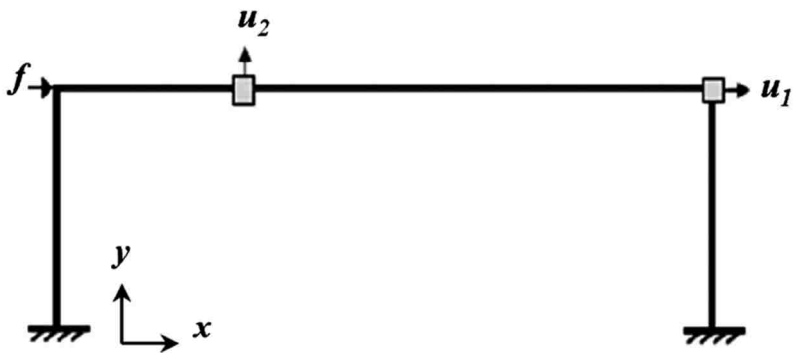

Figure 4.19. Configuration of the non-linear steel frame

4.3.2. Simulated model

A 2-dimensional massless model is developed in Opensees software (Mazzoni et al. 2009). The model consists of 8 nodes and 7 elements dividing beam and columns members into two and three segments, respectively. Each node has three degrees of freedom, ux, uy and θz which allow for translation and rotation in xy plane. Elements are modeled as non-linearBeamColumn having Steel01 uniaxialMaterial properties to construct a bilinear steel material object with kinematic strain hardening. Five integration points were assigned along each element to model the distributed plasticity. A fiber section procedure is used to build the tubular steel section from 92 fibers patched together. Due to zero-mass assumption for the steel tube section, the behavior of the system is not dynamic, and thus static or transient analysis objects with appropriate integrators can be used to solve the equation of motion under seismic

loading. In this study, a transient analysis object is used to apply the Newmark method integrated with the KrylovNewton algorithm (Scott et al., 2010).

The main purpose of studying these numerical simulations is to investigate the effect of frequency band limited excitations -at different measurement noise levels- on the GRSMU estimates. As shown in Section 4.2.3, this can be completed regardless of the damping level of the system. Therefore, for this non-linear frame model damping was not considered.

4.3.3. Parametric study

In order to evaluate the performance of GRSMU algorithm using seismic loading, variability of the model updating results are studied by considering: earthquake loads with different characteristics; various assumptions for true model parameters; and several levels of noise to contaminate the simulated response of the structure.

In this simulation, the RS domain for the updating parameters is set to 27,000 to 33,000 ksi (186.2 to 227.5 GPa) for E and 0.05 to 0.25 for b. Since the location of true model parameters in the RS domain is always unknown in the inverse problem of model updating, four pairs of model parameters are selected from the RS domain to simulate the measured responses of the non-linear frame under earthquake loading. Table 4.1 presents the true model parameters that are used for simulation.

Table 4. 1. Case studies of model parameters used to simulate the measured signals

	True model parameters		
	b	E(x10^3 ksi)	E(GPa)
Case (1)	0.065	27.5	189.6
Case (2)	0.05	33	227.5
Case (3)	0.18	28	193.1
Case (4)	0.125	31.5	217.2

Three earthquake records with different characteristics in terms of duration, fault distance, and frequency content are selected to study the sensitivity of the parameter estimation procedure to seismic input excitation. Figure 4.20 shows the time history and Fourier amplitude spectra of these ground motion records.

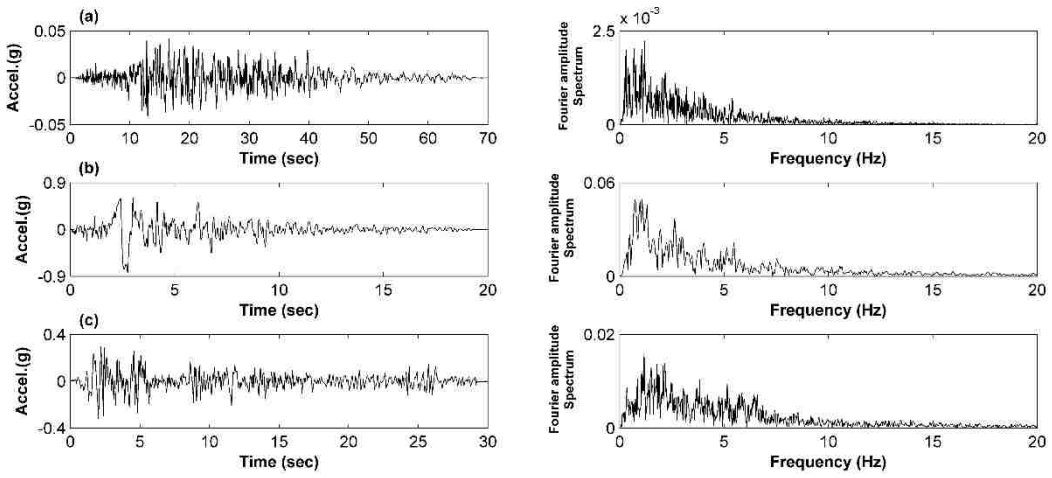

Figure 4. 20. Acceleration time history and Fourier amplitude spectra of: (a) Kern County earthquake (1952), (b) Northridge earthquake (1994), and (c) Imperial Valley earthquake (1940)

The selected earthquake records are: (1) Fault-normal component of Kern County earthquake (1952) recorded at LA Hollywood Stor Pe Lot station (PEER, 2013) which is a long duration far-fault record with a relatively long strong motion portion, (2) Fault-normal component of Northridge earthquake (1994) recorded at Rinaldi

Receiving station (PEER, 2013), a near-fault short duration record with a pronounced pulse in its time history, and (3) North-south component of horizontal ground acceleration of the Imperial Valley earthquake (1940) recorded at EL Centro station (PEER, 2013) which has a frequency content more uniform than the first two records and a relatively medium length strong shaking part. These earthquake records are scaled to simulate a dynamic lateral force at floor level which creates 1 in (2.54 cm) maximum $u_1(t)$, when model behaves linearly with E=33,000 ksi (227.5 GPa). The effect of measurement noise is also investigated by contamination of the simulated reference responses with Gaussian noise signals with different standard deviations.

4.3.4. Parameter estimation using GRSMU

The unknown model parameters are estimated based on the measured responses of the frame in 60 simulated scenarios resulting from three different input excitation, 4 different pairs of true model parameters, and 5 different levels of measurement noise. The model construction and evaluation steps of the GRSMU algorithm resulted in a 5x3 design for b and E. The RS models regressed on this design have model order of 4 for b, and 2 for E. In the optimization step, the resulting optimization problem in Eq. (1) is formulated and solved iteratively in a window selected from the response of system to the strong motion segment of each earthquake loading. Table 4.2 summarizes the information regarding the model updating window associated with each earthquake loading case.

Table 4.2. Details of the steel frame model calibration using Earthquake records

	Earthquake Record	ts_{opt} *(sec)*	te_{opt} *(sec)*	dt_{FEA} *(sec)*	dt_{opt} *(sec)*	N_{opt}
EQ(1)	Kern County	11.95	21.5	0.005	0.010	955
EQ(2)	Northridge	2.4	3	0.001	0.001	600
EQ(3)	Imperial Valley	1.66	4.8	0.002	0.004	785

1: beginning of the time window used in the model calibration
2: end of the time window used in model calibration
3: time step used in finite element analysis (FEA)
4: time step used for parameter etimation in the selected time window
5: number of time steps used in the parameter estimation

In order to find the global minimum of the formulated objective function at each time step, a multi-start optimization framework is adopted based on interior-point algorithm (Nocedal and Wright 2006) using four corners of the RS domain as starting point. Figures 4.21 and 4.22 display the histograms of the updating parameters using EQ (1) record to simulate the input seismic loading on the frame. These figures show that GRSMU successfully estimates the model parameters regardless of the location of the true model parameters in the selected RS domain. The parameter estimation procedures are reiterated to capture the variability of the results with respect to the input excitation and noise level in each case. Figure 4.23 summarizes the estimation error in all the 60 cases considered in this study. This figure indicates low error sensitivity of GRSMU estimates to measurement noise level in all cases with the exception of case (2) with high level measurement noise. Moreover, it is observed that the results are not sensitive to the choice of the ground motion record used for earthquake loading simulation.

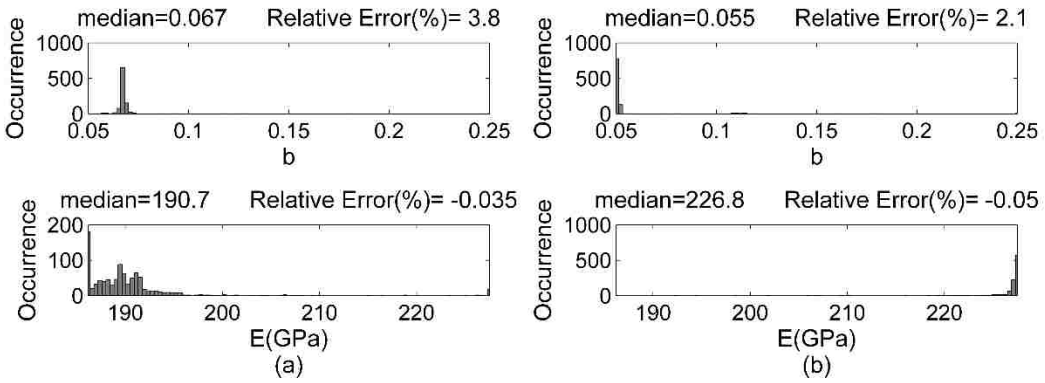

Figure 4.21. Histograms of the updated parameters using EQ (1) record (noise-free data): Case (1), (b) Case (2)

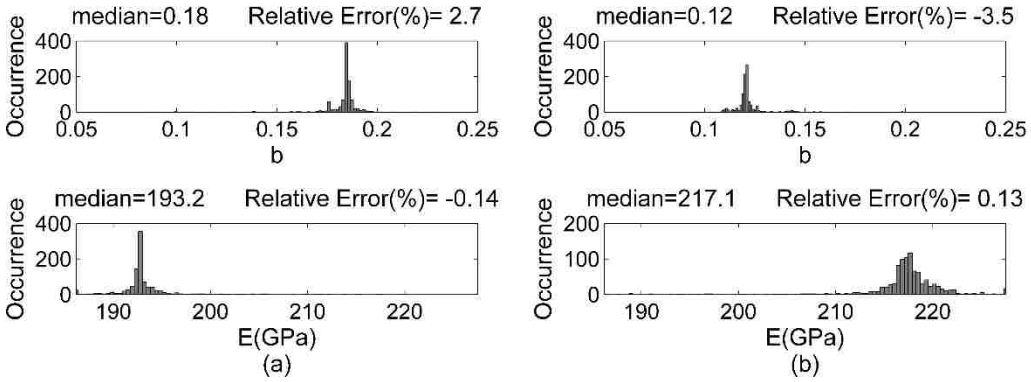

Figure 4.22. Histograms of the updated parameters using EQ (1) record (noise-free data): Case (3), (b) Case (4)

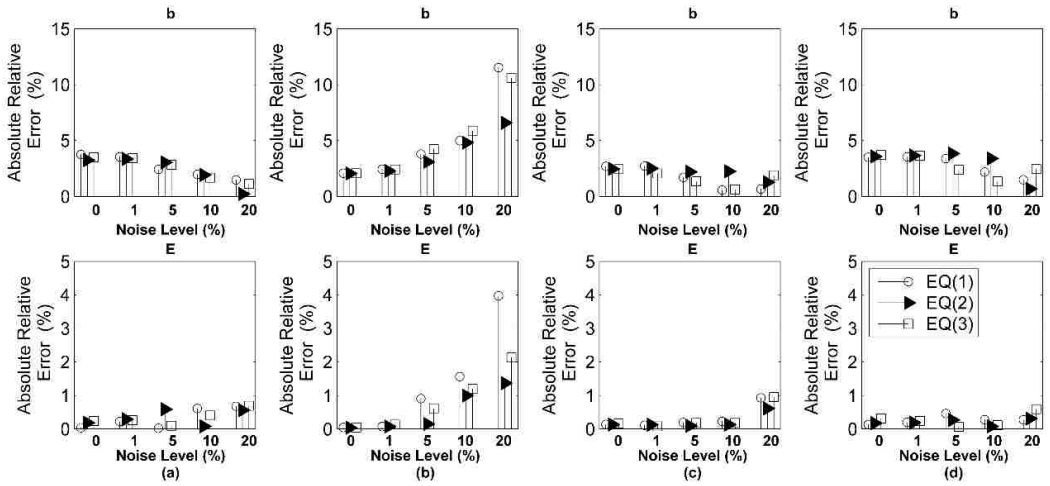

Figure 4.23. Error sensitivity in parameter estimation of the steel frame: case (1), (b) case (2), (c) Case (3) ,and (d) Case (4)

4.4. Summary and Conclusions

GRSMU is a generalized procedure for non-linear model updating using time-domain data. In GRSMU, the parameter estimation is accomplished through approximation of the input-output relationship of the non-linear FE model with RS models, and optimization of an objective function based on measured response and regressed RS models successively through the time history of the measured data. This chapter is primarily concerned with the sensitivity of GRSMU estimates to noise, since a reliable parameter estimation technique should be robust to measurement noise which inevitably exists in any monitoring data.

In this study, with the assumption of White Gaussian measurement noise, it is analytically shown that the GRSMU estimates have low sensitivity to the standard deviation of the noise. Numerical simulations of non-linear systems with several assumptions for measurement noise level, input excitation, true updating parameters,

and time-domain window for parameter estimation are used to validate this methodology. The results of the estimation of the post yielding stiffness ratio of the material in these systems through GRSMU show that the estimation error is fairly insensitive to low and medium measurement noise level. Additionally, when the vibration frequency of the system is outside of the frequency bandwidth of the load, the results show the least sensitivity to measurement noise level, selected time window for optimization, and location of the true model parameters in the RS domain.

Further application of GRSMU is also studied through a case study of a steel frame with bilinear material under seismic loading. In this simulation, three earthquake records with different characteristics in terms of duration, fault distance, and frequency content are selected to capture the variability of the parameter estimation results. The uncertain model parameters are successfully estimated based on the measured responses of the frame in 60 simulated scenarios resulting from 3 different input excitation, 4 pairs of true model parameters, and 5 increasing levels of measurement noise.

It should be noted that as this study is mainly concerned with evaluation of the overall performance of GRSMU algorithm, uniform spatial distribution is assumed for the unknown model parameters. In model-based damage detection scenarios, different spatial distribution could be possibly assumed in order to locate and quantify the structural damage.

Chapter 5

Assessment of the 2011 Virginia Earthquake Damage and Seismic Fragility Analysis of the Washington Monument

The 2011 Virginia Earthquake underlines the need to assess seismic vulnerability of structures in the Central and Eastern United States (CEUS), where according to the United States Geological Survey (USGS), due to the unique geological and geotechnical conditions, ground shaking although less frequent can be felt over a significantly broader region compared to similar events in the Western United States, and therefore the consequential damage is expected to be more widespread. One example of this phenomenon is the damage observed in the Washington Monument following the August 2011 Virginia Earthquake, which occurred despite being located over 130 km away from the epicenter of this 5.8 Mw earthquake in Mineral, VA. Several damage observations in this structure were reported including cracks, surface spalling, and dislodging of stone blocks in the pyramidion, crumbled mortar, as well as damage to the elevator (Wiss, Janney, Elstner Associates, Inc. 2011). The structure was immediately evacuated and remained closed to public for nearly three years to

complete the repairs to the Monument. Due to architectural and national significance of this structure, it is of substantial interest to study the possibility of damage to this structure under future seismic events. Such a prediction is beneficial for decision making in regards to the development of health monitoring plans for the structure.

This chapter investigates the fragility of the Washington Monument at different seismic hazard levels. For this purpose, a finite element model (FEM) of the structure is developed and calibrated with reference to the dynamic characteristics of the structure identified through ambient vibration measurements (Shahidi et al. 2015a). The updated model is then used to study the behavior of the structure during 2011 Virginia earthquake to explain the potential causes of the observed damage following this event. Finally, a fragility analysis is performed to study the probability of occurrence of similar structural and non-structural damage states in the future.

The focus of this chapter is the causes of damage to the shaft of Monument during Virginia earthquake as well as the possibility of damage to the shaft in the future. While the effect of top section of the structure -which is called pyramidion- on overall dynamic behavior of the Monument is included in the FEM, this section is not modeled in detail due to lack of available information for modeling as well as interior access for sensor deployment and structural identification of such a complicated system. Wells et al. (2015) presents a vulnerability assessment on the Monument, where pyramidion section was modeled in more details; however, the FEM developed in that study was not validated with the vibration characteristics of the structure, and

vibration periods appear to deviate from measured vibration periods presented in this chapter.

5.1. Washington Monument: Structural Description

This section briefly describes the construction history and structural details of the Washington Monument. Construction of this structure was completed in two phases with a two-decade suspension due to lack of funding and the occurrence of the Civil War.

During the period of 1848 to 1856 a 23.3 ft. (7.1 m) deep stair stepped pyramid foundation having a square base with 80 ft. (24.4 m) long sides was constructed of blue gneiss. Marble and bluestone masonry walls that were 55.5 ft. (16.9 m) wide and 15 ft. (4.57 m) thick at the ground level were raised to about 156 ft. (47.5 m).

During the period of 1879 to 1884 a second phase of construction occurred involving the strengthening of the original foundation using a system of tunneling and filling with concrete. The new foundation with a base of 126 ft. 5.5 in. (38.5 m) long at each side and a depth of 36 ft. 10 in. (11.2 m) fully encased the primary foundation in concrete (John Milner Associates, Inc. 2004). Construction of walls was resumed by first reducing them to a height of 150 ft. (45.7 m), and then rising them to the 500 ft. (152.4 m) level to create a shaft. These walls are 34.5 ft. (10.5 m) wide and 1.5 ft. (0.46 m) thick at the top, are made of marble and granite below the 450 ft. (137.2 m) level and marble from the 450 ft. (137.2 m) to 500 ft. (152.4 m) level. Finally, the pyramidion section was built from 500 ft. (152.4 m) to 555.4 ft. (169.3 m), making the height of the Monument approximately ten times its baseline dimension. Figure 5.1

shows vertical and horizontal sections of this structure based on a historic blueprint (Historic American Engineering Record 1986). This historic blueprint provides some information about the inner structure of the Monument, which consisted of horizontal platforms and staircases located at every ten feet (3.05 m) along the height of the structure, vertical columns supporting the platforms and staircases, and an elevator shaft which runs through the center of the Monument. More detailed blueprints of the interior structure (Oehrlein and Associates Architects 1993) show eight columns, running vertically over the height of the Monument (See Figure 5.2). These columns are called "Phoenix Column" and are each a circular pipe column made of iron, commonly used during the time of this construction.

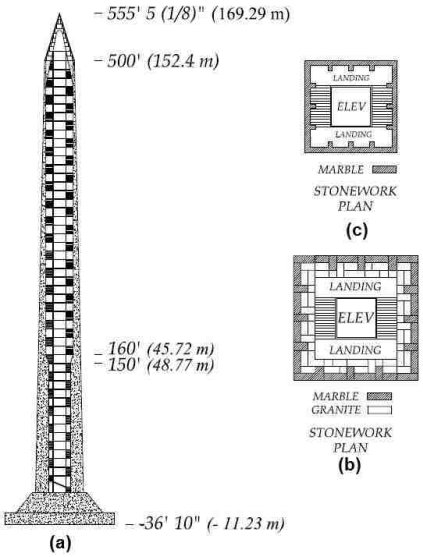

Figure 5.1. Washington Monument: (a) vertical section through north and south walls, (b) horizontal section at 180 ft. (54.9 m) level, and (c) horizontal section at 480 ft. (146.6 m) level

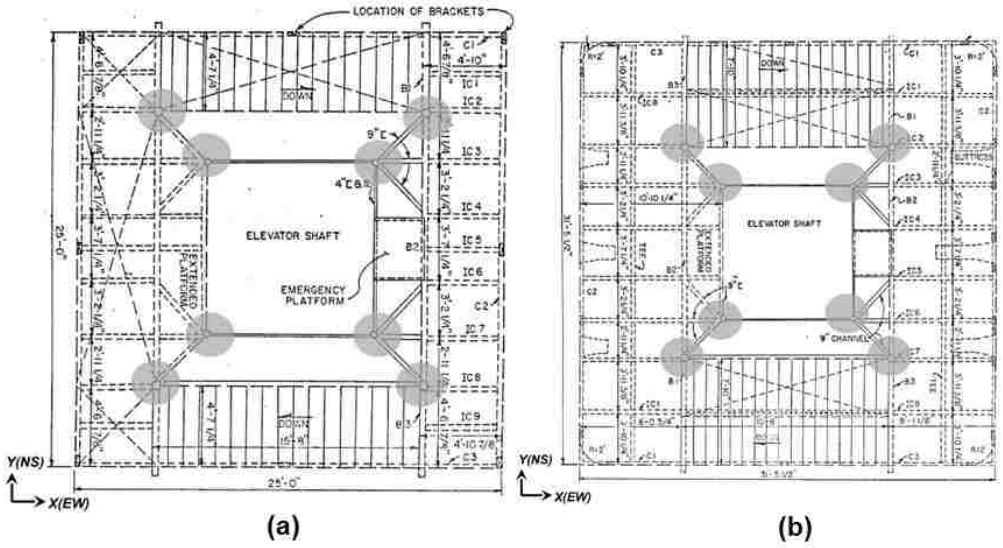

Figure 5.2. Detailed interior structure of the Washington Monument. (a) 150 ft (45.7 m) level and (b) 160 ft (48.8 m) level (Oehrlein and Associates Architects, 1993) Note: Gray circles represent vertical iron Phoenix columns (Note: 25' = 7.6 m and 31'-5 ½" = 9.6 m)

5.2. Post-earthquake Assessment of the Washington Monument

The Washington Monument suffered damage during the 2011 Virginia earthquake causing it to be closed to the public until repairs could be completed (planned for early 2014). The main types of damage observed in the Monument were cracking and spalling of the exterior stone. Cracking and spalling occurred over the entire height of the structure, with a larger density of cracking occurring in the pyramidion as well as the upper section of the shaft around 450 ft. (137.2 m) level. Figure 5.3 shows examples of cracking in the marble pyramidion panels. The crack shown in Figure 5.3(a) is approximately 4 ft. 4 in. (1.32 m) in length and 7 in. (0.18

m) deep, and cuts through the entire depth of the marble panel. Figure 5.3(b) shows a close-up view of cracking of a previously repaired crack in a pyramidion panel.

Examples of the observed spalling are provided in Figure 5.4, where Figure 5.4(a) displays spalling of the corner of a marble pyramidion panel and Figure 5.4(b) shows a complex spall at a previously repaired corner.

It should be noted that some of the observed damage had been documented in previously published historic assessment reports and did not necessarily occur during the 2011 Virginia earthquake. In order to investigate this issue, Figure 5 presents a timeline of the documented condition surveys of the Washington Monument. Figure 5.5(a) shows the condition of the exterior stones of the Monument in 1934 (John Milner Associates, Inc. 2004); where the spalling was more severe below the 150 ft. level of the shaft. Figure 5.5(b) displays the results of a crack survey on the exterior of the Washington Monument published in 1993, which shows two main categories of cracking on all faces of the Monument: (1) lower level cracks, running between the 160 ft. (48.8 m) and 234 ft. (71.3 m) levels, and (2) the upper level cracks, above the 450 ft. (137.2 m) level (Oehrlein and Associates Architects 1993). Figures 5.5(c) and 5.5(d) respectively, show vertical cracking above the 150 ft. (45.7 m) level (west elevation) and 420 ft. (128 m) level (inside) the Monument, documented in 2004 (John Milner Associates, Inc. 2004). Figures 5.5(e), (f) and (g) are from the post-earthquake assessment of the Washington Monument performed by Wiss, Janney, Elstner Associates, Inc. (2011). These figures show the loss of mortar in a vertical joint above the 450 ft. (137.2 m) level, the cracking of a previously repaired vertical joint on the west elevation and deep spalling on the west elevation near the pyramidion. Finally,

Figure 5.5(h), published in The Washington Post (July 9, 2012), shows the damaged masonry stones of the Monument on its four elevations. These observations from the timeline imply that the 2011 Virginia earthquake-induced damage on the Washington Monument is most likely on the pyramidion and upper as well as the middle levels of the masonry shaft.

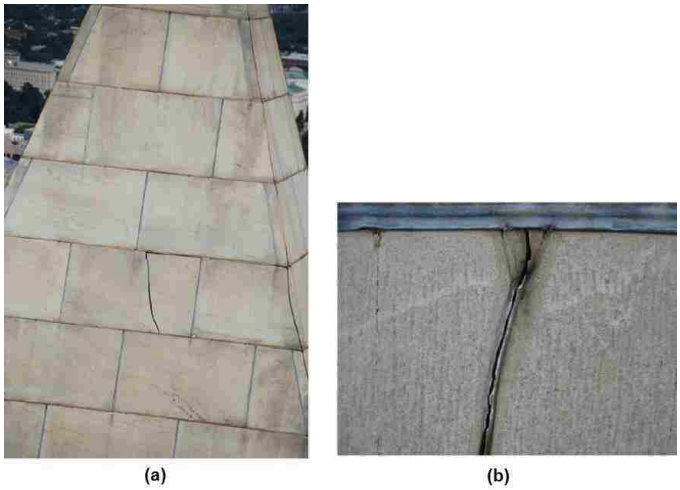

Figure 5.3. Cracking in pyramidion of the Washington Monument. (a) A newly developed crack on the west face of the pyramidion (b) Additional cracking along a historic crack (Wiss, Janney, Elstner Associates, Inc., 2011)

Figure 5.4. Spalling of pyramidion panels of the Washington Monument: (a) North face, (b) Northeast corner (Wiss, Janney, Elstner Associates, Inc., 2011)

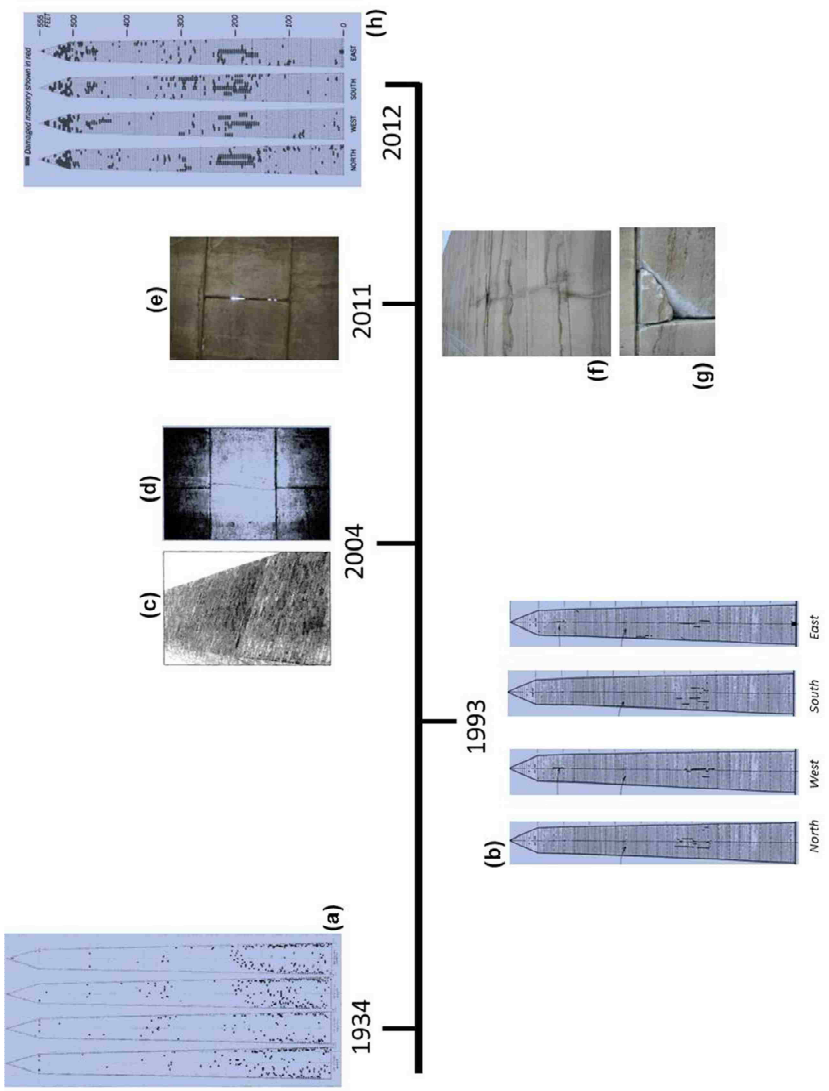

Figure 5.5. Timeline of the Washington Monument condition survey

5.3. Structural Modeling

This section describes the procedure adopted in this study to create the finite element model of the structure. In the analytical modeling of Washington Monument, like any other structural systems, a number of assumptions are made, particularly in terms of material properties. Hence, the calibration of the model with

the vibration characteristics of the structure from field testing is essential prior to deriving any conclusions regarding the causes of the damage due the earthquake.

Information obtained from the blueprints of the Monument was used to construct a 3D finite element model of the structure using the computer program SAP2000 (Computer and Structures, Inc. 2010). The overall dimensions used for the exterior of the Monument were a height of 500 ft. (152.4 m) from the base to the bottom of the pyramidion with baseline dimensions of 55 ft. 6 in. (16.9 m). The interior dimensions were 25 ft. (7.6 m) by 25 ft. (7.6 m) from the base up to the 150 ft. (45.7 m) level where they expand linearly to 31.5 ft. (9.6 m) by 31.5 ft. (9.6 m) at the 160 ft. (48.8 m) level and continue up to the 500 ft. (152.4 m) level. The wall thickness of the structure varied from 15 ft. (4.6 m) at the base to 1.5 ft. (0.46 m) at the top.

This study is primarily concerned with the modeling of the Washington Monument shaft, and thus the details of the pyramidion section were not included in the model. However, its effect was modeled as a distributed vertical gravity force at multiple locations from the 470 ft. (143.3 m) level (where the panels that support the pyramidion are integrated into the shaft's walls) to the 500 ft. (152.4 m) level, adding up to the estimated weight of the pyramidion. Choosing the dead load as the source to define the nodal masses for the dynamic analysis, the corresponding pyramidion mass was added to the nodal lumped masses obtained from the solid elements in the FEM.

As shown in Figure 5.1 the outer walls of the Monument are constructed from a combination of marble and granite. Therefore, in the model, an average of the material

properties of these two types of stone was used. Table 1 shows the range of values for the modulus of elasticity and unit weight of granite, marble, and iron. 45 GPa and 85 GPa were used as lower and upper bounds of the modulus of elasticity of the stone and 165 pcf (25.9 kN/m^3) for its unit weight. The material model for iron was defined using 190 GPa and 210 GPa as lower and upper bound values, and 485 pcf (76.2 kN/m^3) unit weight.

The finite element model of the masonry shaft was constructed using 3D solid elements. In order to ensure the accuracy of the model, different meshes were developed by increasing the number of elements in each model (shown in Figure 5.6). Amongst these, the FEM with 5,600 solid elements (shown in figure 5.6(d)) was chosen since using a finer mesh of elements would change the natural frequencies of the model less than 0.1%. Phoenix columns were modeled with beam elements defined with pipe section properties. In order to include the effects of the stairs and platforms, diaphragm constraints are assigned to the inner nodes of the shaft at each ten foot level.

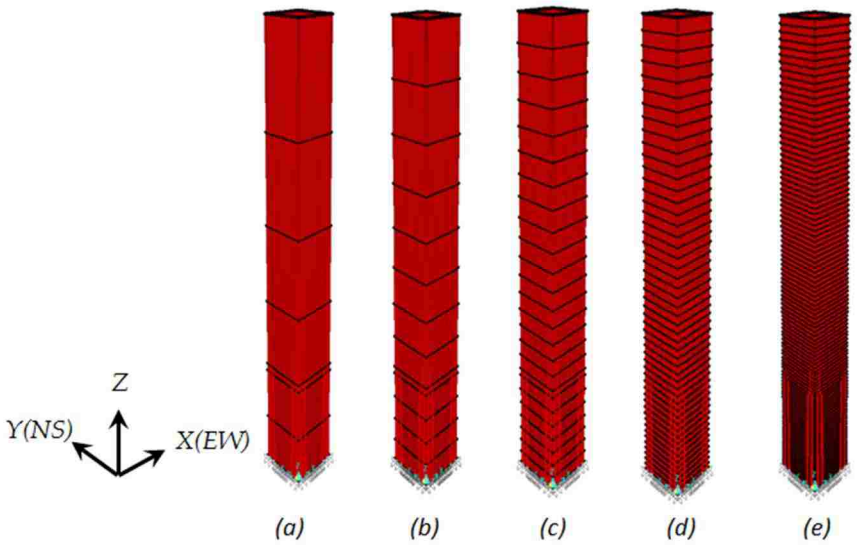

Figure 5.6. FEMs of the masonry shaft with (a) 784, (b) 1456, (c) 2800, (d) 5600, and (e) 11200 solid elements

The foundation was modeled as a lumped mass located at its center of mass and a group of uncoupled springs at the base of the foundation to represent the compliance of the sub-structure with respect to translation and rotation about all three principal directions of the model. The stiffness of these springs were calculated according to "Seismic Rehabilitation of Buildings" (FEMA 356). In this method, the foundation is assumed rigid with respect to the supporting soil, and hence the uncoupled spring model represents the stiffness of the surrounding soil. The equivalent spring coefficients are found based on the dimensions of the footing and effective shear modulus of the underlying soil. In this procedure, values for the unit weight and Poisson ratio of the soil were respectively assumed as 17 kN/m^3 and 0.2, and the average measured shear wave velocity of 1274.3 ft/sec (388.4 m/sec) of the soil strata to the base of foundation were used. Correction factors are applied in order to consider

the effect of the soil embedment on the foundation stiffness. Table 5.2 summarizes the stiffness of the springs used to model the sub-structure.

Table 5.1. Material properties of stone and iron

Material	Elastic modulus (GPa)	Elastic modulus (ksi)	Unit weight (lb/ft^3)	Unit weight (kN/m^3)
granite	40 - 70	5,801 - 10,152	168	26.4
marble	50 - 100	7,241 - 14,503	160	25.1
iron	190-210	27,557-30,458	485	76.2

Table 5.2. Description of the foundation springs

Spring	Degree of freedom	Stiffness	Unit	Stiffness	Unit
KX	Translation along X-axis	2.9322E+06		4.2806E+07	
KY	Translation along Y-axis	2.9322E+06	Kips/ft	4.2806E+07	kN/m
KZ	Translation along Z-axis	2.4159E+06		3.5268E+07	
KXX	Rocking about X-axis	9.2632E+09		1.2552E+10	
KYY	Rocking about Y-axis	9.2632E+09	Kips.ft/rad	1.2552E+10	kN.m/rad
KZZ	Torsion about Z-axis	1.9532E+10		2.6467E+10	

5.4. Parametric Study

In order to consider the uncertainty associated with the adopted modeling approach, as well as the impact of foundation modeling, different cases were studied by permutation of the material properties of the structure as well as the stiffness of the foundation springs. The average of the lower and upper bounds of elastic modulus of granite and marble were used as the lower and upper bound values of the modulus of elasticity of the stone throughout the shaft. Therefore, the lower bound of the stone modulus of elasticity was assumed to be equal to 45 GPa (average of 40 GPa and 50

GPa), and a value of 85 GPa (average of 70 GPa and 100 GPa) was used as the upper bound. The lower and upper bound values of the foundation stiffness were established using a factor of 0.5 and 2 to the stiffness calculated based on FEMA 356 to account for the uncertainty associated with the modeling of the foundation (FEMA 2000). To this end, twelve different cases of FEMs were studied where the first six cases are based on estimated lower and upper bound values for material properties and foundation stiffness, and the last six cases are based on assumption of average elasticity moduli for stone and iron, and foundation stiffness having values shown in Table 5.2.

In Case (1) the modeling of the foundation is not considered, and the iron and stone in the super-structure were modeled using the upper bound value of the moduli of elasticity given in Table 1. In Cases (2) and (3), upper and lower bound values of the foundation stiffness were considered, respectively, while the super-structure material properties are the same as that in Case (1). Three other permutations are made by assigning the lower bound moduli of elasticity to the masonry shaft and the Phoenix columns to create Cases (4), (5) and (6). In Case (4) the super-structure is modeled with the lower bound value of the material properties and is fixed at the ground level. In Cases (5) and (6), the lower bound values for the material properties of the super-structure are used; however, the foundation is modeled with upper bound (Case 5) and lower bound (Case 6) values. Case (7) is created by assigning average of lower and upper bound values of the moduli of elasticity (65 GPa) to stone and iron without including the foundation in the model. In Cases (8), foundation springs (having the values shown in Table 2) are added to this model. Case (9) and (10) are

created to study the effect of uncertainty in foundation stiffness when the super-structure is modeled with average of the bounds of the material properties. Finally, in Case (11) and (12) upper and lower values for the material properties of the super-structure are used, while foundation springs are modeled with values tabulated in Table 5.2. Table 5.3 summarizes the modeling assumptions of this parametric study.

Table 5.3. Description of the parametric study

	Super-structure material properties	Sub-structure stiffness
Case (1)	maximum moduli of elasticity	foundation was not modeled
Case (2)	maximum moduli of elasticity	maximum estimated stiffness
Case (3)	maximum moduli of elasticity	minimum estimated stiffness
Case (4)	minimum moduli of elasticity	foundation was not modeled
Case (5)	minimum moduli of elasticity	maximum estimated stiffness
Case (6)	minimum moduli of elasticity	minimum estimated stiffness
Case (7)	average moduli of elasticity	foundation was not modeled
Case (8)	average moduli of elasticity	from TABLE 2
Case (9)	average moduli of elasticity	maximum estimated stiffness
Case (10)	average moduli of elasticity	minimum estimated stiffness
Case (11)	maximum moduli of elasticity	from TABLE 2
Case (12)	minimum moduli of elasticity	from TABLE 2

Tables 5.4 and 5.5 present the results of modal analysis of these twelve cases. These tables show that the structural characteristics change extensively with the permutation of the material properties and the foundation stiffness. Additionally, modeling the foundation significantly affects the period and shape of the structural vibration modes in the model.

Table 5.4. Periods of vibration and description of the mode shapes, FEM cases 1–6

Mode number	Case (1)		Case (2)		Case (3)		Case (4)		Case (5)		Case (6)	
	P	M. D.	P	M. D.	P	M. D.	P	M. D.	P	M. D.	P	M. D.
1	0.809	trans-Y	1.014	trans-Y	1.495	trans-Y	1.112	trans-Y	1.266	trans-Y	1.667	trans-Y
2	0.809	trans-X	1.014	trans-X	1.494	trans-X	1.112	trans-X	1.265	trans-X	1.667	trans-X
3	0.218	trans-Y	0.288	trans-Y	0.414	axial	0.300	trans-Y	0.359	trans-Y	0.451	trans-Y
4	0.218	trans-X	0.288	trans-X	0.372	trans-Y	0.300	trans-X	0.359	trans-X	0.451	trans-X
5	0.116	torsional	0.211	axial	0.372	trans-X	0.159	torsional	0.217	axial	0.417	axial
6	0.099	trans-Y	0.146	trans-Y	0.216	trans-Y	0.136	trans-Y	0.175	trans-Y	0.246	trans-Y
7	0.099	trans-X	0.146	trans-X	0.216	trans-X	0.136	trans-X	0.175	trans-X	0.246	trans-X
8	0.073	axial	0.120	torsional	0.134	torsional	0.100	axial	0.162	torsional	0.172	torsional
9	0.058	trans-Y	0.097	trans-Y	0.114	trans-Y	0.080	trans-Y	0.117	trans-Y	0.148	trans-Y
10	0.058	trans-X	0.097	trans-X	0.114	trans-X	0.080	trans-X	0.117	trans-X	0.148	trans-X

P: Period (sec)
M. D. : Mode Discription

Table 5.5. Periods of vibration and description of the mode shapes, FEM cases 7–12

Mode number	Case (7)		Case (8)		Case (9)		Case (10)		Case (11)		Case (12)	
	P	M. D.	P	M. D.	P	M. D.	P	M. D.	P	M. D.	P	M. D.
1	0.925	trans-Y	1.272	trans-Y	1.107	trans-Y	1.556	trans-Y	1.193	trans-Y	1.409	trans-Y
2	0.925	trans-X	1.271	trans-X	1.107	trans-X	1.556	trans-X	1.193	trans-X	1.409	trans-X
3	0.250	trans-Y	0.354	trans-Y	0.315	trans-Y	0.415	axial	0.324	trans-Y	0.399	trans-Y
4	0.250	trans-X	0.354	trans-X	0.315	trans-X	0.402	trans-Y	0.324	trans-X	0.399	trans-X
5	0.132	torsional	0.296	axial	0.213	axial	0.402	trans-X	0.295	axial	0.298	axial
6	0.113	trans-Y	0.187	trans-Y	0.157	trans-Y	0.229	trans-Y	0.176	trans-Y	0.203	trans-Y
7	0.113	trans-X	0.187	trans-X	0.157	trans-X	0.229	trans-X	0.176	trans-X	0.203	trans-X
8	0.083	axial	0.140	torsional	0.136	torsional	0.148	torsional	0.125	torsional	0.165	torsional
9	0.067	trans-Y	0.118	trans-Y	0.105	trans-Y	0.128	trans-Y	0.107	trans-Y	0.134	trans-Y
10	0.067	trans-X	0.118	trans-X	0.105	trans-X	0.128	trans-X	0.107	trans-X	0.134	trans-X

P: Period (sec)
M. D. : Mode Discription

5.5. Ambient Vibration Measurements

In order to minimize the uncertainty in the finite element modeling of the Washington Monument, field vibration tests were conducted to establish the dynamic characteristics of the structure and use them as a basis to select the FEM case which

best represents the actual structure. This section presents the details of instrumentation, vibration monitoring, and structural identification of the Monument.

Ambient vibration measurement of the Washington Monument was conducted using a network of 8 sensors and a portable data acquisition system (DAQ) (shown in figure 5.7). The sensors are single channel accelerometers manufactured by Silicon Designs, Inc. (model number 2210-002). The DAQ has a 24-bit analog to digital convertor (ADC), with a quantization resolution of less than 1 μg. The sensors have a characteristic noise floor of 13 $\mu g/\sqrt{Hz}$, which for a signal filtered at 15 Hz translates to about 50 μg root mean squared (RMS) noise.

Two wired accelerometers were located at each corner of the masonry shaft of the Monument at the 491 ft. (149.7 m) level to measure the horizontal vibration of the structure in two orthogonal transverse directions. Figure 5.8(a) shows the layout of this sensor network and figures 5.8(b) and (c) show sensors A1 and A2 attached to the Washington Monument. Ambient vibrations were measured for over a 60 minute duration using a sampling frequency of 200 Hz (720,000 samples per channel).

Figure 5.9(a) shows the time history of the data collected at the southwest corner of the WAMO after removing the unwanted trend due to temperature change caused by wind and sunshine. This figure shows that the ambient vibration amplitude is about 300 μg. The collected data are further studied in the frequency domain. Figure 5.9(b) presents the average power spectral density (PSD) of the 8 measured signals obtained using the Welch method (Welch, 1967). This figure shows distinct peaks of

the PSD, corresponding to the natural vibration frequencies of the system. The peaks are distinct and clear, and repeat in data from all sensors.

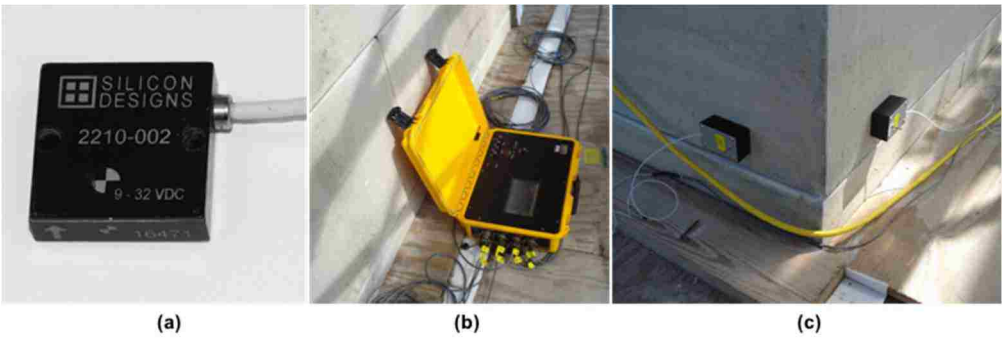

Figure 5.7. (a) Silicon Designs accelerometer, (b) Portable data acquisition system, (c) Single channel wired sensors at 491 ft. (149.7 m) level

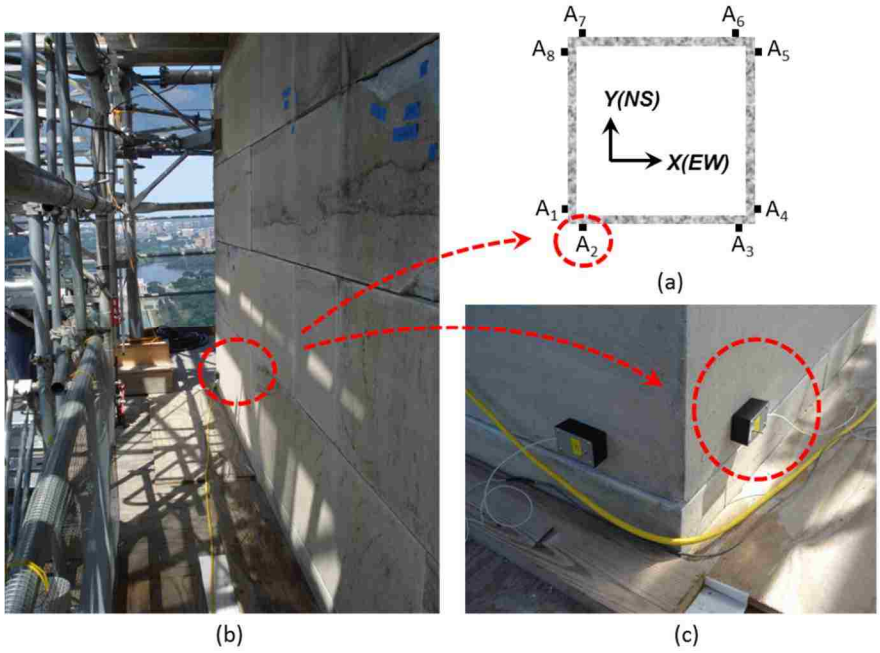

Figure 5.8. Instrumentation plan at: (a) 491 ft. (149.7 m) level; (b) and (c) sensors A_1 and A_2 attached to the southeast corner of the Monument

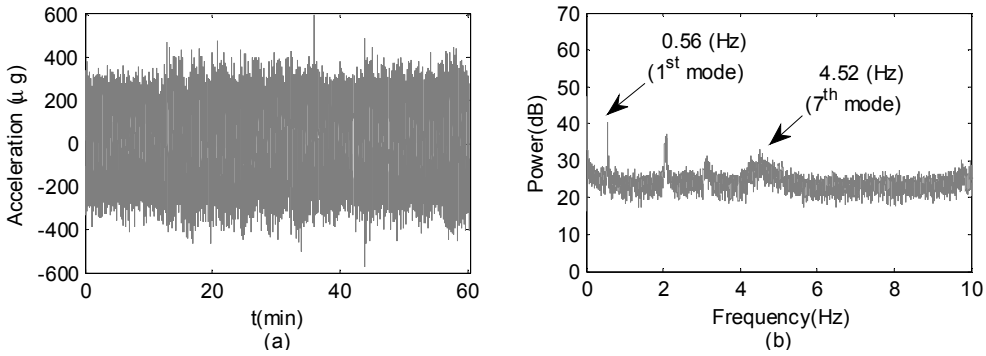

Figure 5.9. Acceleration measured through sensor A_1: (a) detrended time history, and (b) power spectral density

5.6. Modal Parameter Identification

Modal parameter identification is performed using the output-only Eigen Realization Algorithm (ERA-OKID). Using a software package developed at Lehigh University for convenient modal identification of dynamic systems [SMIT or Structural Modal Identification Toolsuite; Chang and Pakzad (2013)], the optimum model order was found from the stabilization diagrams (with convergence thresholds of 5%, 95%, and 10% for frequencies, MAC values (Allemang 2003) and damping ratios, respectively) and the modal properties were extracted. Figure 5.10 shows the stabilization diagrams created based on the ambient acceleration signals measured in the EW and NS directions. In these plots, the identified modal parameters at every model order are marked if they fall within the pre-specified stability threshold of the identified modal parameters at the previous model order.

Table 5.6 shows the first 7 identified structural modes using the entire data set. It should be noted that because the sensor deployment was located at only one level of the WAMO, no spatial information along the height of the structure for the mode shapes are available, and thus the modal ordinates are used to distinguish between modes in the two transverse directions and twisting (i.e., torsional modes). Moreover, since in this project a short-term ambient vibration analysis was conducted, a study of the effect of environmental factors on the dynamic characteristics of the Monument was not of primary focus.

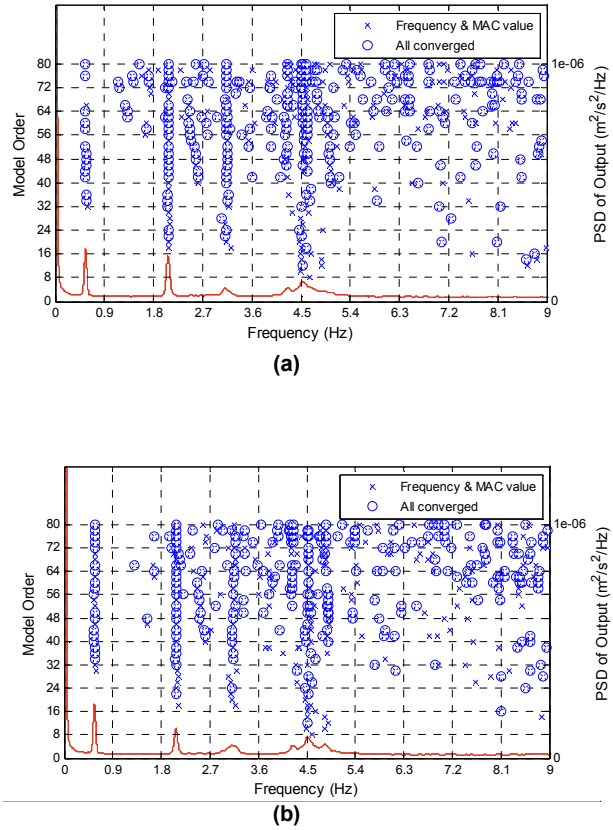

Figure 5.10. Stabilization diagrams in 0–9 Hz frequency range based on the acceleration signals. PSD—power spectral density; MAC—modal assurance criterion. (a) Measured in east-west (X) direction. (b) Measured in north-south (Y) direction.

Table 5.6. Dynamic characteristics of the Monument identified through measurements

Mode number	1	2	3	4	5	6	7
Period (sec)	1.79	1.78	0.484	0.482	0.319	0.317	0.221
Damping (%)	2.38	1.86	0.94	1.07	2.13	2.68	1.79
Modal ordinate elevation: 491 ft. (149.7 m) Y(NS) X(EW)	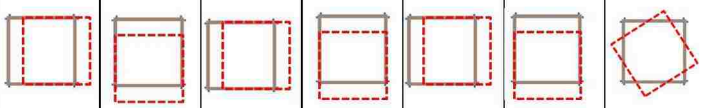						

5.7. *Baseline FEM*

The parametric study presented earlier showed that among all the cases, the one with lower bound values for the modeling parameters has the closest periods to the identified natural frequencies from the ambient vibration measurements. Therefore, the set of modeling parameters from this case is used to create a baseline FEM in which the effect of mass of the soil on top of the foundation was also considered. This model was created using ABAQUS (Dassault Systèmes 2013): (1) in order to cross-validate the previous SAP2000 modeling, and (2) because of its capability to assign non-linear material model to continuum elements to be able to perform fragility analysis. A comparison between the ABAQUS and SAP2000 baseline FEMs showed that these models are in good agreement; less than 1.8% and 6.5% relative difference exist, respectively, in the first 20 vibration periods and maximum tensile stresses predicted by the models. Table 5.7 summarizes the modeling parameters of this baseline model. In order to further minimize the estimation error of the developed FEM, the uncertainty associated with the modeling parameters are identified, and

subsequently a systematic search in domain of uncertain model parameters is conducted.

Table 5.7. Modeling parameters of the baseline FEM

Modeling parameter	value (unit)	value (unit)
weight of pyramidion	672 (kips)	305 (tons)
unit weight of masonry walls	0.165 ($kips/ft^3$)	2.64 (ton/m^3)
weight of foundation	6.79E+04 (kips)	3.08E+04 (tons)
weight of soil on top of foundation	2.31E+04 (kips)	1.05E+04 (tons)
elasticity modulus of masonry walls	9.3984E+05 (ksf)	45 (GPa)
stiffness of sub-structure along horizontal axes (x & y)	1.4669E+06 (kips/ft)	2.1414E+07 (kN/m)
stiffness of sub-structure along vertical axis (z)	1.2084E+06 (kips/ft)	1.7640E+07 (kN/m)
stiffness of sub-structure in rocking about horizontal axes (x & y)	4.6387E+09 (kips.ft/rad)	6.2855E+09 (kN.m/rad)
stiffness of sub-structure in twisting about vertical axis (z)	9.7849E+09 (kips.ft/rad)	1.3259E+10 (kN.m/rad)

5.8. FE model updating based on the identified modal quantities

As the first step for model calibration, the model parameters possessing uncertainty are identified. Model parameters describing the super-structure mass (i.e., mass of masonry walls and pyramidion section) and sub-structure mass (i.e., mass of foundation with soil on top of it) were verified through a comparison with previous estimations (Casey 1885). Therefore, the main sources of uncertainty in the FEM are the modulus of the elasticity of the masonry walls of the shaft and the spring model of the soil. Two separate parameters are considered to calibrate the moduli of elasticity of the shaft: P1 and P2. These two updating parameters are unitless factors to be applied to the moduli of elasticity of masonry material shown in Table 1 during the calibration procedure. P1 is applied to the modulus of elasticity of lower part of the shaft (0-150 ft. (0-45.7 m) elevation) and P2 is applied to the modulus of elasticity of the upper part of the shaft (150-500 ft. (45.7-152.4m) elevation). This distinction is made because the lower portion of the structure was constructed three decades earlier than the upper part. Also, the layout of these two sections are different; where the upper portion is made of marble and granite stone blocks and the lower portion has a layer of infill rubble masonry in between the interior and exterior stone wythes. It is expected then that the lower portion of the shaft will have a lower modulus of elasticity than the upper portion. The third uncertainty is represented by the parameter P3, where P3 is a unitless factor to be assigned to the spring model of the soil (shown in Table 5.6) in the calibration process.

Two calibration techniques are used to update the selected parameters of the FEM with reference to the identified vibration frequencies of the structure, and their results and computational costs are compared. First, a sensitivity-based method is used (Mottershead et al. 2010). In this method, an error function is formulated on the basis of a truncated Taylor series expansion of the natural periods of the model, written in terms of the uncertain model parameters and a sensitivity matrix consisting of first derivatives of the vibration periods with respect to the model parameters. Starting with an initial estimate for the model parameters, this error function is iteratively minimized by updating the model parameters and the sensitivity matrix associated with them. Convergence is achieved when the periods of the updated model fall within a certain threshold from the identified periods (5% in this study), or when further updating iterations does not change the updating parameters (a 1% threshold is used for the average change in the updating parameters in this study). Since convergence of this method depends on the choice of the initial set of the model parameters, and also to ensure that the updated model parameters correspond to global optima of the error function, the model updating process is repeated using several different initial values for the parameters. Table 5.8 summarizes the initial and final set of values for model parameters identified with uncertainty as well as their error in predicting the identified periods.

Table 5.8. Model updating results using sensitivity method

	initial values			RMSE[1]	updated values			RMSE	FEA
	P1	P2	P3	(%)	P1	P2	P3	(%)	count[3]
Case 1	0.5	0.5	0.9	10.5	0.56	0.67	0.96	6.3	17
Case 2	1	0.5	0.9	8.4	NC[2]	NC	NC	8.4	12
Case 3	0.5	1	0.9	7.8	0.56	0.68	0.95	6.3	37
Case 4	1	1	0.9	14.0	0.56	0.67	0.96	6.3	37
Case 5	0.5	0.5	1.4	8.1	0.56	0.67	0.96	6.3	33
Case 6	1	0.5	1.4	11.3	NC	NC	NC	11.3	8
Case 7	0.5	1	1.4	13.0	0.56	0.67	0.96	6.3	25
Case 8	1	1	1.4	20.7	0.56	0.67	0.96	6.3	41

[1] RMSE: root mean square error in estimating the periods T1 , T3, T5, and T7

[2] NC: no convergence

[3] FEA count: number of finite element analysis (FEA) in updating process

In the second calibration method, the GRSMU framework described in the previous chapters is used for model calibration. In this method, first, polynomial RS functions are trained to predict the response of the FE simulation in a pre-selected domain of model parameters. Then, the model updating problem is solved through minimization of the RS-based objective function shown in Eq. (5.1):

$$\min_{P1,P2,P3} \sqrt{\sum_i \left(\frac{RS_i(P1,P2,P3) - T_i}{T_i} \right)^2} \quad i = 1,3,5,7 \tag{5.1}$$

In this equation, T_i represents the i^{th} identified natural period (shown in Table 2), and RS_i denotes the RS model predicting the period of the FEM corresponding to T_i. In order to find RS models that are capable of predicting the response of the FE model throughout the domain of model parameters.The minimization problem is solved using the "*active*-set" algorithm (Nocedal and Wright 2006) in a multi-start framework

starting from all vertices of the selected RS domain, which are in effect the starting points used in the sensitivity-based procedure described previously. Figure 5.11 shows the search history of each parameter. It is observed that regardless of the starting points convergence is achieved, and updated parameters using this method confirm the results of the sensitivity-based analysis performed earlier. Moreover, the construction and validation of the RS models are completed with 33 FE analyses. Compared to the total number of FE runs associated with the sensitivity method (shown in Table 5.8), it is observed that the cost of the global search of the RS domain of uncertain model parameters are six times lower than the sensitivity method.

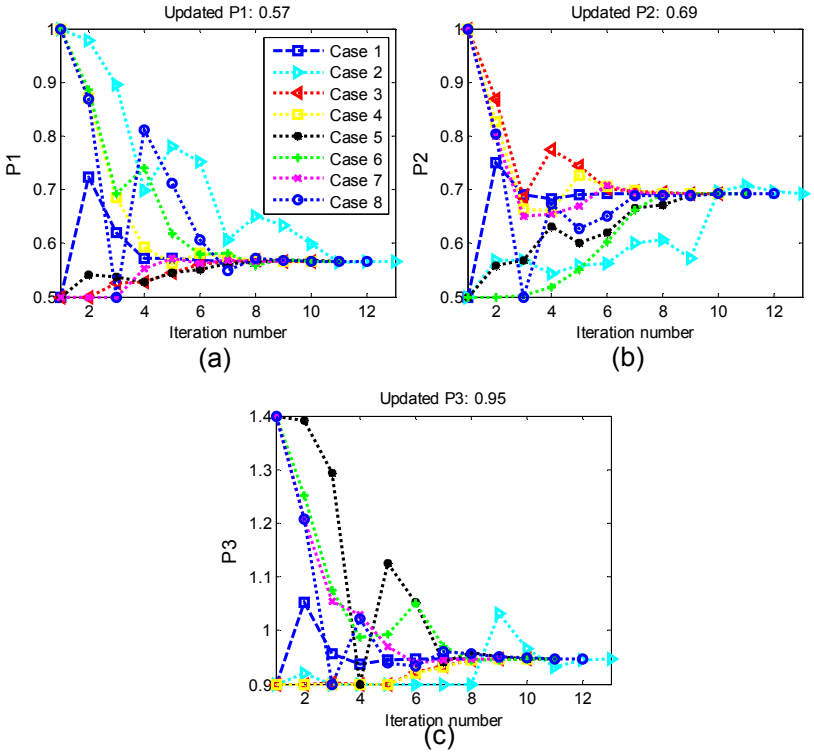

Figure 5.11. RS-based search history of the updating parameters: (a) P1, (b)P2, and (c)P3

Figure 5.12 presents four vibration modes of the updated FEM: the first-three translational modes in a transverse direction, along with the first torsional mode. Translational modes in the orthogonal transverse direction are not pictured here due to symmetry. Table 5.9, summarizes the vibration periods of the baseline and updated FEMs and their errors with respect to the identified vibration periods of the structure (shown in Table. 2). This table shows that the updated FE model (where P1=0.56, P2=0.67, and P3=0.96) better estimates the vibration periods of the Monument compared to the baseline FE model (where P1=1, P2=1, and P3=1).

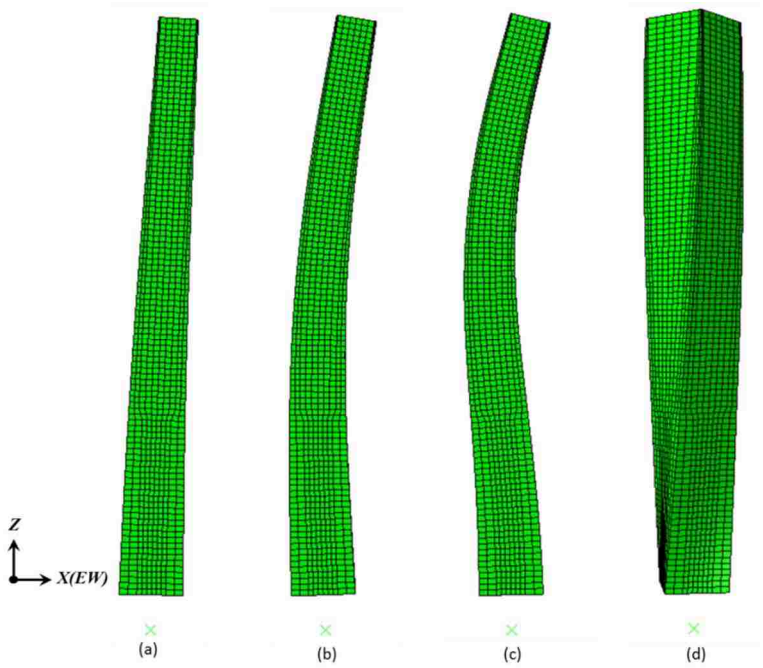

Figure 5.12. Vibration modes of the updated ABAQUS model, periods: (a) 1.874 sec, (b) 0.515 sec, (c) 0.289, and (d) 0.213 sec

Table 5.9. Comparison of the estimation error of FE model before and after model calibration with respect to the identified vibration periods from measurements

Mode number	1		3		5		7	
P: Period (sec) E: Error (%)	P(sec)	E(%)	P(sec)	E(%)	P(sec)	E(%)	P(sec)	E(%)
baseline FEM	1.632	8.827	0.449	-7.231	0.260	-17.981	0.171	-22.624
updated FEM	1.874	4.693	0.515	6.488	0.289	-8.896	0.213	-3.710

5.9. Virginia Earthquake (2011)

Recorded ground accelerations during the 2011 Virginia earthquake were used to investigate the behavior of the monument during this event. For this purpose, ground shaking at the foundation level (FL) of the Washington Monument was estimated based on the USGS recording of this earthquake in Reston, VA (Reston Fire Station 25). This choice is justified because this station is the closest USGS station to the site (about 31 km away) and Reston and Washington, DC have comparable distances with respect to the epicenter of the earthquake, Mineral, VA (both located northeast of Mineral, VA about 122 km and 130 km away, respectively). Shear wave velocity profiles at these two sites were measured by USGS and used to estimate the ground shaking at the site of Washington Monument during the earthquake based on the recorded ground shaking at Reston. These measurements are shown in Figure 5.13, and are aggregated with the estimated shear wave velocity at the deeper levels through bedrock.

The bidirectional (E-W and N-S) ground motions recorded at the Reston station were rotated into path-parallel and path-normal components along the source-to-recording site orientation (Mineral-Reston). These components at the ground surface

(GS) were then deconvoluted to the hard rock level at Reston using the shear wave velocity profile at the station's site (shown in figure 5.13(a)). Hard rock motions in Reston were considered to be representative of the hard rock motions at the Monument site due to their proximity and respective distances to the earthquake source. Hard rock motions at the base of the Reston profile were rotated into (Mineral-Monument site) path-parallel and path-normal components. Site response analysis was then performed using Deepsoil (Hashash et al. 2012) to propagate the rotated rock motions up to the FL at the Washington Monument site using the velocity profile at the site (shown in figure 5.13(b)). Finally, an angular transformation was used to rotate the estimated FL and GS motions into the E-W and N-S directions to be applied to the base of the FEM. Figure 5.14 shows the time history and response spectrum of the GS and FL ground motions in the E-W and N-S directions, respectively.

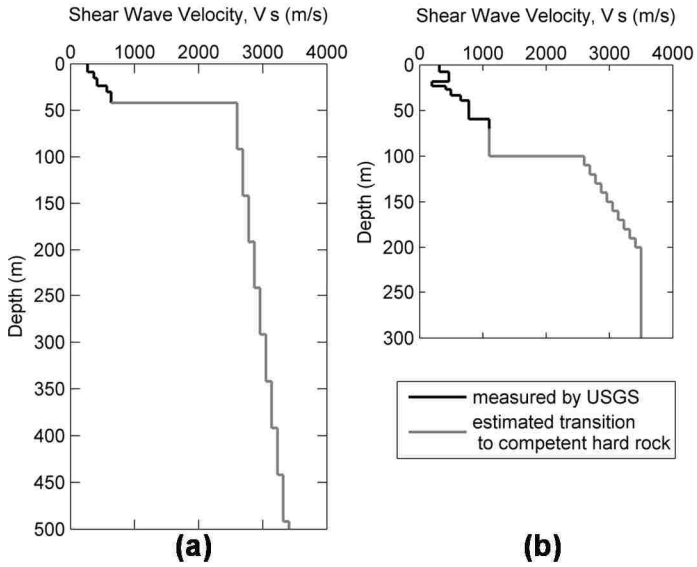

Figure 5.13. Shear wave velocity profile of the soil strata at (a) Reston (b) Washington Monument site

5.10. Behavior of the Monument during 2011 Virginia Earthquake

Time histories of the FL acceleration in the N-S and E-W directions are applied bidirectionally to the base of the calibrated FEM. Linear modal time history analysis are performed using a time step of 0.005 sec and zero initial conditions, and a 2% damping ratio for the structure is assumed which is in the range of the damping ratios obtained from the structural identification (shown in Table 5.7). This is also consistent with the identified damping ratios of masonry structures reported in the literature (De Sortis et al. 2005; Gentile and Saisi 2007). Time histories of E-W components of displacement and acceleration predicted by the calibrated FEM during the Virginia earthquake at the observation level (at 500 ft. (152.4 m)) are shown in Figure 5.15(a). This figure indicates a high range of acceleration occurs at this level, where the acceleration at the observation level are amplified by about 10 times compared to the maximum accelerations at the ground level. The distribution of maximum stresses in the vertical direction on the outer surface of the shaft is shown in figure 5.15(b). This figure shows the envelop of tensile stresses along the vertical direction of the shaft due to the combined effect of the self-weight of structure and bidirectional ground motions. The color scale in the figure indicates the magnitude of the stresses where the highest tensile stresses are shown in dark blue and white represents zero tensile stress. The tensile stresses are highly concentrated around the 350 ft. (106.7 m) level. These tensile stresses are significantly smaller than the reported tensile strength of masonry stone, but they are at the level of the tensile strength of the grout material. Table 5 summarizes the reported tensile and compressive strength of these materials (ASTM

2010 and 2011). The maximum compressive stress throughout the entire structure (-72.1 ksf (-3.45 MPa)) is also considerably smaller than the reported compressive strength of marble, granite, and grout as shown in Table 5.10. Therefore, the concentration of the maximum tensile stresses explains the cracking damage observed around these levels of the Monument shaft in terms of the mortar loss and re-cracking of the previously repaired cracks.

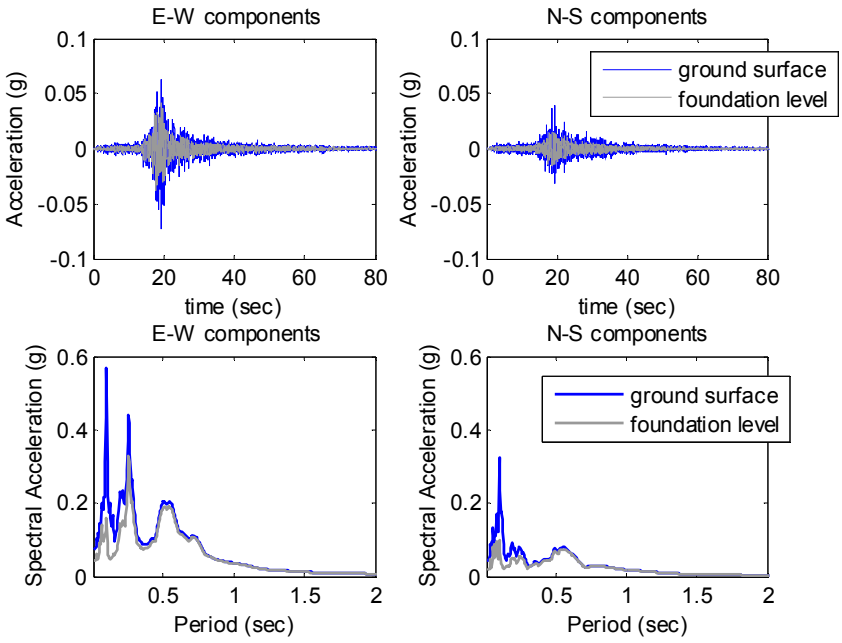

Figure 5.14. Accelerograms and response spectra (2% damping)

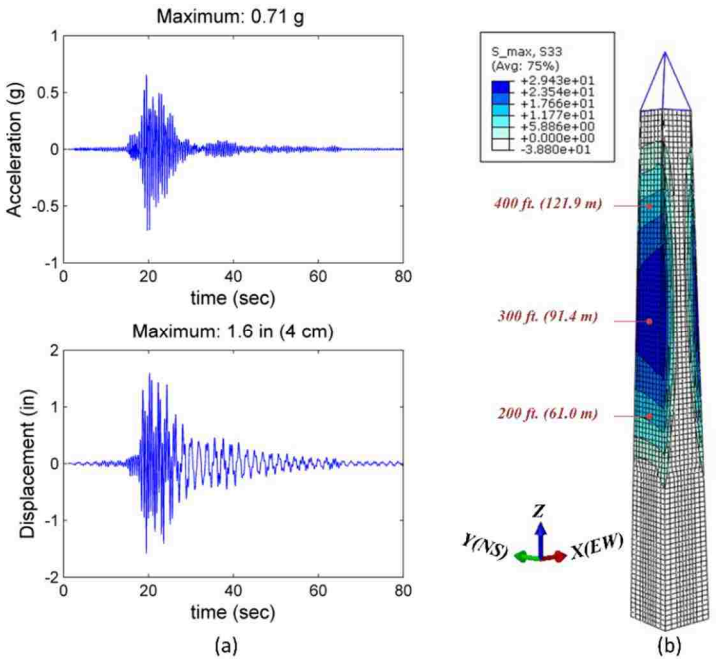

Figure 5.15. FEM predicted structural response during Virginia earthquake: (a) history of acceleration and displacement at observation level (E-W direction), (b) distribution of maximum tensile stresses (ksf) in vertical (Z) direction

Table 5.10. Compressive and tensile strength of masonry materials

Masonry material	Tensile strength		Compresive strength	
	ksf	MPa	ksf	MPa
marble	144	6.9	-1080	-51.6
granite	216	10.3	-2736	-130.8
grout	*		-288	-13.8

* tensile strength of the grout is assumed to be about 10% of its compressive strength

5.11. Fragility Study

This section presents a fragility study to investigate the possibility of damage to the Washington Monument in future earthquake scenarios. The fragility function (F_R in Eq. (5.2)) provides the probability of occurrence of a damage state conditioned on a

seismic intensity measure (SIM) (e.g., peak ground acceleration, spectral acceleration at the fundamental period of vibration, etc.):

$$F_R(SIM) = P_{LS}(SIM) = P(\theta_D \geq \theta_{LS} \mid SIM) \tag{5.2}$$

where θ_D and θ_{LS} denote the seismic demand and structural capacity, respectively, associated with the limit state LS, both in terms of a specific engineering demand parameter (EDP) (e.g., interstory drift, peak floor acceleration, etc.). This function is commonly modeled as a two-parameter lognormal cumulative distribution function expressed by Eq. (5.3) (Shinozuka et al. 2000; Ellingwood et al. 2007):

$$F_R(SIM) = \Phi\left[\frac{\ln(SIM / SIM_{LS})}{\beta_{comb}}\right] \tag{5.3}$$

In this equation, SIM_{LS} is the median structural capacity associated with the limit state LS, Φ denotes the standard normal cumulative probability function, and β_{comb} is the combined standard deviation reflecting the overall (aleatoric and epistemic) uncertainty in the fragility analysis. In effect, two sets of information are required for estimating the parameters of this lognormal fragility function: (1) probabilistic seismic demand model as a function of selected SIM, and (2) probability characteristics of the structural capacity associated with the limit state LS.

The probabilistic seismic demand model in this study is a power function (shown in Eq. (5.4)) relating the selected structural demand to the SIM. This model was previously used for the fragility analysis of other types of structures such as reinforced

concrete frames (Celik and Ellingwood 2010) and steel frames (Cornell et all 2002, Kinali and Ellingwood 2007).

$$\theta_D = a\, SIM^{\,b}\, \varepsilon \tag{5.4}$$

In logarithmic form this model can be written as

$$\ln(\theta_D) = \ln a + b \ln(SIM) + \ln(\varepsilon) \tag{5.5}$$

Constants a and b are estimated using the least squares technique and a dataset generated from a non-linear time history analysis using an ensemble of earthquakes. $\ln(\varepsilon)$ is the random error component in the regression analysis. In this model the errors are assumed to be uncorrelated and follow a zero mean Gaussian distribution (Montgomery et al. 2004). Therefore, $\ln(\theta_D | SIM)$ follows a normal distribution (Montgomery et al. 2004), where

$$\ln(\theta_D | SIM) \sim N(\ln\hat{a} + \hat{b}\ln(SIM), \sigma_{\ln(\varepsilon)}) \tag{5.6}$$

In Eq.(5.6), $\hat{a}$ and $\hat{b}$ are the least square estimates for a and b, and $\sigma_{\ln(\varepsilon)}$ is the standard deviation of the error of the regression model shown in Eq. (5.6).

In order to obtain the seismic intensity measure associated with the performance limit state, the model established in Eq. (5.4) can be used. Therefore, $\ln(\theta_{LS} | SIM_{LS})$ follows a normal distribution as shown in Eq. (5.7)

$$\ln(\theta_{LS} | SIM_{LS}) \sim N(\ln \hat{a} + \hat{b} \ln(SIM_{LS}), \beta_{LS}) \tag{5.7}$$

β_{LS} (the logarithmic standard deviation of θ_{LS}) is usually determined from an existing database (Ellingwood and Tekie 2001).

Having the probabilistic models of demand and capacity, Eq. (2) can be written as

$$F_R(SIM) = P(\theta_D \geq \theta_{LS} | SIM) = P(\ln\theta_D - \ln\theta_{LS} \geq 0 | SIM) \tag{5.8}$$

Substituting the Eqs. (5.6) and (5.7) into Eq. (5.8) reformulates the fragility function as

$$F_R(SIM) = \Phi[\frac{\hat{b}\ln(SIM) - \hat{b}\ln(SIM_{LS})}{\sqrt{\sigma_{\ln\varepsilon}^2 + \beta_{LS}^2}}] = \Phi[\frac{\ln(SIM / SIM_{LS})}{\sqrt{(\sigma_{\ln\varepsilon}^2 + \beta_{LS}^2)/\hat{b}^2}}] \tag{5.9}$$

The quantity β_M is typically included in the standard deviation of this fragility function to represent the epistemic uncertainty associated with the error in the structural modeling (Kinali and Ellingwood 2007). Therefore, the logarithmic standard deviation of the fragility function shown in Eq. (3) is written as

$$\beta_{comb} = \sqrt{(\sigma_{\ln\varepsilon}^2 + \beta_{LS}^2)/\hat{b}^2 + \beta_M^2} \tag{5.10}$$

5.11.1. Generation of hazard level compatible earthquake ensembles

As stated before, the first step in the fragility analysis is to establish a probabilistic demand model (shown in Eq. (5.4)). For this purpose, the FEM of the structure is analyzed using a suite of ground motions representing future potential ground shaking at the site of the structure. In this study, two sets of 22 bidirectional bedrock motions are utilized at the Design Basis Earthquake (DBE) and Maximum Credible Earthquake (MCE) hazard levels. These bedrock motions were originally developed by McGuire et al. (2001) as a set of 151 tri-dimensional bedrock motions to represent the CEUS ground shaking. Setting the DBE and MCE uniform hazard response spectrum (UHRS) developed by USGS at the bedrock level of the Washington Monument (Site Class A) as the target spectrum, the geometric mean of the horizontal components of these bedrock motions are uniformly scaled to match the target, and 22 sets of motions with the least overall error between the scaled spectra and the target spectrum (over periods smaller than 2 sec) are selected for the structural fragility analysis in this study (Chu et al. in preparation). A site response analysis is subsequently performed using Deepsoil (Hashash et al. 2012) to propagate the bedrock motions to the foundation level (FL) and ground surface (GS) using the shear wave velocity profile of the site (shown in figure 5.13(b)). Figure 5.16 shows the response spectra of the generated ground motions at DBE and MCE hazard levels.

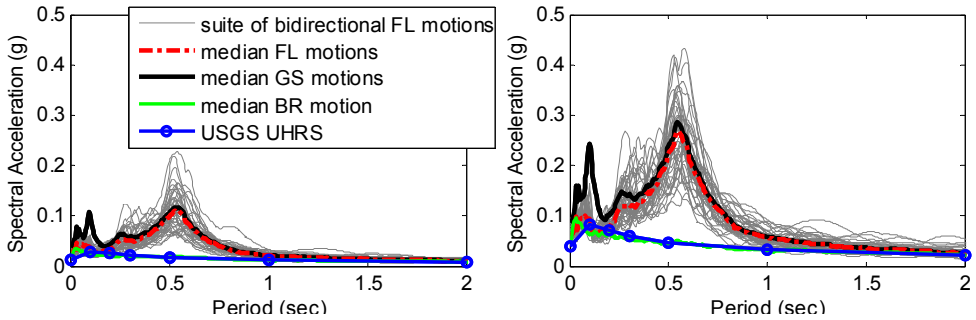

Figure 5.16. Acceleration response spectra (5% damping) (a) DBE hazard level (b) MCE hazard level

5.11.2. Description of the ABAQUS non-linear FE model

In order to study the fragility of the Monument, the updated ABAQUS FEM described above is modified to consider the fragility of the grout and previously damaged sections of the shaft tension and compressive failure during future earthquakes. Therefore, an elasto-plastic material model with the appropriate tensile and compressive strengths is introduced for the solid elements of the model of the shaft. For this material model, cracking in tension is governed by the maximum principal stress, while in compression maximum Von Mises criteria governs the maximum compressive stress. In this study, the maximum uniaxial tensile strength was set to 50% of the assumed tensile strength for the grout (see Table 5.10) to reflect the deteriorated state of the grout based on the post-earthquake assessment report (Wiss, Janney, Elstner Associates, Inc. 2011). The maximum uniaxial compression strength is set to the minimum of compressive strength of materials shown in Table 5.10. However, this limit did not govern the material behavior in any of the MCE and DBE earthquake scenarios. Non-linear time history analyses are performed for each FL ground motion pair using the Hilber-Hughes-Taylor direct integration method (α=-

0.05) with a 0.005 sec time step. Rayleigh proportional damping was used in the model based on 2% damping in the 2nd and 3rd translational modes.

5.11.3. Acceleration-based Fragility analysis

The analysis results showed that during the Virginia earthquake the acceleration at the observation level is amplified by about 17 times compared to the input acceleration at the foundation level (i.e., FL). This high amount of acceleration amplification may explain the cause of the observed damage at the upper sections of the shaft, pyramidion, and fallen debris near the observation level following this earthquake. This section concentrates on the fragility of the "acceleration-sensitive" non-structural components (e.g. mechanical systems, elevator, lighting fixtures, etc.) at the observation level.

In this study, the peak floor acceleration response at the observation level (500 ft. (152.4 m)) and average (2% damping) FL spectral acceleration of the first three translational modes in E-W and N-S direction (S_{ave}) are selected as EDP and SIM, respectively. Figure 5.17(a) shows the EDP database resulted from the non-linear time history analysis of the FEM at the DBE and MCE hazard levels, as well as the developed probabilistic demand model. This demand model along with the median capacity (θ_{LS}) is used to create fragility functions. In order to improve this estimation, an interval associated with a selected statistical confidence level can be used. Since the demand model of Eq. (5.5) is developed with the assumption that $\ln(\varepsilon)$ is normally distributed the t-distribution is used to construct a 100(1-α) percent confidence interval

(CI) for $E(\ln(\theta_D|SIM))$, where α is the level of significance in the confidence interval and shows the rejection regions under the probability distribution function associated with $\ln(\theta_D|SIM)$. Figure 5.17 (b) shows the demand model predicted with the 95% confidence. Also shown on this plot is the 95% CI associated with predicting observations outside the range of datasets used in the regression analysis.

Peak floor acceleration limits defined in HAZUS (FEMA 2012) for non-structural acceleration-sensitive components of "Pre-Code" structures are adopted here. On this basis, four limits for progressively increasing non-structural damage are defined: "Slight" damage ($\theta_{LS} = 0.2g$), "Moderate" damage ($\theta_{LS} = 0.4g$), "Extensive" damage ($\theta_{LS} = 0.8g$), and "Complete" damage ($\theta_{LS} = 1.6g$). The three contributors to the damage variability are obtained as follows: (1) record-to-record variability is accounted for by using a point estimator for $\sigma_{\ln(\varepsilon)}$ from the regression of the demand model presented in figure 5.17; (2) as HAZUS suggests, β_{LS} is set to 0.6 to consider the uncertainty in the damage state thresholds; and, (3) uncertainty associated with the capacity estimation using the updated FEM is also considered by setting β_M to 0.1. Figure 5.18(a) shows the fragility curves created for acceleration-sensitive components at the observation level of the Washington Monument based on median EDP. Figure 5.18(b) shows the fragility regions created on the basis of the confidence intervals discussed above. For the "Moderate" and "Extensive" damage states, the 95% CI associated with estimation of median EDP is used. However, for the "Slight" and "Complete" damage states, where the threshold falls outside of the

range of the dataset generated with DBE and MCE earthquake ensembles, the confidence interval for predicting observations outside the range of regression data is utilized to create the fragility regions. It is observed that with this method, more uncertainty is considered in estimating the fragility of the structure in the "Complete" damage state. Figure 5.18 indicates that for the Virginia earthquake with a 0.076 g average FL spectral acceleration at the first three translational modes of the updated FEM (spectral acceleration corresponding to first three translational modes in X(E-W) direction are 0.008g, 0.189g, and 0.168g, and spectral acceleration corresponding to first three translational modes in Y(N-S) direction are 0.003g, 0.062g, and 0.025g), there is a 85% to 98% probability of reaching the "Slight" damage state, 55% to 75% probability of reaching the "Moderate" damage state, and a low probability (less than 25%) of reaching the "Extensive" and "Complete" damage states.

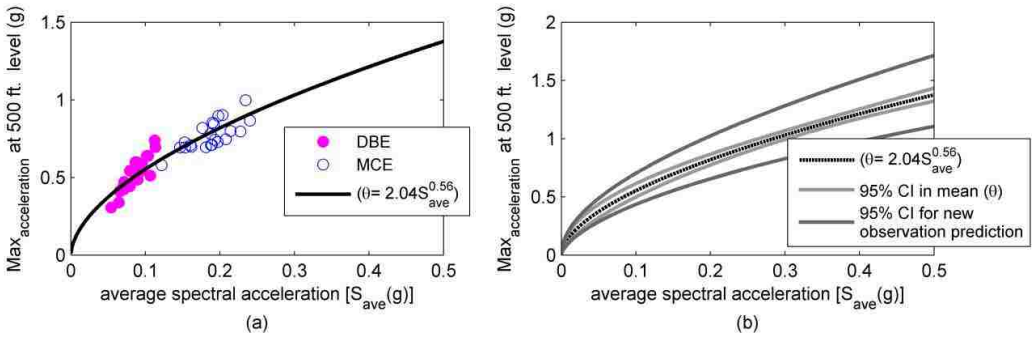

Figure 5.17. Acceleration-based demand model: (a) generated dataset and regression model; (b) 95% estimation and prediction confidence level

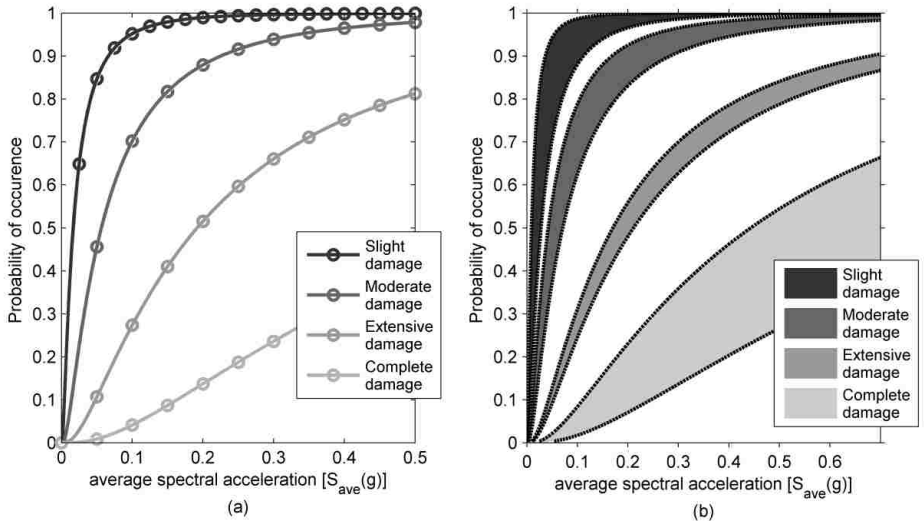

Figure 5.18. (a) Acceleration-based fragility curves; (b) acceleration-based fragility regions (CI= 95%)

5.11.4. Stress-based Fragility analysis

Since cracking under tensile stresses is one of the main damage modes of masonry structures, the fragility of the Washington Monument associated with crack initiation and propagation is also investigated. For this purpose, three limit states are defined as follows: (1) crack initiation; (2) crack propagation to more than 25% of the outer surface of the masonry shaft (representing the "Moderate" damage); and (3) crack propagation to more than 50% of the outer surface of the masonry shaft (representing the "Extensive" damage). The cracked area in each earthquake scenario is obtained by examining the area on the outer surface of the FEM to determine where a residual plastic strain exists at the end of each non-linear time history analysis. Table 5.11 presents the probability of occurrence of these limit states at the DBE and MCE hazard levels. It is observed that for a DBE level earthquake scenario, there is high

probability associated with crack initiation; however, it is unlikely that the cracking extends to a moderately large area on the outer surface of the Monument. For a MCE level event on the other hand, the probability of crack initiation as well as the extensive crack propagation is high. For the Virginia earthquake with a 0.076 g average FL spectral acceleration at the first three translational modes of the updated FEM, the probability of crack initiation is high, whereas the probability of reaching the "Moderate" and "Extensive" damage state is low. This is consistent with the observations from damage reconnaissance reports following the Virginia earthquake.

Table 5.11. Probability of occurrence of limit states associated with cracking

Hazard Level	Probability of exceedance in 50 years	Retrun period (years)	median S_{ave} (g)	Probability of occurrence of limit state		
				(1) crack initiation	(2) moderate crack	(3) extensive crack
DBE	10%	475	0.088	82%	23%	0%
MCE	2%	2475	0.190	100%	100%	59%

5.12. Summary and conclusions

This chapter explores potential causes of damage to the Washington Monument during the Virginia earthquake as well as the estimation of the probability of occurrence of similar patterns of damage to this structure during future earthquakes. For this purpose, a FEM of the Washington Monument is developed using the ABAQUS computer program. The focus of this study is to investigate the cause of damage to the shaft of the Monument during the Virginia earthquake as well as the possibility of damage to the shaft in the future. While the effect of pyramidion section on overall dynamic behavior of the Monument was included in the FEM, this section was not modeled in detail due to lack of available information for modeling as well as

interior access for sensor deployment and structural identification of such a complicated system.

The modeling primarily focuses on the sub- and super-structure of the outer masonry shaft of the Monument. In the sub-structure, the total mass of the foundation and soil on top of it is lumped at its center of mass and a group of uncoupled springs is used at the base of the foundation to model the compliance of the surrounding soil. In order to minimize the uncertainty in the modeling procedure, ambient vibration measurements are used to identify the dynamic characteristics of the structure. The FEM is then calibrated with reference to the extracted natural periods of the structure. Due to the lack of recorded ground motions in the immediate Washington, DC area, ground motions that occurred during the Virginia earthquake at the site of the Washington Monument are estimated by applying angular transformations and site response analysis using shear wave velocity profiles of soil layers measured by USGS to ground surface accelerations recorded in Reston, VA.

A fragility study is also performed in order to estimate the probability of occurrence of similar types of damage in future earthquakes. Two site-compatible suites of ground motions at the DBE and MCE hazard levels are generated. A non-linear FEM is developed to consider the brittle behavior of the grout and sealant material in tension. Probabilistic demand and capacity models are established, and fragility intervals associated with a 95% confidence level are developed for four stages of damage in acceleration-sensitive non-structural components. Moreover, the

occurrence probability of three damage states associated with initiation and extent of cracking of grout and repaired masonry materials are established.

The principal findings of this research are as follows:

1. This study highlights the importance of structural monitoring in providing valuable information about the dynamic characteristics of existing structures to be used as a basis for reduction of modeling uncertainty.

2. The cross validation of the model calibration techniques reveals that while sensitivity-based and surrogate-based model updating methods yield the same results, surrogate-based model calibration requires less computational effort for global search in the domain of model parameters.

3. Time history analysis of the calibrated FEM of the Washington Monument using the estimated ground shaking during the 2011 Virginia earthquake, show high acceleration at the top of the Monument as well as a concentration of tensile stress at the upper levels of the masonry shaft. These observations correlate with the damage observed in the pyramidion section and cracking of repaired sections and loss of mortar in the upper levels of the shaft.

4. The fragility analyses performed indicate the probability of structural and non-structural damage to this structure in future earthquake scenarios. Fragility curves are beneficial in establishing the probability of several states of acceleration-based damage at the observation level based on average spectral acceleration of a selected earthquake scenario.

5. The damage states associated with cracking of the grout material also shows a high probability associated with initiation and propagation of such cracks on the outer surface of the masonry shaft of the Monument during a future earthquake.

6. The study highlights the critical need for improved recognition and greater awareness of the seismic vulnerability of constructed facilities and lifelines in the Central and Eastern United States.

Chapter 6

Structural damage detection and localization using multivariate regression models and two-sample control statistics

This chapter presents model-free damage identification and localization methods based on two-sample control statistics. The proposed methodology consists of two steps: (1) damage feature extraction, and (2) decision making through change point analysis. Performance of combinations of several damage features, regression models, and control statistics on a scaled two-bay steel frame instrumented with a dense sensor array is compared. The acceleration response of the frame recorded from two different physical states are measured and control charts are used to find the significance of change between the two. The first state is a baseline (here "healthy") state of the structure, and the second is an unknown state. In effect, two sets of data are created that would be taken from a structure pre- and post- a damaging event (or a regular maintenance check). Damage features are created based on linear regression parameters, and are utilized in the control charts to make the distinction, if any, between an undamaged and an unknown state of the structure. The following sections describe the damage sensitive features and change point statistics used in this research.

6.1. *Change point analysis using Normalized Likelihood Ratio test*

The Normalized Likelihood Ratio test (NLRT) can detect a shift in the mean and/or variance of a data set. It assumes that there are *m* independent observations that are normally distributed with mean μ and standard deviation σ. If a process is in-control, at any partition of the data, the two sets would have similar means and variances. However, if there was a change in the process, the means and variances of the two subgroups would vary substantially from one another.

As explained in Sullivan and Woodall (1996), the log of the likelihood function for the first m_1 observations can be written as

$$l = -\frac{m_1}{2} log[2\pi\sigma^2] - \frac{m_1\widehat{\sigma_1}^2}{2\sigma^2} - \frac{m_1(\bar{x}_1 - \mu)^2}{2\sigma^2} \quad (6.1)$$

Here, $\bar{x}_1$ and $\widehat{\sigma_1}^2$, represent the mean and variance of the first m_1 observations, while μ and σ^2 represent the population mean and variance. This function can be maximized to generate l_1 presented below.

$$l_1 = -\frac{m_1}{2} log[2\pi] - \frac{m_1}{2} log\left[\widehat{\sigma_1}^2\right] - \frac{m_1}{2} \quad (6.2)$$

This procedure can be repeated for the remaining m_2 $(= m - m_1)$ observations to find the maximum value of the likelihood function, l_2. In this way of partitioning the process into m_1 and m_2, there is an assumption that there is a change in the data at point m_1+1. However, if this were not the case and the process was in-control for all *m* observations, the likelihood function would be maximized using $\bar{x}$ and $\widehat{\sigma^2}$, the mean

and variance of all m observations. This would generate l_o, the maximum of the likelihood function for an assumed in-control process. If l_a, the sum of l_1 and l_2, is much larger than l_o, the process is deemed to be out of control. For this reason, the likelihood ratio test detects the significance of the difference between the two. It is defined as $lrt[m_1, m_2] = -2(l_o - l_a)$ and has an asymptotic chi-squared distribution (χ^2) with two degrees of freedom (Sullivan and Woodall 1996).

This statistics is normalized to create the NLRT with a threshold value of unity. In normalizing the statistic in this damage detection scheme, any value of the likelihood ratio for a damage feature that is above one represents an out of control feature. This can then be correlated to a location on a structure if the damage feature originated from data taken from a localized sensor network. In order to normalize the statistics, it is divided by its expected value (E), based on the dimensionality of the observations, p, and an upper control limit (UCL) based on a desired overall in-control false alarm probability, ω. As explained in Sullivan and Woodall (1996), the in-control expected value is not the same for all values of m_1. If m_1 and m_2 are small, the expected value is larger than when both are the same. Therefore, when the model order is 1, the expected value can be approximated by simulation or

$$E = 2\left[\frac{m_1 + m_2 - 2}{(m_1 - 1)(m_2 - 1)} + 1\right] \tag{6.3}$$

The test statistics is also normalized using an upper control limit which is usually set to give a specified in-control average run length. Based on m and p, the upper

control limit can be approximated. Its value has been tabulated in Sullivan and Woodall (1996) using Eq. (6.4):

$$UCL = \frac{1}{1.7} F^{-1}[(1-\omega)^{\frac{1}{k^*}}] \tag{6.4}$$

Here $k^* = -4.76 + 3.18Ln(m)$. F denotes the cumulative distribution function of a χ^2 distribution with two degrees of freedom. In this implementation, the vector of damage features is successively tested using NLRT (starting from $m_1=2$, to avoid numerical instability, through $m_1=m-2$) to detect the timing and location of the potential structural damage.

6.2. Change point analysis using Student's t-test

The other change control threshold that is utilized in this dissertation bases on the Student's t-test. The two-sample t-test is a common procedure for testing the differences between the means of two samples (Montgomery and Loftis 1987). There are three assumptions that this Student's t-test follows: (1) samples come from a parent population that is normally distributed, (2) the two sample groups are from populations with equal variances, and (3) sample observations are independent. The statistics of this test has $N-2$ degrees of freedom (N being the combined length of the two sample vectors) and is given by

$$t = \frac{\bar{X}_1 - \bar{X}_2}{S_p\sqrt{\frac{1}{n_1}+\frac{1}{n_2}}} \tag{6.5}$$

where the variables $\bar{X}_1$and $\bar{X}_2$ are the means, n_1 and n_2 are the size of the two samples, and S_p represents their pooled standard deviation equal to

$$S_p{}^2 = \frac{(n_1 - 1){S_1}^2 + (n_2 - 1){S_2}^2}{(n_1 + n_2 - 2)} \tag{6.6}$$

S_1 and S_2 are the sample standard deviations.

This method, used for cases in which the variance is assumed to be unchanged, can be used with linear regression parameters. This is because it represents the realistic condition when a property of the structure is changed due to damage if the change does not affect the estimation uncertainty of the damage feature. In this chapter this two-sample t-test is applied sequentially through the vector of damage features to identify and localize the structural damage.

Upper and lower control limits (UCL and LCL) for this test are then calculated using the Student's t inverse cumulative distribution function at a certain confidence level $(1 - \omega)\%$ and $N - 2$ degrees of freedom ($N = n_1 + n_2$) based on Eq. (6.7).

$$UCL = t_{\left(1-\frac{\omega}{2}\right),N-2}$$
$$LCL = t_{\frac{\omega}{2},N-2} \tag{6.7}$$

6.3. Localized Damage Detection Method: Mathematical Models

The damage features studied in this dissertation come from the linear regression coefficients produced by an algorithm called Influenced-based Damage Detection

Algorithm (IDDA) developed by Dorvash et al. (2013a and 2013b). These damage features are shown to be viable ways of detecting damage in a structure because they are sensitive to the changing properties of a structure. The IDDA algorithm correlates the response (measured acceleration signals in Dorvash et al. (2013a) and measured strain signals in Dorvash (2013b)) of a structure at various locations by creating influence coefficients from a linear regression model based on output of a dense sensor network. When damage occurs, the relationship between responses changes, which will be reflected in the influence coefficients and indicate the existence of damage. The location can then be pinpointed by correlating such data driven damage features to the location of the sensors.

6.3.1. Single Variate Regression Model

The simplest linear mapping model is the Single Variate Regression (SVR) model. It relates the acceleration response of one location to another location at the current time step. This version of the model can be represented using Eq. (6.8)

$$y_j = \alpha y_i + \beta + \epsilon \tag{6.8}$$

which correlates the response at node j to current response at node i through α with intercept β and error ϵ. Since the effects of previous time steps are removed from this equation, the intercept (β) is added into Eq. 6.8 to account for the initial conditions. The influence coefficient α is then used to extract damage feature from the linear regression model in this study. The derivation and validation of this simplified mathematical model can be found in Dorvash et al. (2013a) on a scaled beam-column

connection. Since this damage feature has already been proven to detect and localize damage in small- and large-scale structural models (Dorvash et al., 2013a and 2013b), it is used as a basis for comparison and derivation of the proceeding damage features discussed in the following sections.

6.3.2. Auto-Regressive Models

The SVR model can be expanded to include more information about the system from past and present time steps of the structural response. In effect, this Auto Regressive with Exogenous term (ARX) model can be written as

$$y_j(n) + \sum_{p=1}^{P} \alpha_{jp} y_j(n-p) = \sum_{q=0}^{Q} \alpha_{iq} y_i(n-q) + \varepsilon(n) \tag{6.9}$$

where y_j and y_i are outputs at locations j and i respectively, α_{jp}'s and α_{iq}'s are the ARX coefficients, $\varepsilon(n)$ represents the residuals, n is the time index, and P and Q are orders of the autoregressive and exogenous parts of the ARX model, respectively. Derivation and validation of this formulation can be found in Yao et al. (2012).

This ARX model can be simplified to just include one location on a structure. This regression may produce more localized results if only one location is involved in the model. Acceleration response at the same location in time can be established using an Auto Regressive (AR) model as

$$y_j(n) = \sum_{p=1}^{P} \alpha_p y_j(n-p) + \varepsilon(n) \tag{6.10}$$

In this formulation, y_j is the output at location j, α_p's are AR coefficients, $\varepsilon(n)$ represents the residuals, n is the time index, and P is the order of the AR model. In this study, the regression coefficients (α_p's , α_{jp}'s, and α_{iq}'s) are used to generate damage sensitive features from the AR and ARX linear regression models to be tested in the change point analyses.

The order of the AR and ARX models must be determined before the influence coefficients can effectively be used in damage control charts. The accuracy of the two regression models depends on the selected model orders based on the data from the localized sensor networks. While higher model orders, in general, deliver more details of the system and reduce the estimation bias, it is always desired to keep the order at the minimum level to avoid over-parameterization. One way to establish the model order is to minimize the Akaike's Information Criterion (AIC) which is used in Friedlander and Porat (1984) and Figueiredo et al. (2011) as,

$$AIC(p) = (L - p) \times Ln(SE) + 2p \tag{6.11}$$

In Eq. (6.11), p is the number of parameters in the AR model and SE is the sum of the squared regression residuals divided by $L - p$ (L being the total number of data samples). Once the model order number is found and the AR and ARX coefficients are regressed, their coefficients are condensed to generate a univariate control statistics.

6.3.3. Collinear Regression Model

The SVR model can also be modified to correlate three locations on a structure without over parameterizing the system. This model is called the Collinear Regression

(CR) model. There are many different types of regressors that can be used in CR models. For this implementation, y_i in Eq. 8 is changed to the average of two outputs. In effect, the mathematical model would be calculated as

$$y_k = \alpha_{ijk}\frac{(y_i + y_j)}{2} + \beta + \epsilon \tag{6.12}$$

Here, an additional location's acceleration output, y_k, can be included to create the new coefficient α_{ijk} . The effectiveness of CR influence coefficient is analyzed and compared to the AR, ARX, and SVR model parameters presented above in the structural damage detection based on change point analysis.

6.4. Localized Damage Detection Method: Damage Features

There are two types of features that are used to test the null hypothesis that the mean of the two observation samples from different states of the system are equal. The first of these is a scalar function of the regression coefficients – referred to as *Alpha-based Coefficients* in this chapter – obtained from the regression models discussed above. In cases of the SVR and CR models, the output of this function is the influence coefficients themselves, whereas for the AR and ARX models, the Mahalanobis distance is utilized to find a scalar representation of the multivariate regression coefficients corresponding to a condition of interest and those corresponding to a reference condition (Mosavi et al., 2012). The Mahalanobis distance $\boldsymbol{D_m(x)}$ can be computed by using Eq. (6.13)

$$D_m(x) = \sqrt{(x-\mu)^T S^{-1}(x-\mu)} \tag{6.13}$$

where x is the matrix of the reference regression coefficients with mean μ, and S is its covariance matrix. Once the distances are calculated, these scalar representations of the influence coefficients are used in the change point analysis.

The second damage feature used in this study is called the *Angle Coefficient*. This coefficient measures the angle between regressed lines from two different states of the system. In other words, for damage detection methods, instead of measuring the difference in slope between a healthy state line and an unknown state line of a structure, the angle between the two lines can be compared to detect change as well. In effect, the *Angle Coefficient* can be written as

$$\Gamma = cos^{-1}\left|\frac{v*v'}{\|v\|\|v'\|}\right| = cos^{-1}\left|\frac{\alpha\alpha'+1}{\sqrt{\alpha^2+1}\sqrt{\alpha'^2+1}}\right| \tag{6.14}$$

Here v and v' correspond to a vector $[-1, \alpha]^T$ for an undamaged state and a vector $[-1, \alpha']^T$ for an unknown state, respectively. In this formulation, α and α' are the respective influence coefficients from SVR or CR models. For ARX and AR regression models (with model order p), $v = [-1, \alpha_1, \alpha_2 \ldots \alpha_{2p+1}]^T$ and $v = [-1, \alpha_1, \alpha_2 \ldots \alpha_p]^T$, respectively.

These two sets of coefficients, *Alpha-based Coefficients* and *Angle Coefficients*, are extracted from the acceleration signals measured from a baseline and an unknown state. They are then tested for a change in their mean using the NLRT or t-test method discussed in Section 6.1.

6.5. Test Setup

A two-bay steel tube frame testbed was constructed at the laboratory of Advanced Technology for Large Structural Systems (ATLSS) at Lehigh University. In this chapter, this specimen is used to analyze the effectiveness of the damage features discussed above. This frame was built as a testbed for damage detection, mainly to represent typical building frames or bridge girders. It has nine interchangeable sections, 0.2 m in length, that can be changed throughout the frame in order to simulate damage. These interchangeable sections have different cross sectional properties than the healthy state (shown in Table 6.1) which correspond to 20% reduction in member stiffness. In order to simulate a realistic damage scenario, the length of these switchable members was designed so that a negligible change would occur in the global behavior of the frame pre- and post- damage. Figure 6.1 shows the experimental setup used in this study.

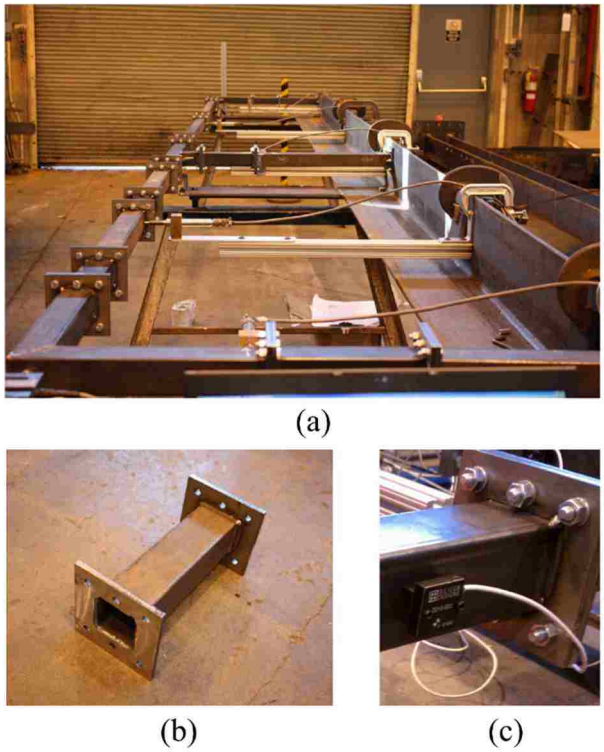

Figure 6.1. Experimental setup: (a) scaled frame (b) switch-out member (c) wired accelerometer

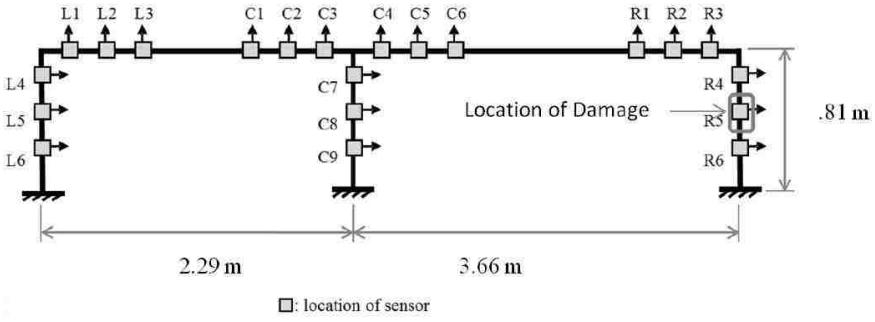

Figure 6.2. Sketch of the specimen and the location of the introduced damage

In order to collect data, the specimen was instrumented with 21 wired accelerometers, labeled in figure 6.2 with L, C, or R on left, center, and right portions

of the frame. During testing, there were a total of 40 runs of data collected. For each run, the sampling rate was 500 Hz and 1000 samples were recorded so that each test lasted a total of 2 seconds. The first 20 runs were taken when the frame was in an undamaged state, where the first 10 tests of this group serve as a known healthy baseline for comparison throughout this research. The Mahalanobis distance between these first 10 healthy runs and the next 10 healthy runs creates a baseline distance for comparison. It was at this point (run 21) that damage was simulated for the second half of the experiment. For this study, the damage case consists of replacing a healthy section with one of less stiffness at the location of sensor R5, which corresponds to less than a 1% change in the lateral stiffness as well as the first three natural frequencies of the frame. After this section is exchanged, an additional 20 tests were taken. These tests will serve as the unknown state of the structure after a damaging event by comparing the Mahalanobis distance between these 20 'damaged' runs and the baseline distance from the healthy start runs. The results, shown in Section 6, should detect the timing of the damage after the 20^{th} test and localize it to the right column of the frame.

Table 6.1. Geometry of baseline and interchangeable sections

Feature	*Baseline Sections*	*Interchangeable 'Damage' sections*
Outer Dimension of Hollow Cross Section	0.05 m (1.97 in)	0.05 m (1.97 in)
Tube Thickness	2.16 mm (0.085 in)	1.65 mm (0.065 in)
Cross Sectional Area	410.57 mm^2 (0.64 in^2)	324.57 mm^2 (0.5 in^2)
Moment of Inertia	162526 mm^4 (0.39 in^4)	130811 mm^4 (0.31 in^4)

There are two sets of data collected, which represent measurements that would be taken pre- and post- a damaging event or regular maintenance of a structure. Therefore, it is possible to assume that the structure behaves linearly during data collections. Additionally, Dorvash et al. (2010) show that the type of excitation used with IDDA does not affect the detection of damage. In order to dynamically excite the frame, impact loading is chosen as the excitation method for this implementation. This excitation is similar to ambient vibration in not imposing any specified excitation frequency to the frame. The impact amplitude was limited to ensure that the linear behavior assumption for the experimental frame holds. Therefore, the acceleration response of frame is recorded while the frame is struck with a hammer on the right column and the frame freely vibrates on its own. The data from this experiment was previously used in Nigro et al. (2014) to investigate the performance of IDDA damage features using a change point framework, where statistics such as univariate Cumulative Sum (CUSUM), Exponentially Weighted Moving Average (EWMA), Mean Square Error (MSE), Modified MSE, Mahalanobis distances, and Fisher

Criterion are used. As stated, in this chapter two-sample change point statistics are implemented for different combinations of damage features and regression models.

6.6. Results

As shown in figure 6.2, the damage case in question for this study includes damage at a section on the right side column; therefore, the results should detect damage at or near this location. Three sensor clusters on the left, center, and right portions of the frame are used for damage detection. It should be noted that the data measured with sensors L1, C3, C5, and C9 were excluded from the damage detection process, as the preliminary inspection of the measured signals revealed faulty behavior of these sensors. Considering there are five or six sensors in each sensor group, there are many different combinations of sensors that can be paired in the different linear regression models. Therefore, only sensors within the same cluster will be paired with one another. In effect, for a sensor cluster consisting of six sensors, in cases where two sensor nodes are paired with one another, 30 pairs can be made without pairing a sensor with itself. This occurs in SVR and ARX linear models. However, based on the CR model, 120 different combinations can be made. This section presents the results of the damage detection techniques described in the previous sections using the acceleration data collected from the scaled steel frame.

6.6.1. Single variate regression results

The coefficients made using SVR model are readily used in the NLRT and t-test. Since the *Angle Coefficients* are found in reference to the first baseline run of the

experiment, a possible damage point should be detected when both damage features are split into two groups of 20 tests. Figure 6.3 shows the Likelihood Ratio (LR) and absolute t-statistics of the *Alpha-based* and *Angle Coefficients* in this case. All these plots show peaks on the split at run number 20 which implies the possible timing of the damage. These peaks correspond to the maximum test statistics; since the t- or LR-test statistics are sequentially created for every two partitions of the observations as a means to signify the difference between two partitions, these statistics are maximized when all the observations in each partition belong to one state (healthy or damaged) of the system. For *Alpha-based* and *Angle Coefficients* extracted from SVR models, this corresponds to splitting observations at run number 20.

The change detection threshold is also plotted for both tests in these plots. It is seen that when run number at the split is 20, the extracted damage features from left and right side of the frame cross the change threshold, and this identifies the occurrence of damage at the 21st run of the experiment. The damage features extracted from the left and right sensor clusters at this split are plotted in figure 6.4. As the entire frame's response is changing with the switch of the damaged section, it is expected that the damage features on the left side also cross the change threshold. However, the detected change at the right side of the frame is more pronounced than the left side. This implies that with a sensor located at right or left side of the frame, the occurrence of the damage is most likely successfully identified; however, localizing the damage to a specific location on the frame requires denser instrumentation.

The average of the test statistics associated with each sensor location that indicates a statistically significant change in the extracted damage features are used in order to localize the identified damage. This quantity correlates the severity of the change in the damage features with the sensor locations on the structure. Figure 6.5 shows these localized damage indicators extracted from the SVR models. This figure shows that based on the maximum averaged test statistics, damage is localized to R6. With this measure, the actual location of the damage R5, has the second largest damage indicator. Therefore, it can be concluded that this change detection method successfully localizes the damage to its true locale.

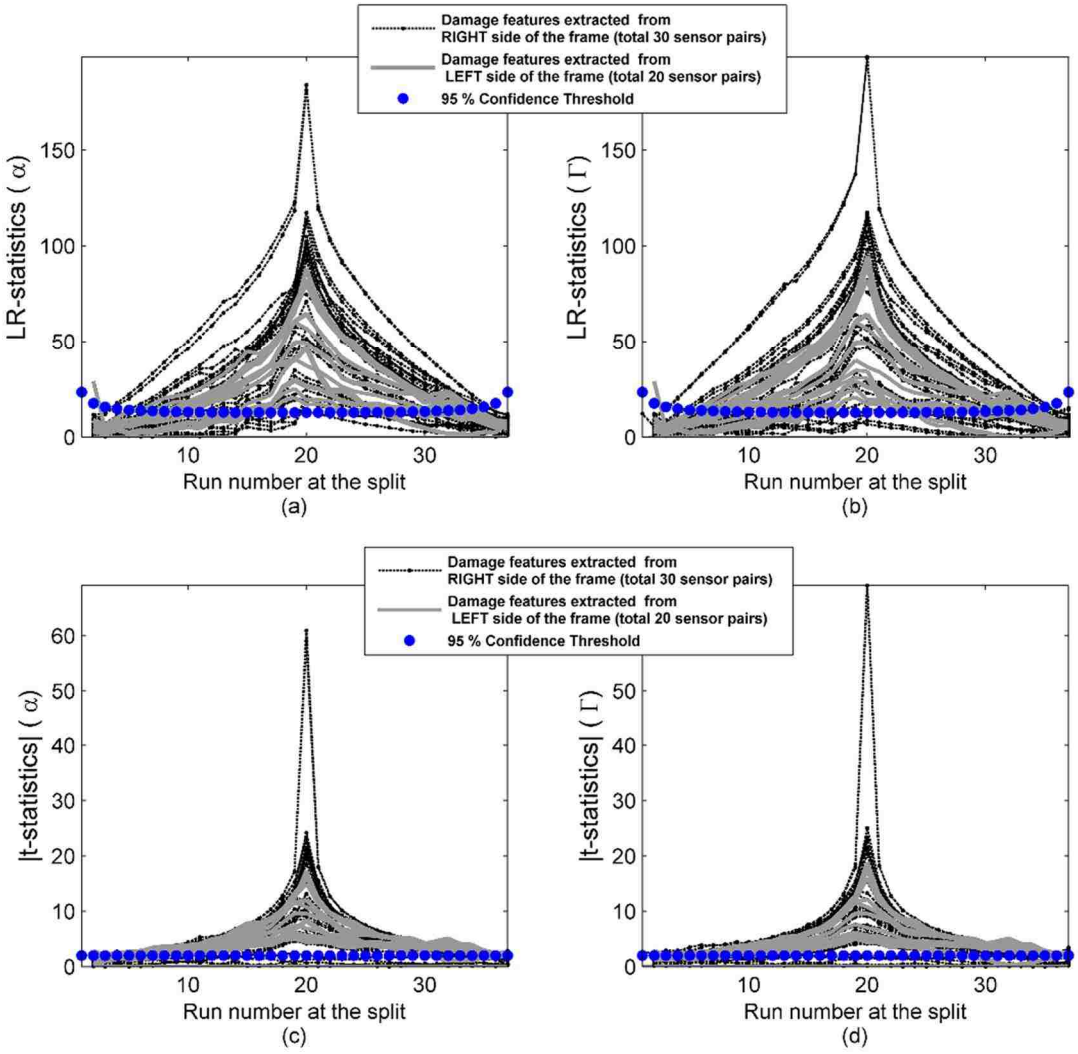

Figure 6.3. Test statistics of the damage features extracted from the SVR models: (a) LR-statistics, Alpha-based Coefficients; (b) LR-statistics, Angle Coefficients; (c) absolute t-statistics, Alpha-based Coefficients; (d) absolute t-statistics, Angle Coefficients

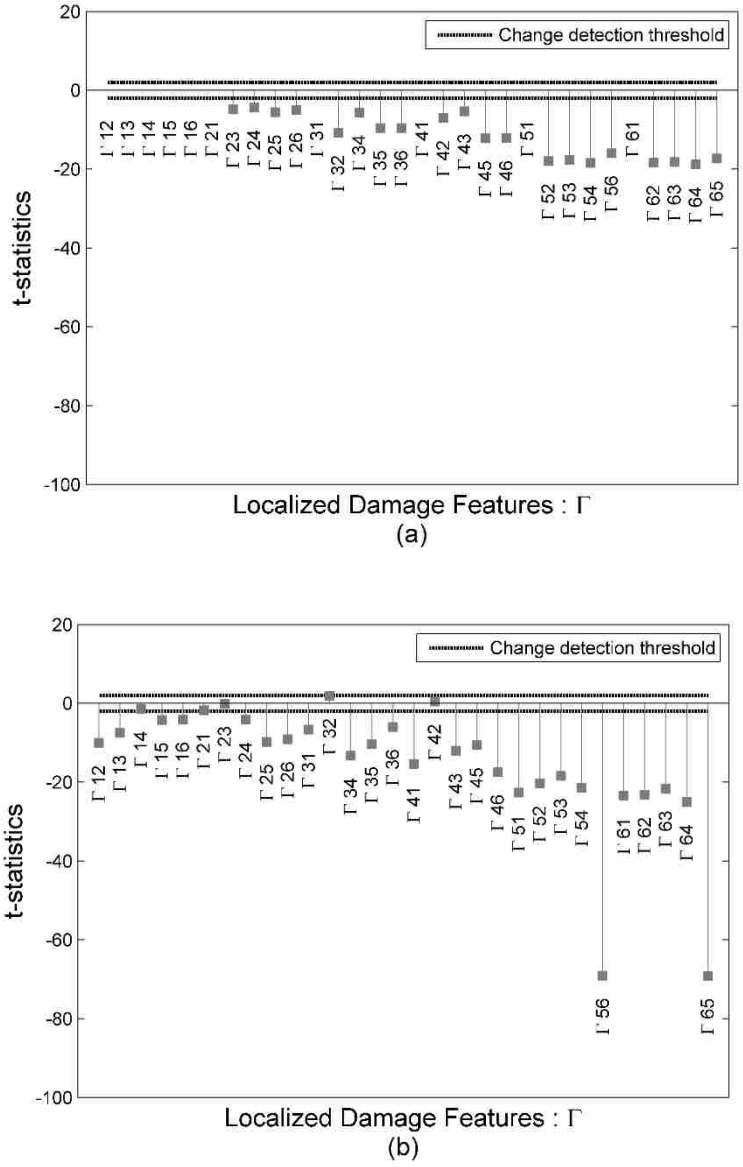

Figure 6.4. Test statistics of the damage features extracted from the SVR models (split at the 20th run): (a) Alpha-based Coefficients at the LEFT side; (b) Alpha-based Coefficients at the RIGHT side

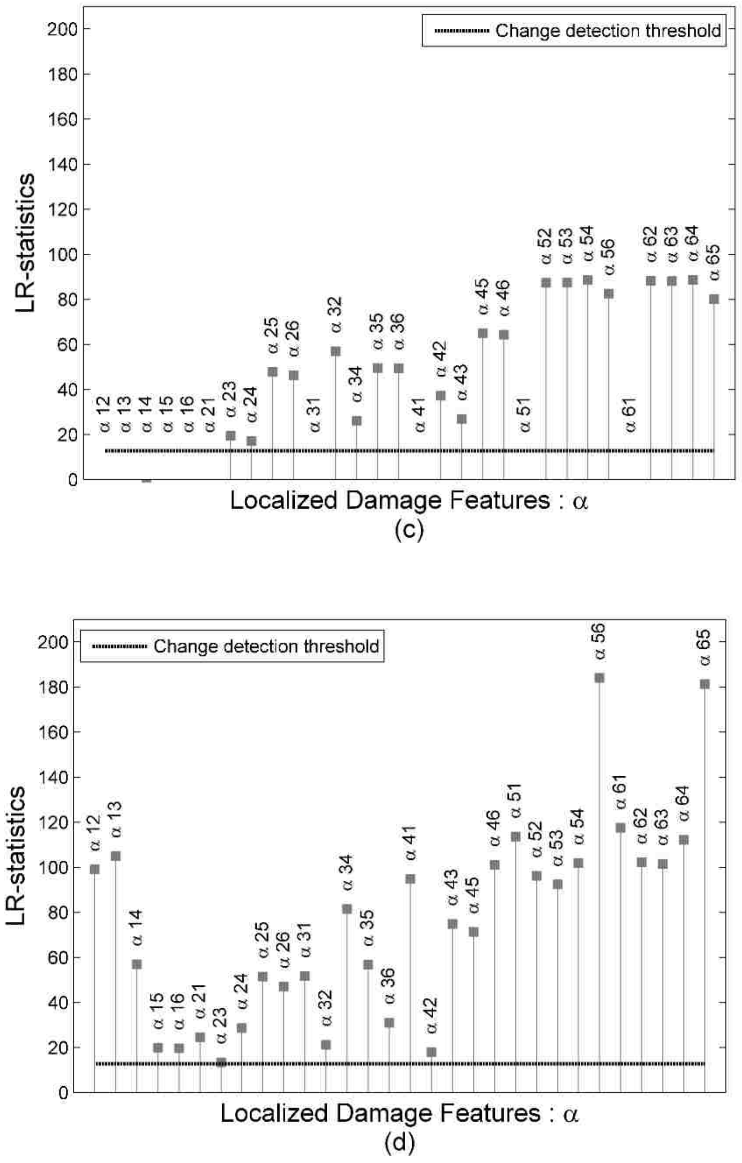

Figure 6.4. Test statistics of the damage features extracted from the SVR models (split at the 20th run): (c) Angle Coefficients at the LEFT side; (d) Angle Coefficients at the RIGHT side

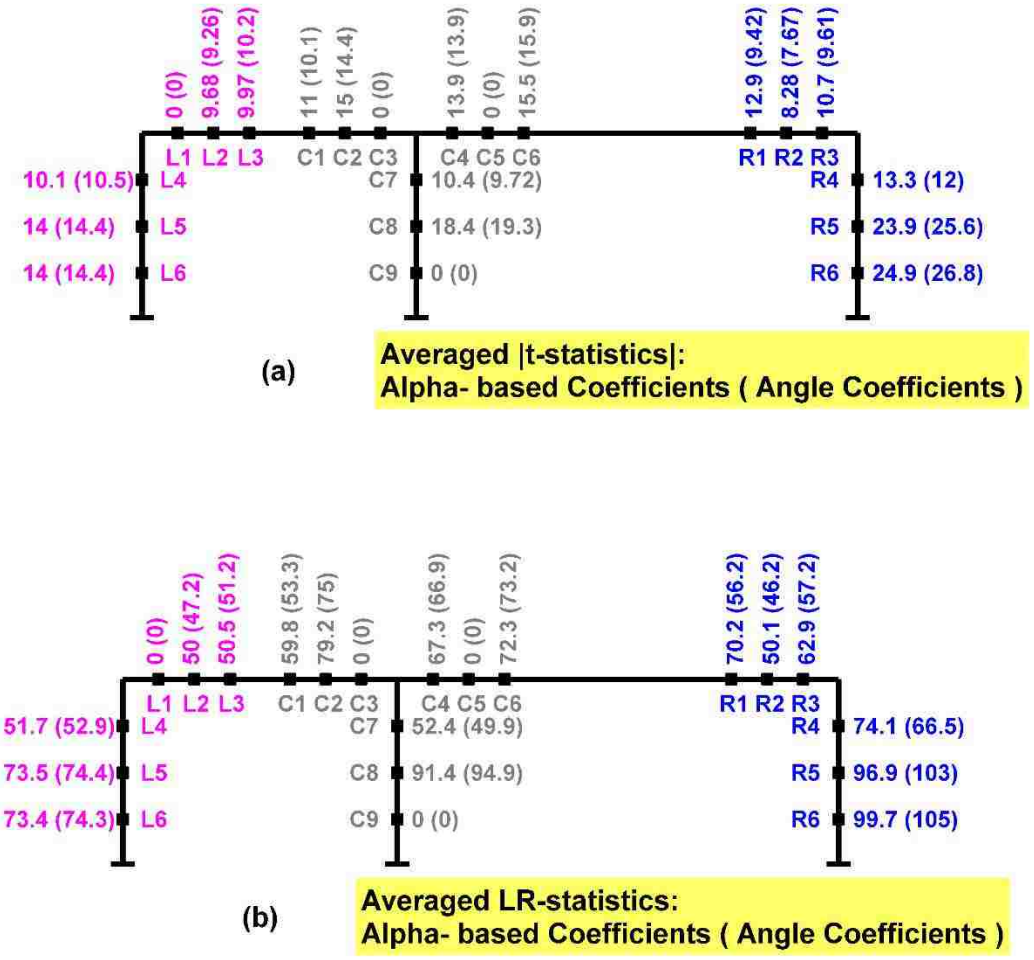

Figure 6.5. Localized damage indicators using SVR models: (a) Average absolute t-statistics, (b) Averaged LR-statistics

6.6.2. ARX model results

The regression coefficients of ARX models, with model order 4, are first condensed into a scalar damage feature using Mahalanobis distance which is then used in the developed damage detection methods. The model order selection in this implementation is based on the AIC criteria described in Section 6.2.2 along with the

fact that the first 10 test runs are assumed to be conducted on a known healthy structural configuration, and thus are used as reference to calculate the Mahalanobis distances. Therefore, Mahalanobis distances are calculated between coefficients from the first 10 healthy state runs and the last 10 healthy state runs. This step creates a baseline distance. Then, the first 10 healthy runs and the 20 damaged runs are used to create a distance to compare to the reference. The distances calculated in the latter coefficients should be bigger than the baseline condition at areas of damage. In effect, a possible significant change is expected to happen when the run number at the split is 10. As the proposed *Angle Coefficients* are scalar quantities, no preprocessing is required prior to the change point analysis, and therefore the timing of possible damage is expected to be detected at the split with run number 20. Figure 6.6 shows the test statistics of the features extracted from ARX models. This figure shows that the damage features from the ARX model do identify the correct timing of damage.

The damage features at the identified change time are plotted in Figures 6.7 and 6.8. These figures show that, similar to the SVR results, at time of the damage (11^{th} run in case of *Alpha-based coefficients*, and 21^{st} run based on *Angle Coefficients*), several coefficients on the left and right side of the girder cross the change threshold. The test statistics are then analyzed for their effectiveness in localizing the damage. The results are displayed in Figure 6.9. This figure shows that the averaged test statistics of the Mahalanobis distance locate the damage at R4, while such damage indicators based on *Angle Coefficients* localize the damage to its true location at R5.

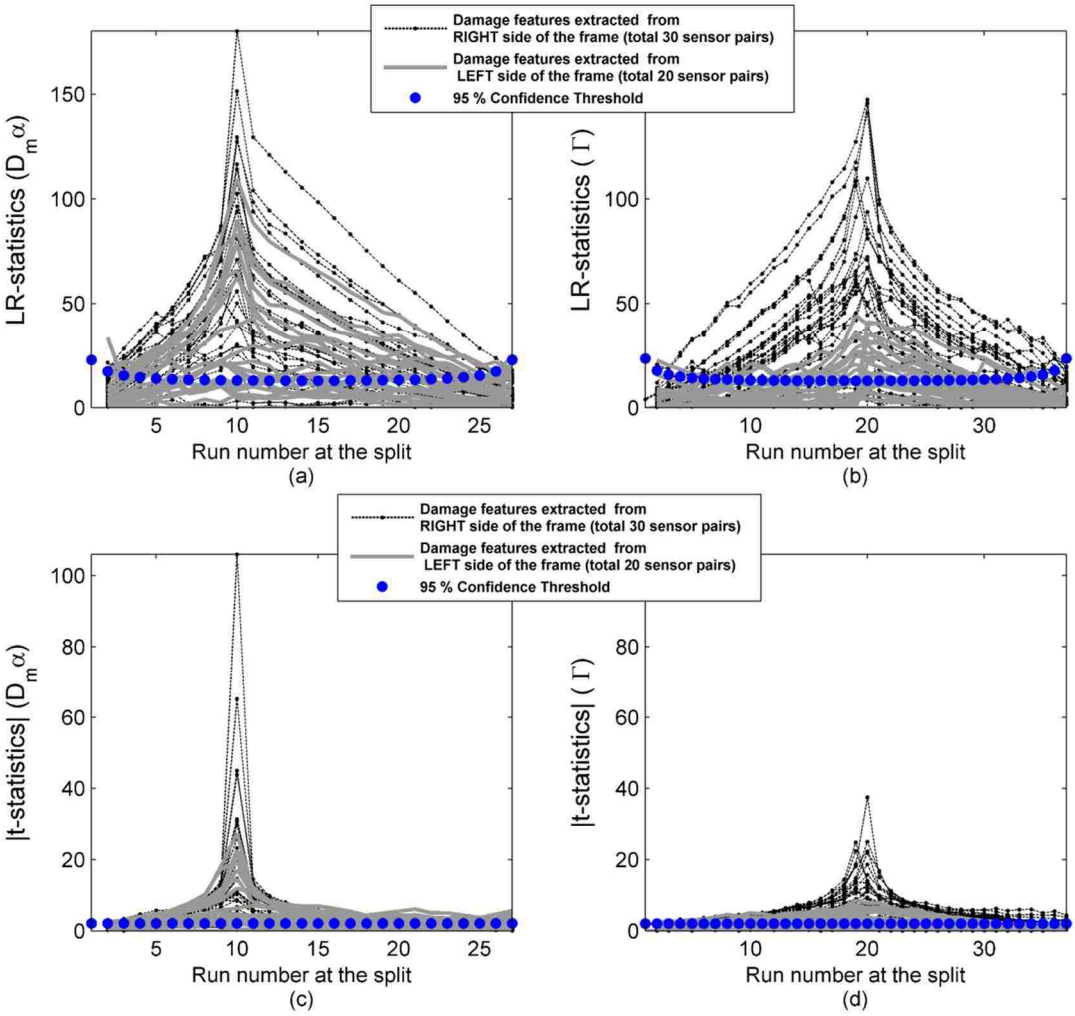

Figure 6.6. Test statistics of the damage features extracted from the ARX models: (a) LR-statistics, Alpha-based Coefficients; (b) LR-statistics, Angle Coefficients; (c) absolute t-statistics, Alpha-based Coefficients; (d) absolute t-statistics, Angle Coefficients

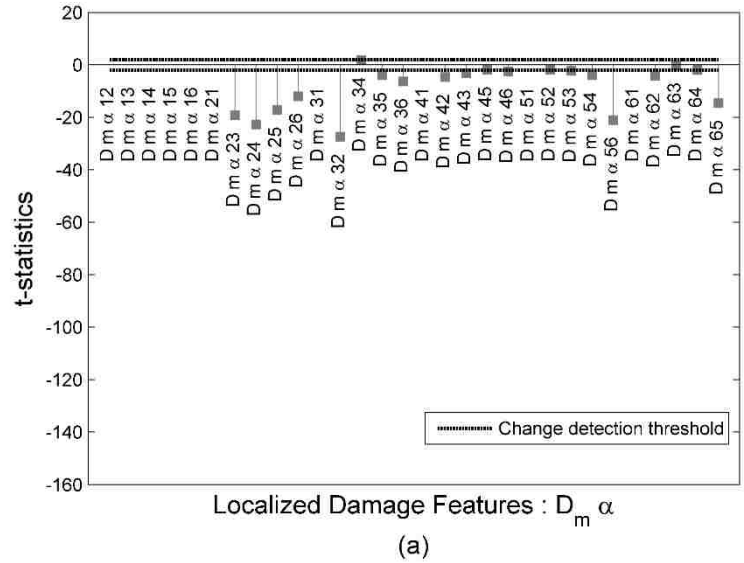

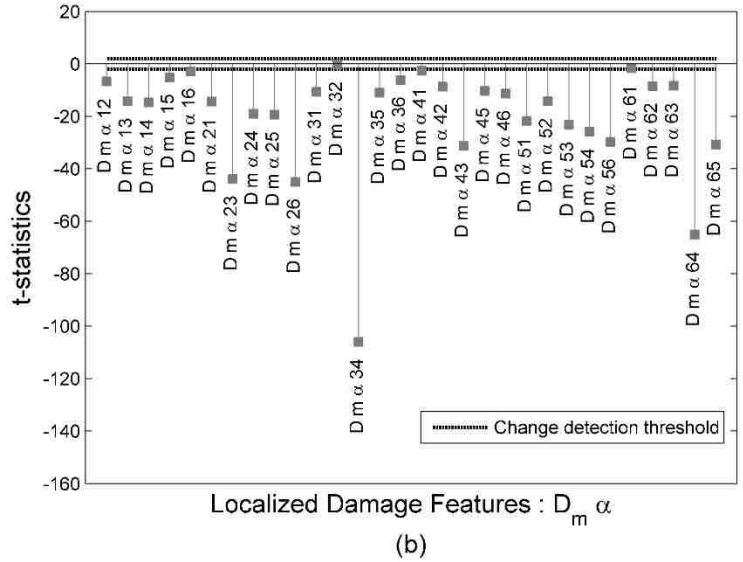

Figure 6.7. The t-statistics of the Alpha-based Coefficients extracted from the ARX models (split at 10th run): (a) at the LEFT side and (b) at the RIGHT side

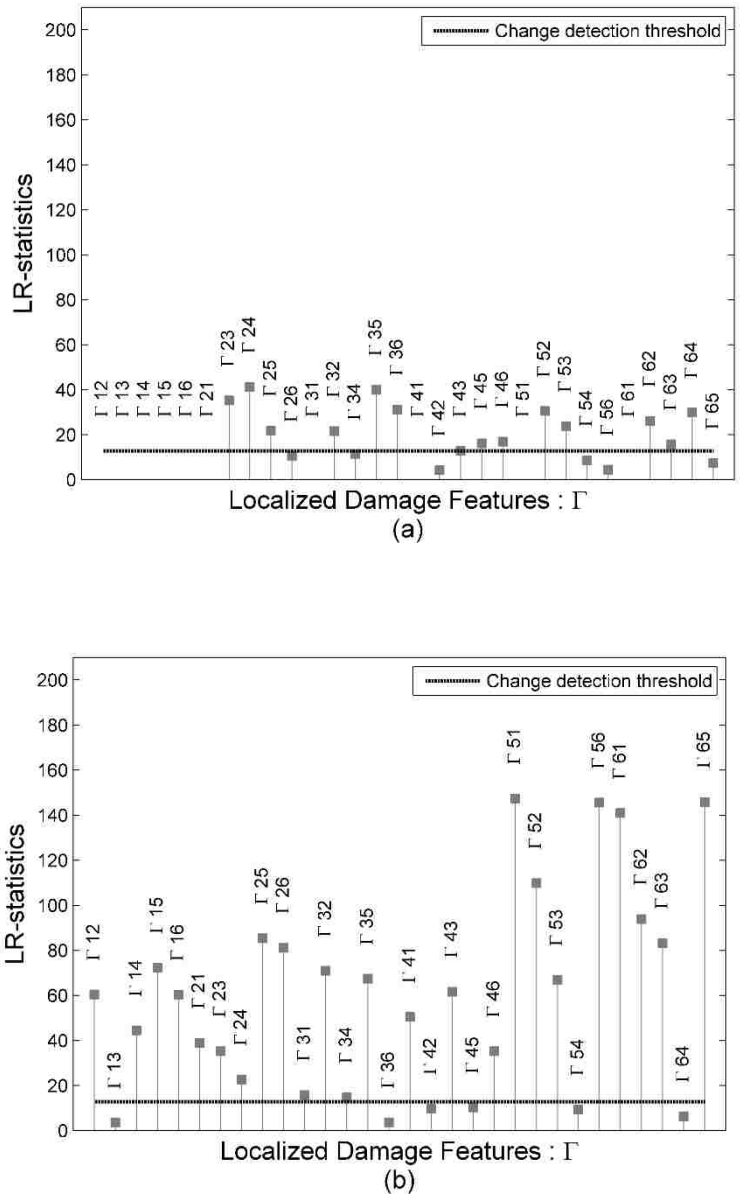

Figure 6.8. The LR-statistics of the Angle Coefficients extracted from the ARX models (split at 20th run): (a) at the LEFT side and (b) at the RIGHT side

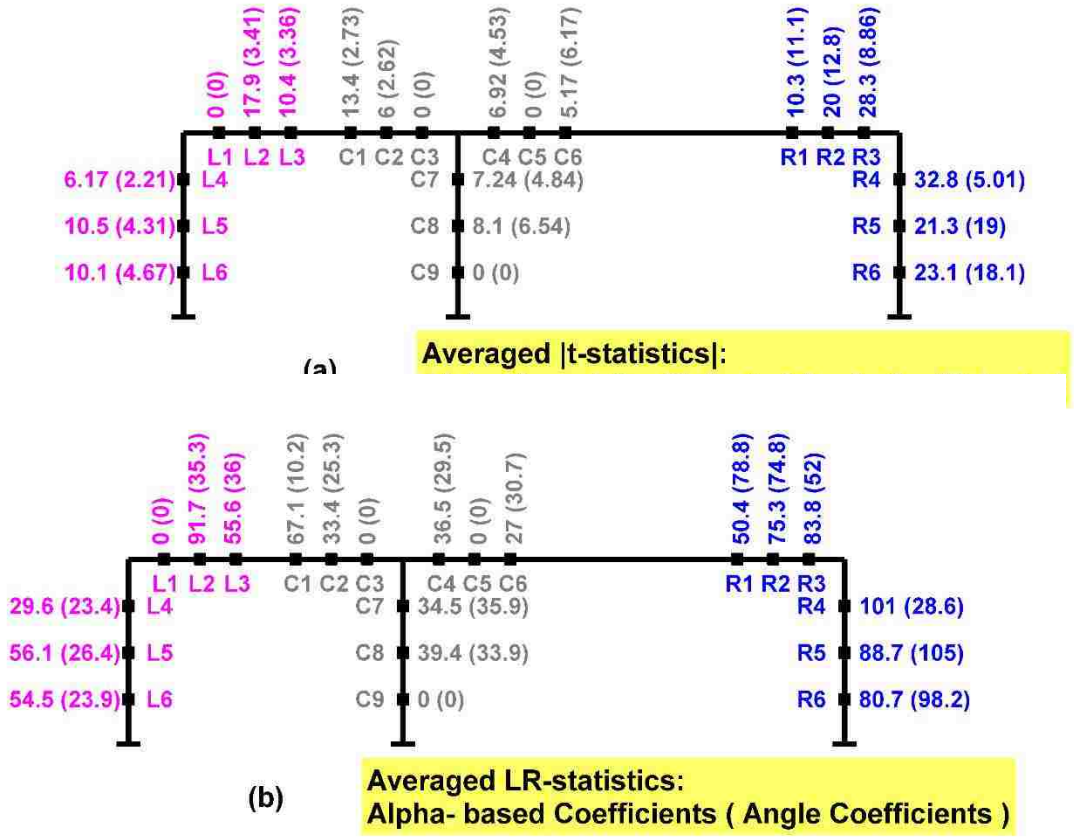

Figure 6.9. Localized damage indicators using ARX models: (a) Average absolute t-statistics, (b) Averaged LR-statistics

6.6.3. Collinear regression results

Collinear Regression (CR) in this implementation involves three different locations. In effect, the results may show a more localized detection of damage because the coefficients themselves include a higher spatial distribution. It is still expected that the coefficients with combinations of the locations on the right side column will show more significant change than those extracted from the left side of

the frame. The results for the *Alpha-based* and *Angle Coefficients* are shown in figure 6.10. These plots are initially analyzed for the timing of damage.

All plots show a peak when the vector of the coefficients is split at the 20th run of testing. As these peaks occur above the change threshold with 95% confidence level, it can be concluded that this is the correct time of the damaging event. The results can then be analyzed for their effectiveness in localizing the damage to the right side column of the frame. Figure 6.11 shows the localized damage indicators. This figure shows that the *Angle Coefficients* generated from CR models find the true location of the damage (R5) using LR- or Student's t-test, while the performance of the *Alpha-based Coefficients* depends on the test statistics; location of the damage is pinpointed to the location of sensor C6 when using t-test, and R6 using LR-test.

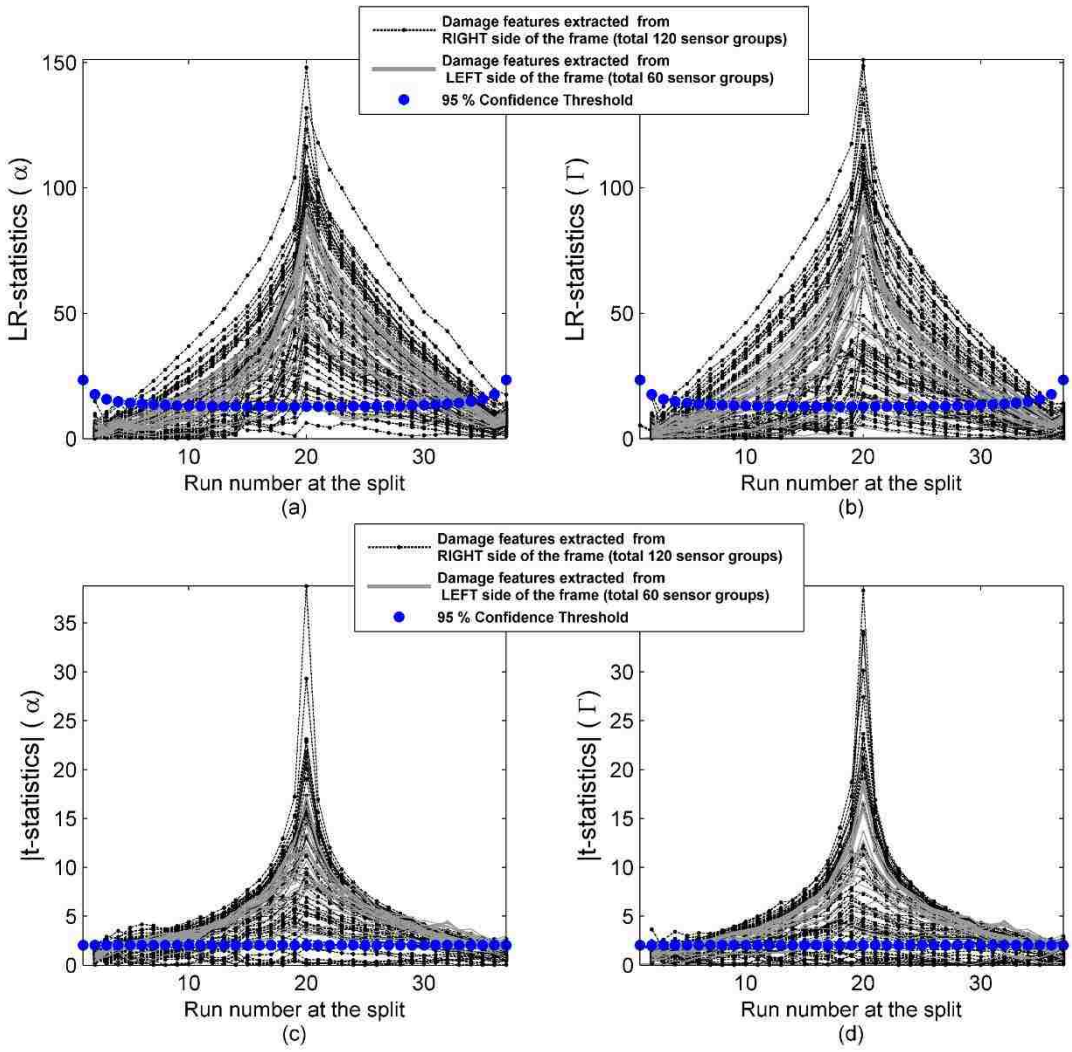

Figure 6.10. Test statistics of the damage features extracted from the CR models: (a) LR-statistics, Alpha-based Coefficients; (b) LR-statistics, Angle Coefficients; (c) absolute t-statistics, Alpha-based Coefficients; (d) absolute t-statistics, Angle Coefficients

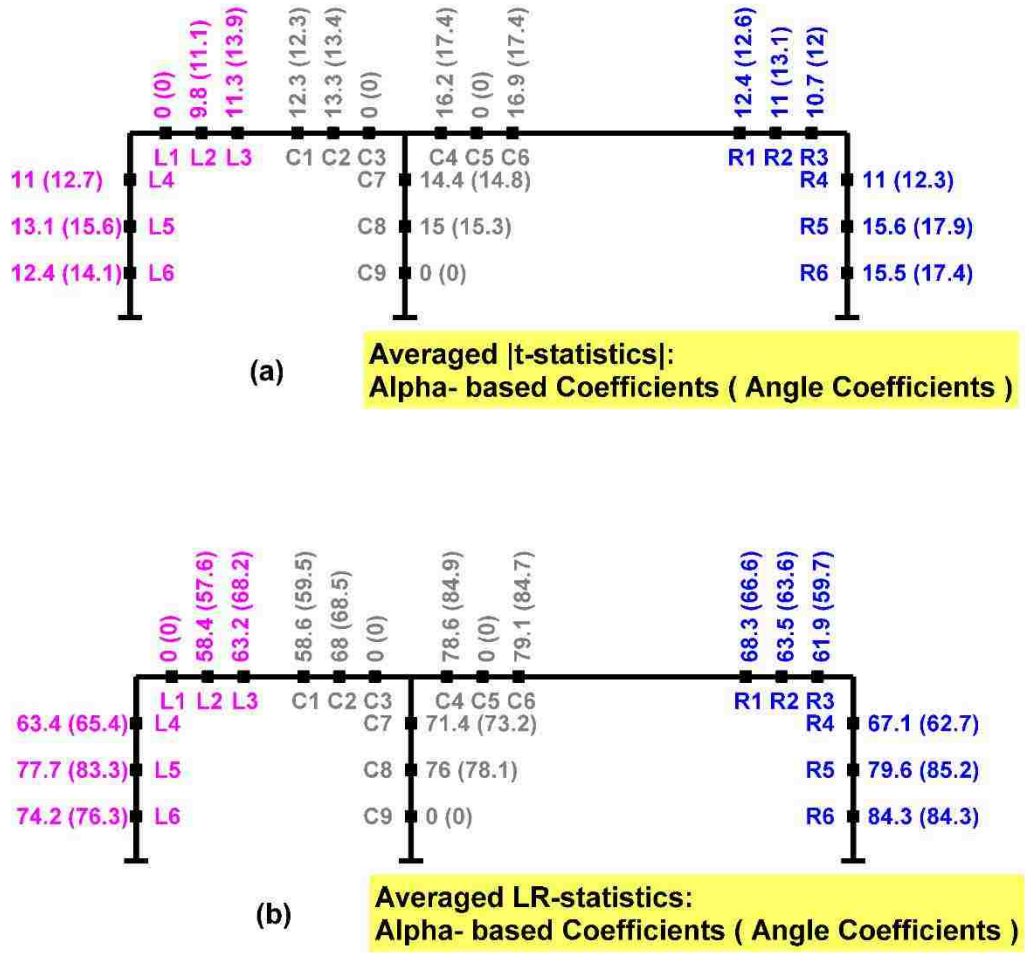

Figure 6.11. Localized damage indicators using CR models: (a) Average absolute t-statistics, (b) Averaged LR-statistics

6.6.4. AR model results

AR models are also tested in the developed damage detection strategies. The *Alpha-based* and *Angle Coefficients* in this case are generated as for the ARX models. These coefficients are different from those generated based on the ARX models, in that the damage features extracted from the AR models represent one sensor node on

the frame. Figure 6.12 summarizes the results of the two-sample change detection on the extracted damage features from AR models. These figures show that for the AR models, the peaks of the change point test statistics are not as distinct as in the previous cases. While using the Mahalanobis distance, the timing of the damage is detected correctly, the *Angle Coefficients* are not successful in detecting the time or location of the damage with this model. The LR-test statistics are shown in Figure 6.13 for *Alpha-based Coefficients* when data is split at 10^{th} run. This figure shows that the extracted damage features are not successful in pinpointing the damage to its true location. This is most likely due to the fact that the simulated damage in this experiment (20% stiffness reduction in a 0.2 m long segment of one of the columns) does not significantly change the natural vibration frequency of the frame as well as the characteristic roots of the AR models extracted from the acceleration response of the frame at different locations. Additionally, Yao and Pakzad (2012) showed that estimates of such AR coefficients has low robustness to environmental factors and measurement noise, and therefore to use the AR model for structural damage detection purposes other damage features such as autocorrelation function of the AR residuals and AR model spectrum are more promising.

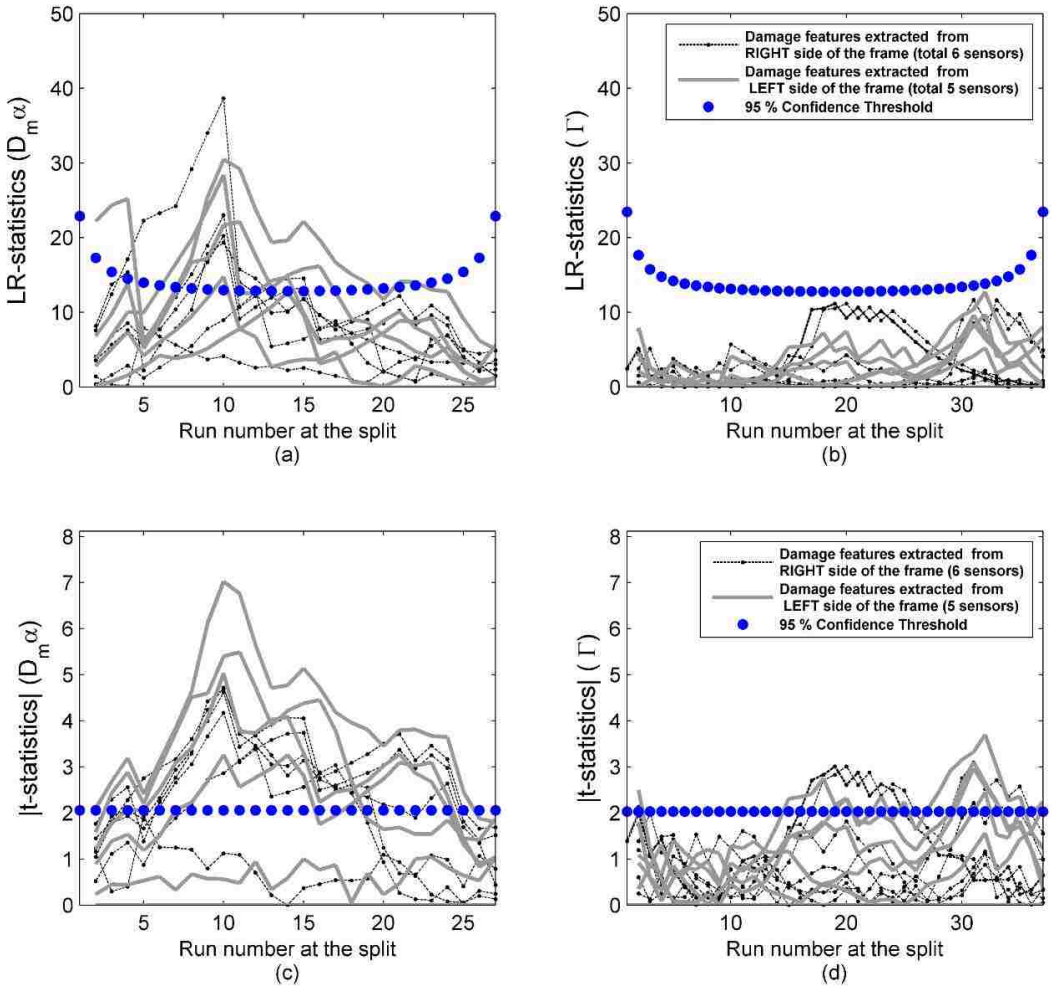

Figure 6.12. Test statistics of the damage features extracted from the AR models: (a) LR-statistics, Alpha-based Coefficients; (b) LR-statistics, Angle Coefficients; (c) absolute t-statistics, Alpha-based Coefficients; (d) absolute t-statistics, Angle Coefficients

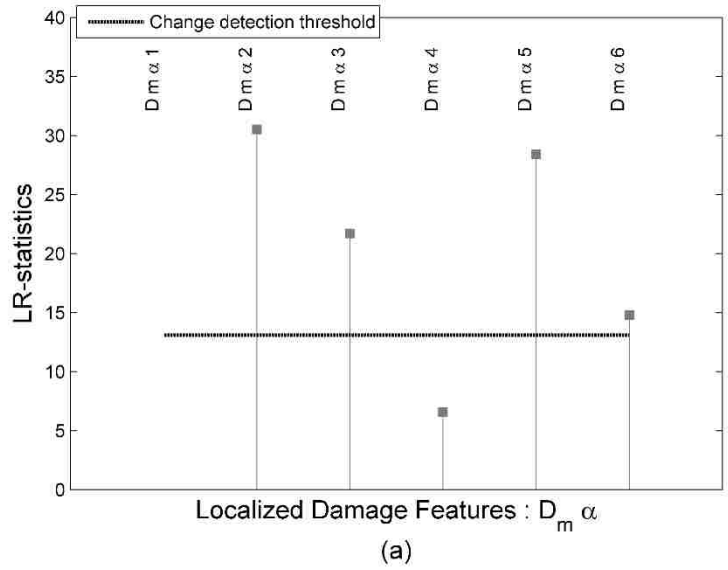

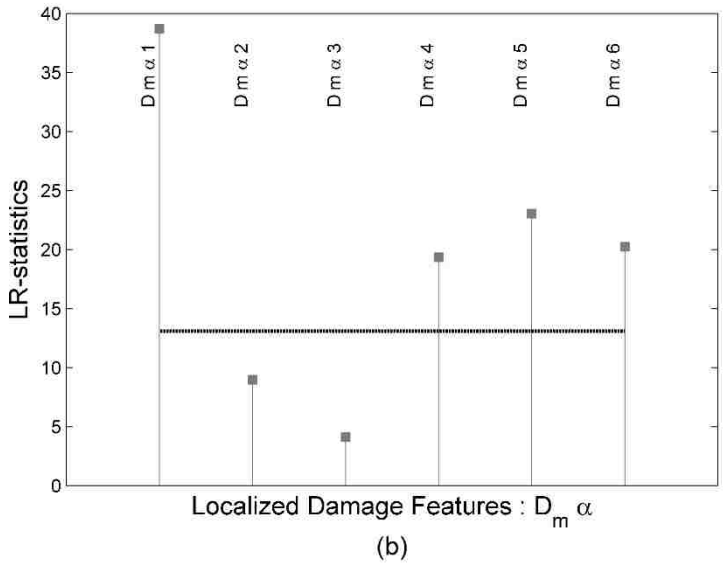

Figure 6.13. The LR-statistics of the Alpha-based Coefficients extracted from the AR models (split at the 10th run): (a) at the LEFT side and (b) at the RIGHT side

6.6.5. False detection check

Prior to concluding that the proposed damage detection methods are viable ways of identifying the structural damage, their false detection quality should also be tested.

For this purpose, these methods are iterated on a group of 40 runs consists of the first 20 tests on the healthy configuration of the frame combined with a random permutation of these 20 runs. As all the tests are from the same structural condition, it is expected that no damage is detected using the damage sensitive features in this case. Figure 6.14 shows the LR- and t-statistics extracted from the coefficients of the SVR, ARX, CR, and AR models for these 40 sets of data from the undamaged state, along with the change detection threshold corresponding to 95% confidence level. This figure shows that when all the observations belong to one state of system, no large and distinct peaks are evident above the change threshold as in the previous cases. However, it is also seen that some of the statistics do cross the change threshold. This does not signify damage as it is consistence with average false detection of the corresponding tests on observations from a normal distribution at 95% confidence level.

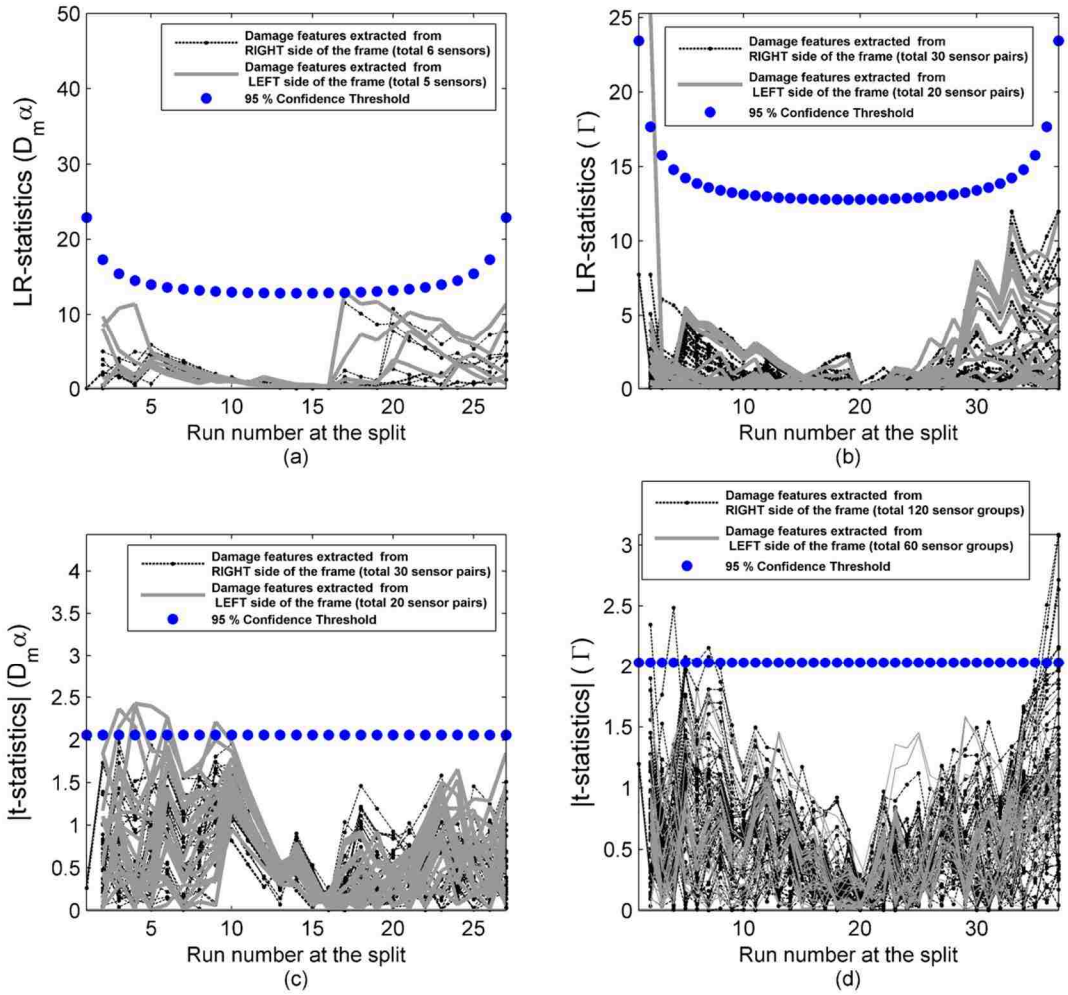

Figure 6.14: Test statistics of the damage features extracted from different regression models: (a) AR model, LR-statistics, Alpha-based Coefficients; (b) SVR model, LR-statistics, Angle Coefficients; (c) ARX model, absolute t-statistics, Alpha-based Coefficients; (d) CR model, absolute t-statistics, Angle Coefficients

6.7. Summary and Conclusions

This study is concerned with the effectiveness of different damage features and multivariate linear regression models used in data-driven structural damage identification. For this purpose, a successive normalized likelihood ratio test and a sequential two-sample t-test are adopted to test the change in two different damage

sensitive features based on the regression coefficients of four different linear regression models (SVR, CR, ARX, and AR models). This methodology is tested on a scaled two-span frame in which damage is simulated by switching a segment of one of the columns with a section with 20% less stiffness. It was observed that all of the mathematical models were successful in identifying the occurrence of the damage, except when the *Angle Coefficients* from AR models were tested. The location of damage was then identified based on the test statistics from SVR, CR, and ARX models. These results are summarized in Table 6.2. This table shows that the *Angle Coefficients* have a better performance in localizing the damage, as in all cases the simulated structural damage is localized to its true or neighboring sensor node. *Alpha-based Coefficients, however,* perform less accurate and robust in damage localization; their damage localization performance depends on the underlying mathematical model and the change point test statistics. It is also observed that the ARX model has the most accurate localization estimate regardless of the test statistics used, and its performance is improved in combination with the proposed *Angle Coefficients*.

It should be noted that in any damage detection experimental testbed similar to the one used here, assembly procedure for simulation of damage could change the system and generate misleading results in the change point analysis. To address this issue, note the following: (1) through the presented methods, damage is successfully localized to its true neighborhood, (2) damage detection methods in this chapter are all model-free techniques. Model-based damage detection methods with appropriate parameterization could have benefits of detecting such changes, and (3) the

consistency of the assembly of the testbed was examined in preliminary experiments, by repeating the experiments in healthy/damaged states. A procedure for the sequence of testbed assembly is established to ensure that the results remain consistent.

Table 6.2. Summary of the damage identification of the steel girder

	Identified damage location*			
Change point method	***t-test***		***LR-test***	
Damage features	*Alpha-based Coefficients*	*Angle Coefficients*	*Alpha-based Coefficients*	*Angle Coefficients*
SVR model	R6	R6	R6	R6
ARX model	R4	R5	R4	R5
CR model	C6	R5	R6	R5

**** True damage location is R5***

Since the false detection quality of the proposed methods were also verified using data sets from the healthy condition of the structure, it can be concluded that these methods are viable techniques to identify and locate damage in structural systems. It was shown that incorporating multiple mathematical models, damage sensitive features and change detection tests improve the overall performance of these model-free structural damage detection when impact loading is used to dynamically excite the steel frame. This shows potential application of such methodologies in automated damage localization during events like earthquake; however, in order to extend the application of these methods, their performance should also be evaluated using ambient vibration as excitation in future research. In addition, in this single damage scenario, it was observed that when damage features are developed based on relative change in the acceleration response at nodes inside each sensor cluster, occurrence of damage could be statistically identified even using the data from a sensor that is

located relatively far from the damaged member. This implies that these methods are most likely capable of detecting the timing of damage in multiple damage scenarios as well.

Chapter 7

Structural damage identification with a compressed sensing approach

This chapter extends the data-driven damage detection methods presented in the previous chapter into a damage localization technique with a compressed sensing (CS) approach. The motivation is to identify the least amount of data that is required to process in order to successfully localize structural damage in its early stage. This is important because the volume of monitoring data is growing drastically with improvement in sensing technology. Therefore, while installing high resolution sensing networks has become affordable, the requirements for data storage and processing the monitoring data could become a bottleneck for the previously damage detection algorithms which work on the basis of analyzing the entire collected data set in order to make a decision (Matarazzo et al. 2015). This has become a concerning issue in the SHM field in the recent years, and research is ongoing to find efficient ways of processing, transmitting, and storing the monitoring data while maintaining comparable accuracy in the results. Some of the works in this area have investigated this issue in SHM applications for the purpose of modal identification, while others tackle the problem of compressed data-driven damage detection. Bao et

al. (2013) proposed and validated a CS-based approach for the acceleration time series recovery and modal parameters identification on data collected from the Jinzhou West Bridge and the Structural Health Monitoring System on the National Aquatics Center in Beijing. The results indicated that recovery accuracy depends on the sparsity characteristic of the collected signals in some orthonormal basis. O'Connor et al. (2014) proposed a CS strategy for sub-Nyquist random sampling and off-line target signal reconstruction to perform modal identification on a three span highway bridge instrumented with wireless sensor network. Haile and Ghoshal (2012) presented a CS technique for reconstruction of full-field strain data from discrete strain samples in a numerical experiment. Mascareñas et al. (2013) implemented a prototype compressed sensor that can collect compressed coefficients and send it to off-board processer for reconstruction, also investigated the suitability of the CS coefficients for damage detection. Zhou et al. (2013) proposed a structural damage identification method based on the sub-structure-based sensitivity analysis and the sparse constraints regularization. Finally, Yao et al. (2015) proposed a compressive sensing damage detection method based on spatial correlation of random samples and Ant Colony optimization.

In this chapter a CS-based damage localization algorithm is proposed which performs based on three components of random sensor location sampling, change point analysis, and recursive Bayesian probability estimation. The damage detection starts with selecting a subset from entire monitoring network. Data from these sensors are processed for feature extraction and change point analysis. When the

change point analysis signifies a potential candidate for damage location, neighborhood of the suspect location is investigated further in a local sampling step. A recursive Bayesian estimation procedure is also adopted in order to iteratively update the probability of damage location as data from more sensors are considered for processing. This procedure is terminated when damage is localized with a certain probability. The following sections of this chapter describe this damage localization methodology in details. Performance of this technique is also shown using a FE model of a steel gusset plate.

7.1. Compressed damage detection and localization: single damage scenario

The data-driven damage detection methodology proposed here consists of iterative global and local sampling steps from a dense sensor network. With a uniform prior probability for the location of damage, the global sampling step starts by taking samples uniformly from the entire sensor network. This iterative global sampling ensures high reliability in finding a proper start point to establish an initial local search boundary. Data from the sampled sensors are processed for feature extraction and statistical testing based on change detection methods. As test statistics from sampled sensor locations cross the specified change threshold, likelihood of the damage location is calculated, and is used to obtain the posterior probability of the damage location. The local sampling steps start with taking samples inside a smaller window centered on the location with maximum posterior probability. The steps of local sampling, feature extraction, change point analysis, likelihood and posterior

probability estimation are repeated until damage is localized beyond a pre-specified probability threshold. The local sampling window is also updated if a new sampled point reveals the highest change statistics over the current search window. Figure 7.1 shows the details of the proposed method in a flowchart. As this figure indicates, in the case of multiple damage detection, first number of desired local search boundaries are assumed (N_w). Then kmean clustering algorithm (Lloyd 1982) is used to divide the change points into N_w classes to set N_w search boundaries where a separate local search begins using a moving window as explained before.

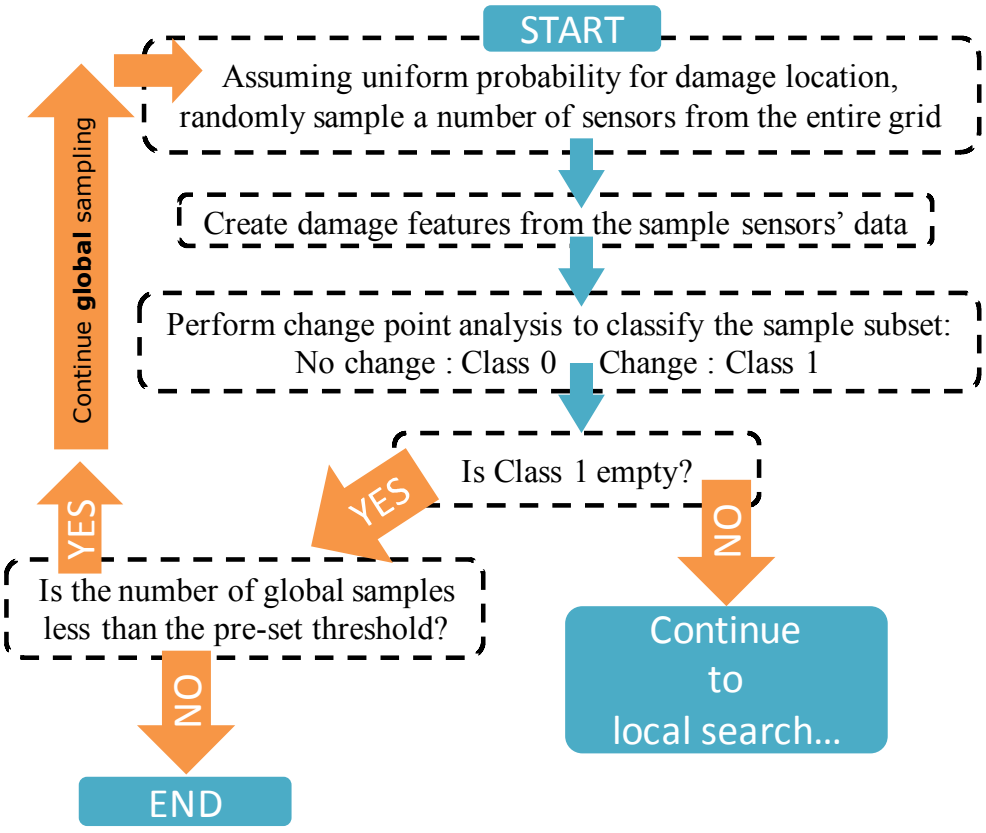

Figure 7.1. (a) Flowchart of the proposed compressed damage localization algorithm

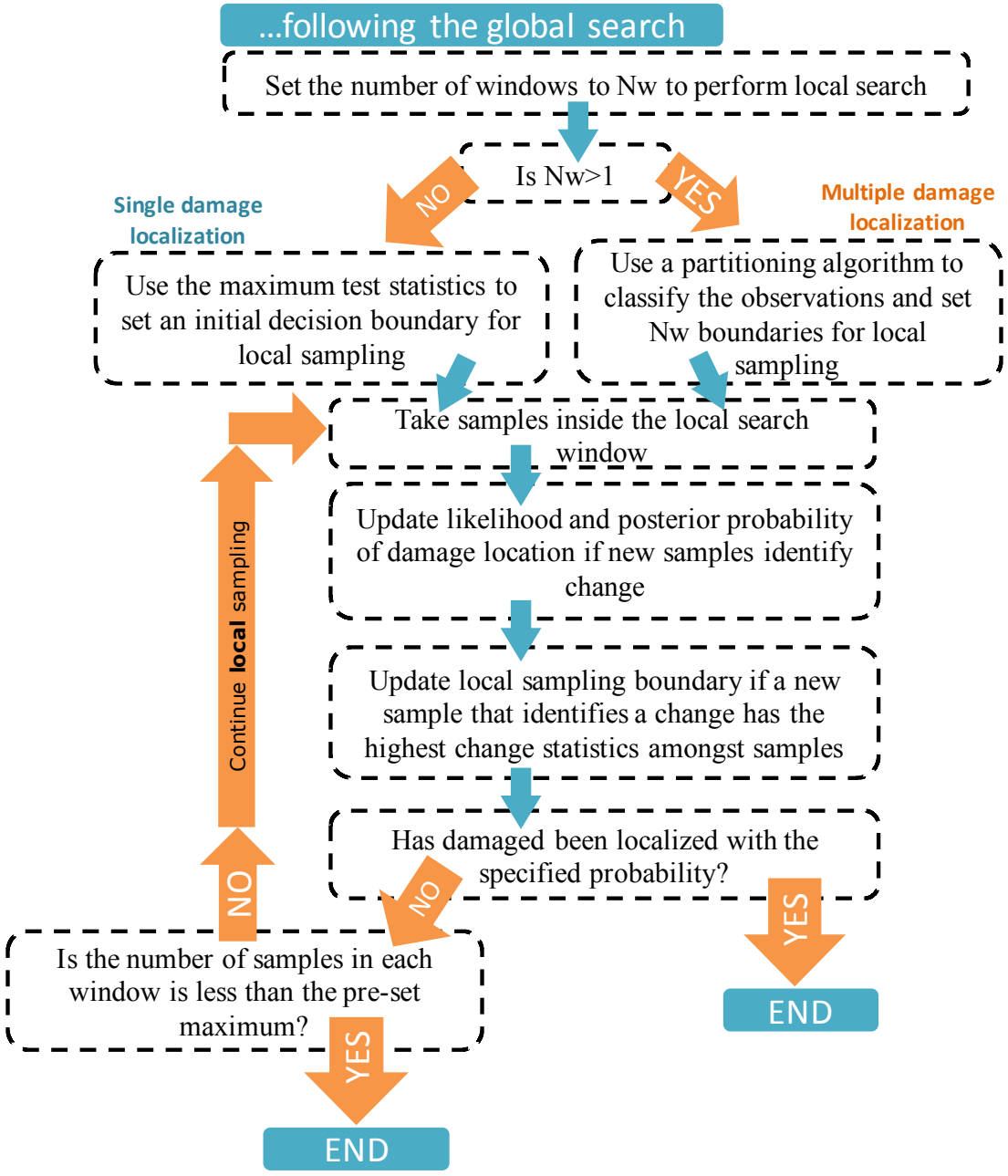

Figure 7.1. (b) Flowchart of the proposed compressed damage localization algorithm

7.2. Application of the Proposed Compressed Damage Detection Algorithm on a Steel Gusset Plate Simulation

Accuracy and robustness of the proposed compressive damage diagnosis framework is evaluated through FE simulations of damage and undamaged structural connections used to generate strain data. Figure 7.2 shows the simulated two-way gusset plate connection used for numerical validation in this research. The assembled connection is 52 inches long and undergoes a 50 kips (222.4 kN) axial tensile load. It should be noted that the gusset plate is designed to withstand up to 100 kips (444.8 kN) of axial tensile force. The simulated damage is a one inch long cut in the free section of the gusset plate. Figure 7.3 and 7.4 show the FEM of the simulated single and multiple damage cases. Strain filed of the gusset plate before and after damage is used to simulate the test data. In both damaged and undamaged cases, Gaussian noise is added to the data to create a more realistic monitoring scenario and generate 30 sets of strain data for each structure's health condition.

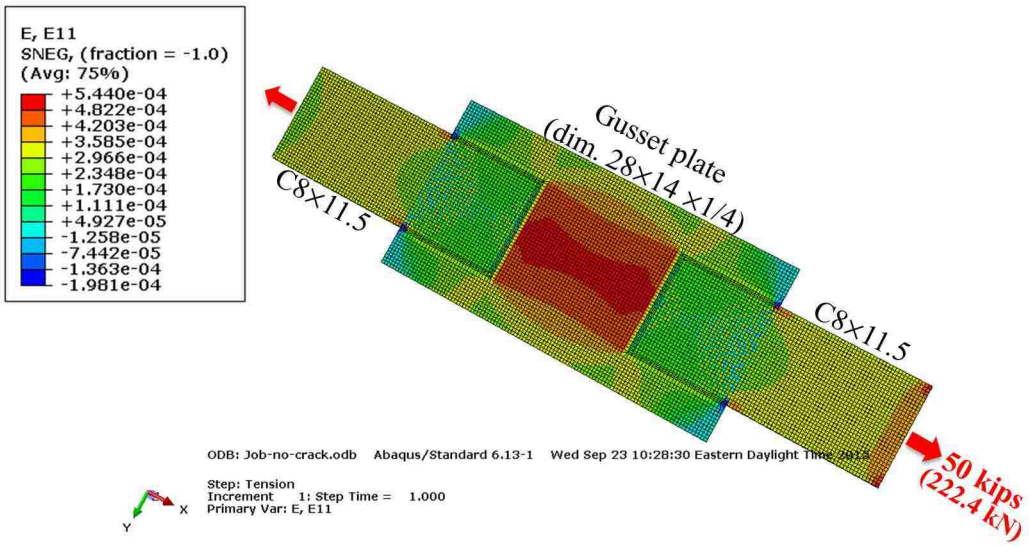

Figure 7.2. Simulated gusset plate connection under axial loading: undamaged state

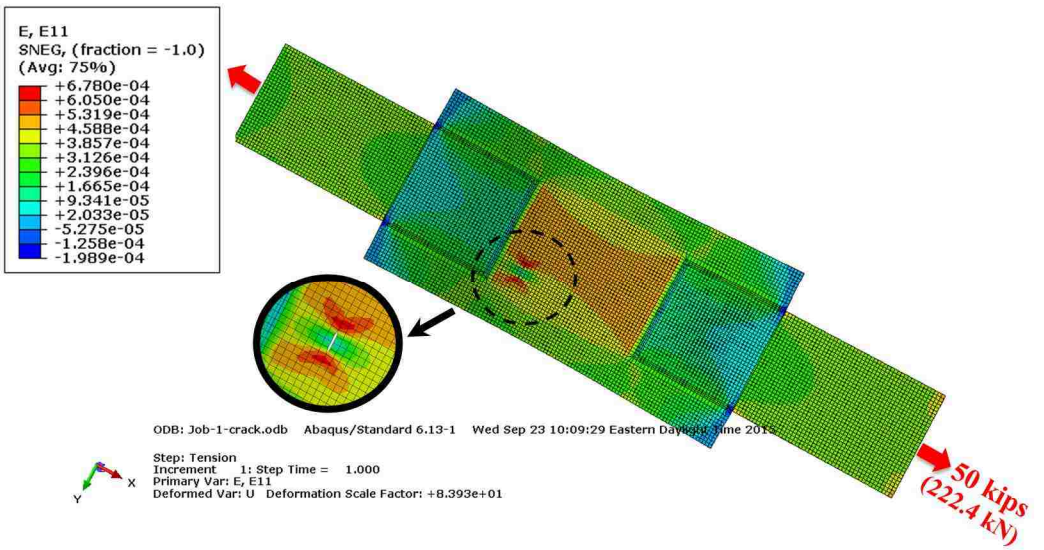

Figure 7.3. Simulated gusset plate connection under axial loading: single damage scenario

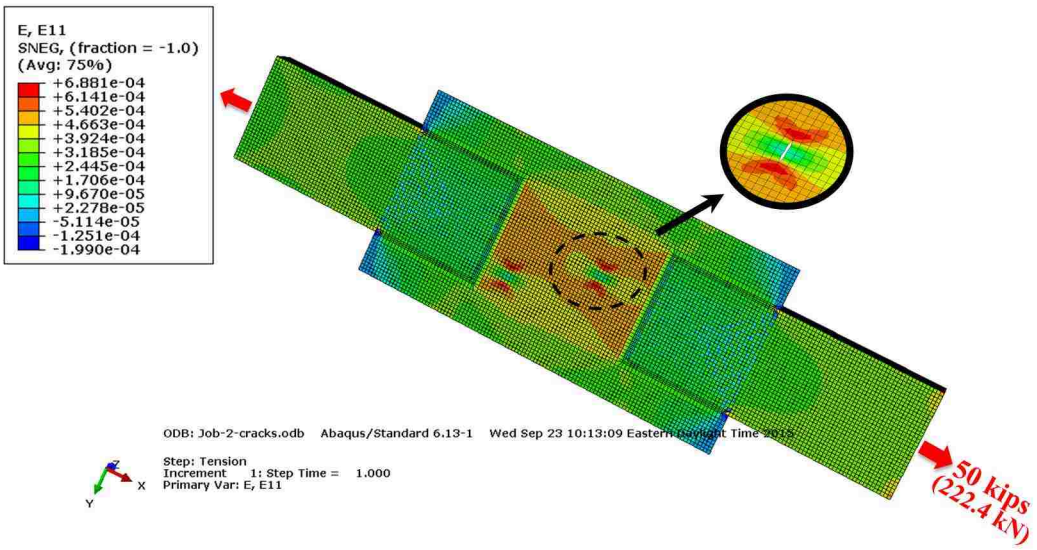

Figure 7.4. Simulated gusset plate connection under axial loading: multiple damage scenario

7.3. Damage Features Extraction

The damage features used in this study is a dimensionless scalar feature based on the relative change in the strain at neighboring grid nodes. Since direction of the potential cracking is not known in real damage cases, this feature establishes a relationship between strain at every node of the FE mesh and those from points close to that node in the two orthogonal directions. Eq. (7.1) shows this damage feature. In this equation $\varepsilon_{i,j}$ denotes strain at a node with coordinate (i,j).

$$DF_{i,j} = \left|\frac{\varepsilon_{i,j}}{\varepsilon_{i+2,j}}\right| + \left|\frac{\varepsilon_{i+2,j}}{\varepsilon_{i,j}}\right| + \left|\frac{\varepsilon_{i,j}}{\varepsilon_{i,j+2}}\right| + \left|\frac{\varepsilon_{i,j+2}}{\varepsilon_{i,j}}\right| \tag{7.1}$$

When the gusset plate is intact, each term in Eq. (7.1) is close to unity, since there is no abrupt change of strain between neighboring nodes in the middle section of the

gusset plate. When a crack is formed; however, a drastic change in the vicinity of the crack occurs in form of stress reduction along the cracked section and intensified stress around the crack tips. With these changes, the damage features would deviate from their counterparts extracted from the "healthy" state of the structure. In order to statistically test the significance of change in these damage features, vectors of features shown in Eq. (7.1) from damaged and undamaged FE models are tested to find a statistically significant change in their means.

7.4. Change Point Analysis

In order to test the change in the damage sensitive features described before, two-sample t-test is used here. This control statistics is based on the Student's t-test and is a common procedure for testing the significance of difference between the means of two samples (Montgomery and Loftis 1987), and has been successfully adopted for data-driven damage detection (Labuz et al. 2010, Shahidi et al. 2014). The statistics of this test has N-2 degrees of freedom (N being the combined length of the two sample vectors) and is given in Eq. (7.2):

$$t = \frac{\hat{X}_1 - \hat{X}_2}{S_p \sqrt{(1/n_1) + (1/n_2)}} \tag{7.2}$$

where the variables $\hat{X}_1$ and $\hat{X}_2$ are the means, n_1 and n_2 are the sizes of the two samples, and S_p represents their pooled standard deviation. Upper and lower control limits for this test are then calculated using the Student's t inverse cumulative distribution function at a certain confidence level and N-2 degrees of freedom. When a

vector of test statistics crosses these control limits, significance of the change in the statistics is inferred. As sensors are located closer to the location of damage, their change statistics increase. This is the basis for finding the location of damage.

7.5. Recursive Bayesian Estimation

In the proposed algorithm, a Bayesian estimation framework (Thrun et al. 2005) is adopted to find the probability of damage over the sensor network to terminate the sampling process when enough evidence is available for damage localization. This Bayesian estimation process starts with a uniform prior for the entire grid of the FE mesh under investigation. A bivariate Gaussian model is then utilized to find the likelihood of each damage location hypothesis with respect to the new detected change point. Eq. (7.3) shows the formulation of this bivariate Gaussian model, where D_k shows the coordinate of the k[th] detected change point (i.e. $D_k = [xd\ yd]_k$) and $H_{x,y}$ represents the hypothesis that damage is located at the coordinate (x,y).

$$L(H_{x,y}|D_k) = \frac{1}{\sqrt{(2\pi)^2|\Sigma|}} \exp\left(\frac{-(D_k - [x\ y])\Sigma^{-1}(D_k - [x\ y])^T}{2}\right) \tag{7.3}$$

Eq. (7.4) shows the k[th] iteration in the Bayesian estimation process.

$$Po_k(H_{x,y}) = \frac{\Pr_k(H_{x,y})L(H_{x,y}|D_k)}{\sum_x \sum_y \Pr_k(H_{x,y})L(H_{x,y}|D_k)} \tag{7.4}$$

In this equation Pr_k and Po_k respectively indicate prior and posterior probability of damage for the k^{th} iteration. As stated before, when k equals one, a uniform prior is used as there is no knowledge about the location of damage prior to observing a significant change in the sampled sensors' data. When k exceeds one, posterior probability estimated in the previous step (i.e. $Po_{k-1}(H_{x,y})$) is recursively used as the prior probability of the damage location.

7.6. Results

This section presents the results of the proposed damage detection method applied on the data simulated with the FEM of the Gusset plate shown before. Figure 7.5 shows the complete feature domain for the single damage scenario when simulated noise has a small amplitude; at each node standard deviation of the noise signal is 1% of strain value. In the probability estimation step, for the likelihood function, standard deviation of 3 for detection in x and y direction with zero correlation is assumed. The damage detection is terminated when with 90% probability damage is localized to four sensor locations, which in effect would be the smallest block size for the simulated sensor network. Figure 7.6 and 7.7 shows the results of the single damage localization algorithm when noise level is 1% and 10% respectively. Figure 7.8 compares the entire feature domain with the compressed features when noise level is 10% and a compression ratio of 90.9% is obtained. Figure 7.9 and 7.10 shows the results of multiple damage detection scenario with 5% noise level, compression ratio in this

case is 86.3%. It should be noted that in all these cases, the global sampling starts with sampling 4% out of the entire feature domain.

Since the global sampling step establishes the local sampling boundary, it is important to investigate the effect of the ratio of global sampling on the damage localization results. The damage detection is repeated in several cases where global sampling ratio is varying from 2% to 20%. In order to consider the variation in the measurement noise, 50 different noise simulations is performed for each case. Table 7.1 and 7.2 shows the results of damage detection for single and multiple damage scenarios with different global sampling ratio. It is observed that with 4% global sampling, single damage localization would be successful with high reliability (98%). However, in the case of multiple damage detection, it would be better to start with higher global sampling ratio to have about 90% reliability for correct damage detection.

Finally, the robustness of the proposed methodology to the measurement noise is investigated by considering different noise amplitudes. For each noise level, 50 sets of simulation are performed and single damage detection procedure is repeated. Table 7.3 summarizes the results of these simulations in terms of successful detection and compression ratio. This table shows that as noise level is increasing, the successful detection performance is deteriorating; however, in the successful cases the compression ratio is still very high (more than 85%).

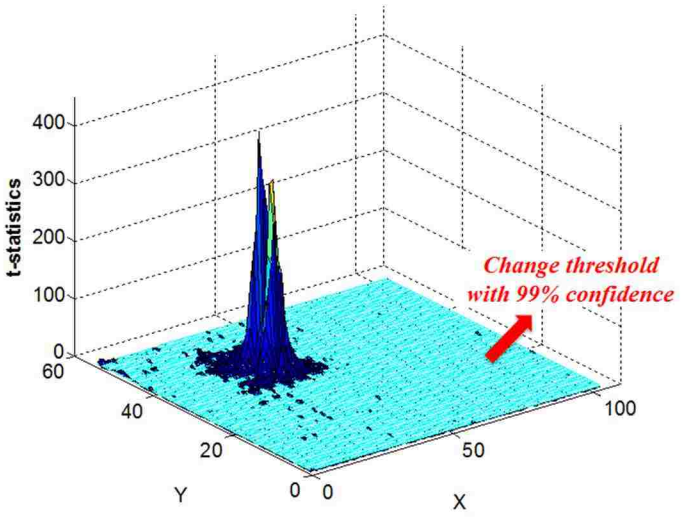

Figure 7. 5. Damage features: single damage scenario, 1% noise

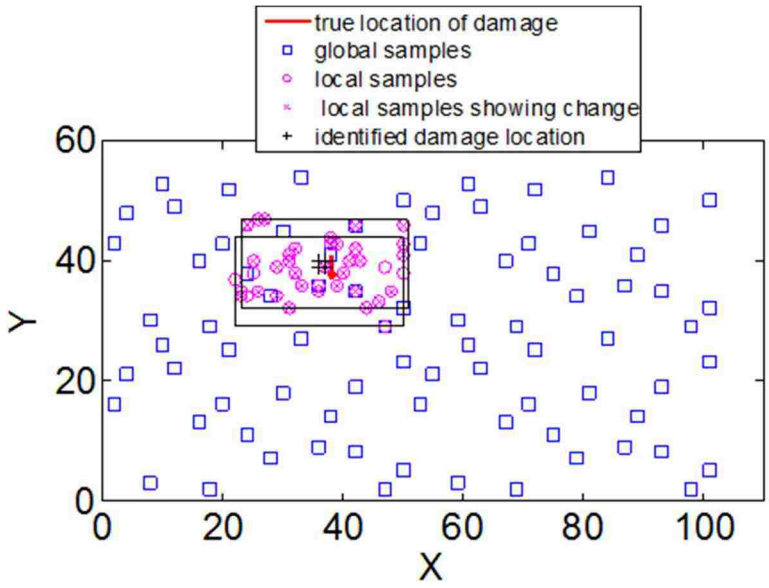

Figure 7. 6. CS damage detection results: single damage scenario, 1% noise

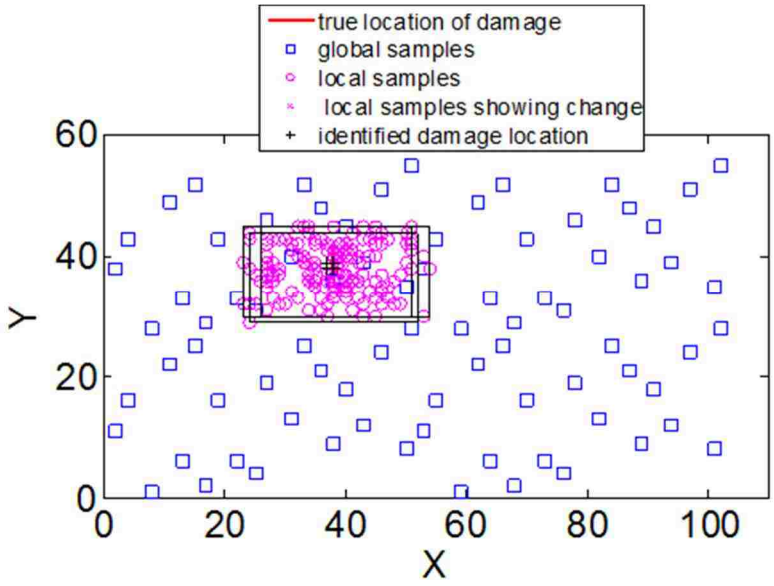

Figure 7. 7. CS damage detection results: single damage scenario, 10% noise

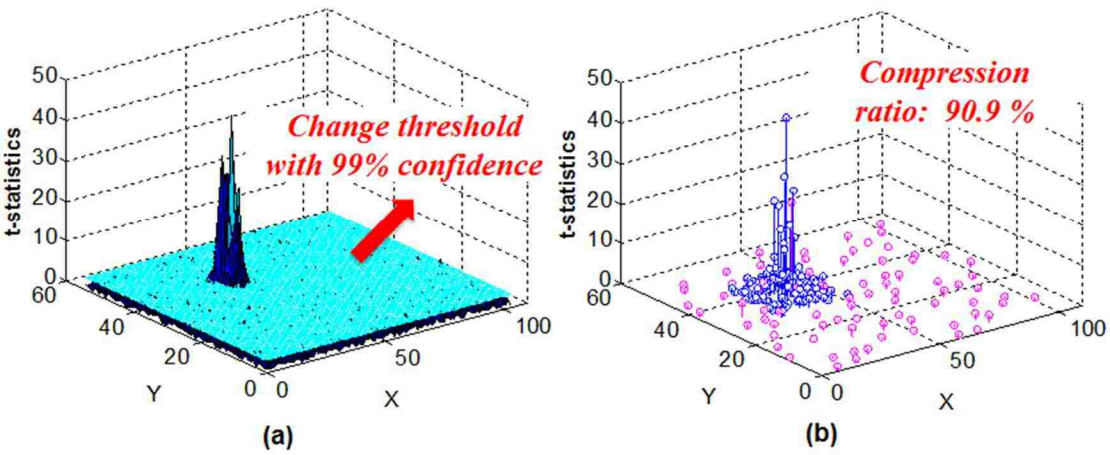

Figure 7. 8. (a) Entire damage features, (b) compressed damage features single damage scenario, 10% noise

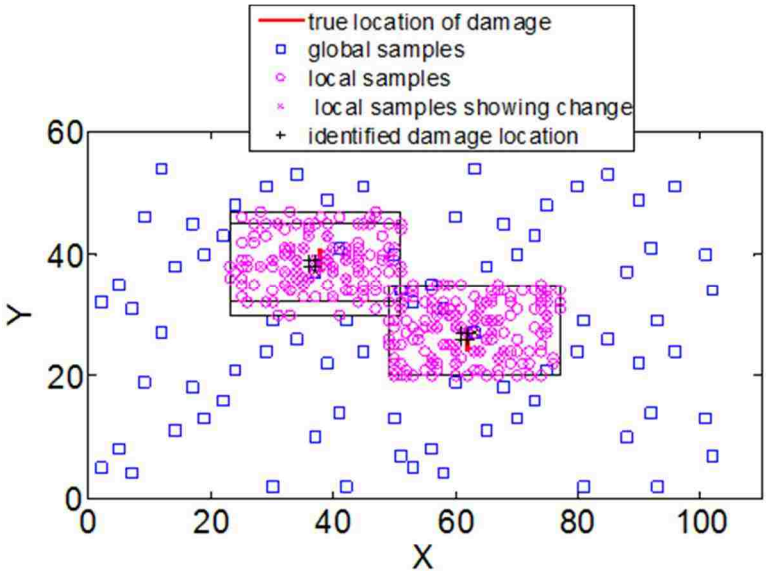

Figure 7. 9. CS damage detection results: double damage scenario, 5% noise

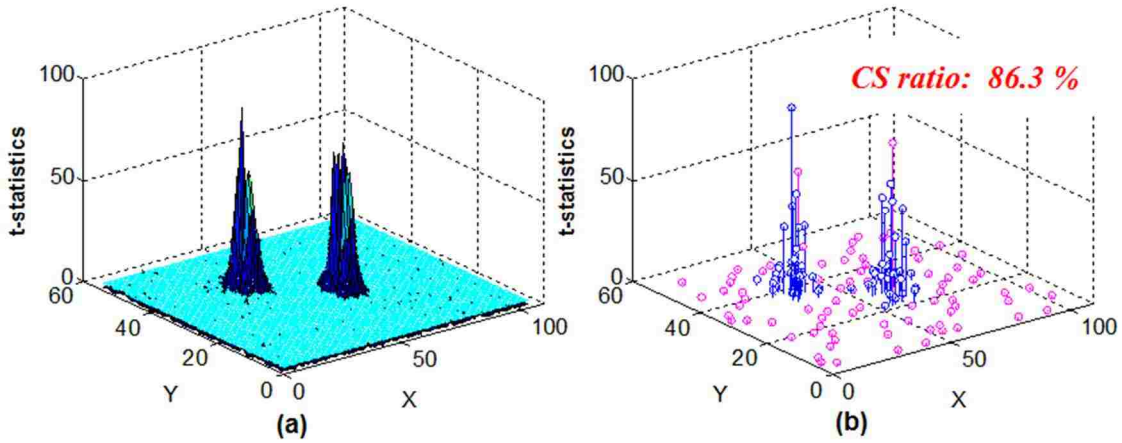

Figure 7. 10. (a) Entire damage features, (b) compressed damage features double damage scenario, 5% noise

Table 7. 1. Comparison of the performance of CS damage detection with different global sampling: single damage scenario, 5% noise

global sample (%)	2	4	10	20
successful detection (%)	94	98	100	100
average compession ratio (%)	92.6	91.0	85.6	76.7

Table 7. 2. Comparison of the performance of CS damage detection with different global sampling: Multiple damage scenario, 5% noise

global sample (%)	2	4	10	20
successful detection (%)	40	78	88	92
average compession ratio (%)	87.3	85.6	80.6	72.2

Table 7. 3. Comparison of the performance of CS damage detection with different noise level: Single damage scenario, 4% global sampling

noise level (%)	1	5	10	15
successful detection (%)	100	98	84	68
average compession ratio (%)	94.1	91.0	88.2	85.5

7.3. Summary and Conclusions

This chapter presents a methodology for compressed damage diagnosis. The main motivation for developing such damage detection methods is to improve the scalability of damage diagnosis frameworks. With rapid advancement in SHM hardware over recent decades, dense contact and non-contact sensor networks are readily used in the monitoring projects, and thus measurements with high resolution

in time and space are obtained. While higher resolution measurement techniques could be beneficial in accurate structural damage detection, it is important to improve the scalability of damage detection algorithms for processing the SHM BIG DATA. The proposed algorithm in this chapter aims to present a method that accurately localize damage in the structure, while a very small subset of sensor nodes are used for processing. The method works on the basis of change point analysis and recursive Bayesian probability estimation. This algorithm is applied for damage detection in a simulated gusset plate under axial loading. A single and a multiple damage scenario is considered by introducing one-inch long cuts in the gusset plate. Thirty sets of noisy strain field are generated from undamaged and damaged states of the structure. The effect of global sampling on the damage detection performance is investigated. The multiple damage scenario is seen to be more sensitive to the global sampling rate. The success rate in this case is more than 75%, when damage detection starts with only 4% of the entire data. Different noise amplitudes are considered to investigate the robustness of the proposed methodology to the measurement noise. For each noise level, 50 sets of simulation were performed and damage detection procedure is repeated. The results show that with processing less than 15% of the monitoring data, this procedure is successful in single damage localization for low and moderate noise levels.

Chapter 8

Contributions and Future Directions

8.1. Contributions

This dissertation presents model-based and model-free algorithms for processing SHM data. The research presented in this dissertation can be divided into four parts: (1) developing a non-linear FEM updating algorithm and validation of its performance in terms of accuracy, computational cost, and robustness, (2) damage assessment and fragility analysis of the Washington Monument following 2011 Virginia earthquake through modal identification and model calibration, (3) developing and comparing data-driven damage detection methods, and (4) a compressed sensing damage detection algorithm is proposed and applied to localize cracks in a steel gusset plate connection. This section presents a summary of contributions of different parts of the research presented in this dissertation.

The contribution of the first part of this research is to develop a surrogate-based non-linear FEM updating algorithm (called GRSMU), through which appropriate RS models are created to replace the non-linear FEM in the minimization problem of model calibration. Performance of GRSMU in terms of accuracy and computational cost was compared with sensitivity-based model calibration; the most common and

generalized model calibration technique used for this purpose. This comparison shows that GRSMU is computationally cheaper, while having comparable accuracy. The research findings were published in Volume 140 of the Journal of Structural Engineering-ASCE (Shahidi and Pakzad 2014a).

Another contribution of this part is in developing analytical and numerical procedure to investigate the robustness of GRSMU results with respect to the standard deviation of the measurement noise. Several parametric studies were performed on single- and multi-dof structures, and it was observed that for a zero-mean noise structure, the estimation error is fairly insensitive to low and medium measurement noise level. In addition, robustness of the GRSMU results regarding frequency content of the input load was also explored. This was accomplished through assuming a sinusoidal input load on the structure, and change the frequency of this excitation with respect to the fundamental vibration frequency of the structure in several scenarios. It was observed that when the vibration frequency of the system is outside of the frequency bandwidth of the load, the results show the least sensitivity to measurement noise level, selected time window for optimization, and location of the true model parameters in the RS domain. Similar observations were made when GRSMU was used to estimate modeling parameters of an steel frame with bilinear material model under seismic loading. The research findings were published in Volume 75 of the Engineering Structures Journal (Shahidi and Pakzad 2014b).

Contribution of the second part of this dissertation is to present the role that SHM algorithms plays in improving the credibility of damage assessment and seismic

fragility analysis. In this part of the research, a finite element model of the Washington Monument is developed and updated based on the dynamic characteristics of the structure identified through ambient vibration measurement and modal identification after the earthquake. The calibrated model is used to study the potential causes of the observed damage to the Washington Monument during 2011 Virginia earthquake. This FEM is then modified to limit the tensile capacity of the grout material and previously cracked sections to investigate the initiation and propagation of cracking in several futuristic earthquake scenarios. The non-linear FEM is subjected to two ensembles of site-compatible ground motions representing different seismic hazard levels for the Washington Monument, and occurrence probability of several structural and non-structural damage states is investigated. Summary of our findings in the vibration testing and damage assessment phase of the project were published by Geological Society of America in a special paper volume on "*The 2011 Mineral, Virginia, Earthquake, and Its Significance for Seismic Hazards in Eastern North America*" (Shahidi et al. 2015a). Results of the second phase of our research in seismic fragility assessment of the Washington Monument was submitted to Earthquake Spectra Journal and is currently under revision.

In the last part of this research, data-driven damage detection methods are presented and effectiveness of combination of different regression models, damage features, and test statistics are compared. In effect, a successive normalized likelihood ratio test and a sequential two-sample t-test are adopted to test the change in the damage sensitive features extracted from different linear regression models.

This methodology is tested on a scaled two-span frame instrumented with a dense sensor of accelerometers where damage is simulated by switching a segment of one of the columns with a section with 20% less stiffness. It was observed that all of the presented damage detection methods are successful in identifying the occurrence of the damage; however, with different localization accuracy. The contribution of this part is in data-driven damage detection is in establishing and comparing the effectiveness of different regression models, damage indicators, and two-sample test methodologies for SHM applications. In addition, a damage sensitive feature based on the change in the angle of regression coefficient vectors is introduced which is applicable to both single and multivariate regression models. The application of the collinear regression model and sequential two-sample statistical tests for damage detection and localization is also introduced. The paper presenting our contributions in this part was published in the Volume 11 of the journal of Structure and Infrastructure Engineering: Maintenance, Management, Life-Cycle Design and Performance.

Finally, in the last part of this research a compressed sensing data-driven damage detection algorithm is presented. This algorithm works based on strategic sampling of sensors from a dense sensor network, change point analysis, and recursive Bayesian probability estimation. The contribution of this part is in developing a novel scalable single and multiple damage detection strategy to localize the structural damage accurately, while only a small portion of data is processed.

8.2. Future directions

While this dissertation contributes different approaches for vibration-based SHM research, as a result a wide range of research topics are also opened. This section describes possible future directions for continuation of the research presented in this dissertation. The following presents these future research ideas classified based on the related problem.

8.2.1. RS-based non-linear FEM updating

While this dissertation presents several examples of implementing the GRSMU algorithm for input-output non-linear model updating as well as output-only linear model calibration, one future direction for extending the application of this algorithm is to develop output-only GRSMU for non-linear model updating. This can be accomplished by including an input excitation estimation step or alternatively by performing the model calibration on short-term Fourier transforms of the time domain data. In addition, another future research direction is to implement GRSMU for model updating of structures with different sources of non-linearity than what assumed in this dissertation. Moreover, given availability of long-term monitoring data, the overall GRSMU framework can be extended to develop RS functions of structural parameters as well as environmental factors such as temperature. This would be beneficial to establish an efficient on-line damage detection algorithm.

8.2.2. Data-driven Damage detection

This dissertation presents a comprehensive comparison of the performance of several data-driven damage localization techniques on a scaled steel frame under impact loading. Implementation of these damage detection frameworks on in-service real world structures by measuring their ambient vibration would provide a more realistic comparison of the performance of these techniques. In effect, this can be readily accomplished using the graphical toolsuit developed in Lehigh University's SHM research group. This toolsuite is available for download at http://dit.atlss.lehigh.edu (Shahidi et al, 2015b).

8.2.3. Damage detection with a compressed sensing approach

Compressed sensing and its application in SHM is relatively a new research topic. Therefore, several future directions are possible to take for further research in this area. One direction for future research is to study the effects of sensor network resolution on the accuracy of the proposed CS algorithm. Moreover, performance of other damage sensitive features, global or local sampling techniques, and likelihood models can be further studied. Finally, one could develop CS-based SHM algorithms with compression in terms of data transmission as well as sensor location selection.

References

Alvandi, A., Cremona, C. (2006). Assessment of vibration-based damage identification techniques, Journal of Sound and Vibration 292, 179–202.

Amiri, A. and Allahyari, S. (2011). Change point estimation methods for control chart post signal diagnostics: a literature review. Quality and Reliability Engineering International. 28, 637–685.

ASTM Standard C615/C615M-11, (2011). Standard Specification for Granite Dimension Stone, ASTM International, West Conshohocken, PA, DOI: 10.1520/C615_C615M-11.

ASTM Standard C503/C503M-10, (2010). Standard Specification for Marble Dimension Stone, ASTM International, West Conshohocken, PA, DOI: 10.1520/C0503_C0503M-10.

ASTM Standard C476-10, (2010). Standard Specification for Grout for Masonry, ASTM International, West Conshohocken, PA, DOI:10.1520/C0476-10.

Balageas, D. (2006). Introduction to Structural Health Monitoring. Structural Health Monitoring. Chapter 1: 13-43. ISTE, California.

Bao, Y., Li, H., Sun, X., Yu, Y., and Ou, J. (2013). Compressive sampling–based data loss recovery for wireless sensor networks used in civil structural health monitoring. Structural Health Monitoring, 12(1), 78-95.

Baruch, M. (1978). Optimization procedure to correct stiffness and flexibility matrices using vibration tests. AIAA J., 16(11), 1208–1210.

Baruch, M. (1984). Methods of reference basis for identification of linear dynamic structures. AIAA J., 22(4), 561-564.

Bell, E., Sanayei, M., Javdekar, C., and Slavsky, E. (2007). Multiresponse parameter estimation for finite element model updating using nondestructive test data. Journal of Structural Engineering, 133(8), 1067–1079.

Berman, A, and Nagy, E. J. (1983). Improvement of a large analytical model using test data. AIAA J., 21(8), 1168-1173.

Bodeux, J. and Golinval, J. (2003). Modal identification and damage detection using the data-driven stochastic subspace and ARMAV methods. Mechanical Systems and Signal Processing, 17 (1) 83–89

Box, G. E. P., and Draper, N. R. (1987). Empirical model-building and response surfaces. Wiley, New York.

Brownjohn, J. M.W., and Xia, P. (2000). Dynamic assessment of curved cable-stayed bridge by model updating. Journal of Structural Engineering ,126(2), 252-260.

Brownjohn, J. M. W., Xia, P., Hao, H., and Xia, Y. (2001). Civil structure condition assessment by finite element model updating: methodology and case studies. Finite Elements in Analysis and Design, 37(10):761–775.

Carpinteri, A., Lacidogna, G., and Niccolini, J. (2011). Damage analysis of reinforced concrete buildings by the acoustic emission technique. Structural Control and Health Monitoring, 18(6), 660-673.

Casey, T. L. (1885). Completion of Washington's Monument, Scientific American Supplement Vol. 19, March 7, 7650–7651.

Celik O, Ellingwood B. (2009). Seismic risk assessment of gravity load designed reinforced concrete frames subjected to Mid-America ground motions. Journal of Structural Engineering, 135(4):414–24

Celik O, Ellingwood B. (2009). Seismic risk assessment of gravity load designed reinforced concrete frames subjected to Mid-America ground motions. Journal of Structural Engineering, 135(4):414–24

Cruz, P.J.S. and Salgado, R. (2009). Performance of vibration-based damage detection methods in bridges. Computer-Aided Civil and Infrastructure Engineering 24 (1) 62-79.

Cundy, A. L. (2002). Use of response surface metamodels in damage identification of dynamic structures. M. S. Thesis. Virginia Polytechnic Institute and State University, Blacksburg, VA, USA.

Chang, M., and Pakzad, S.N. (2014). Observer Kalman filter identification for output-only systems using Interactive Structural Modal Identification Toolsuite (SMIT), Journal of Bridge Engineering , 19(5), 04014002.

Computer and Structures, Inc. (2010). CSI Analysis Reference Manual for SAP2000 (Version 14.2.4).

Dassault Systèmes, 2013, ABAQUS Documentation (Version 6.13), Providence, RI, USA.

De Sortis, A., Antonacci, E., and Vestroni, F. (2005) Dynamic identification of a masonry building using forced vibration tests: Engineering Structure, v. 27, 155–165.

Deng, L. and Cai, C. S. (2010). Bridge model updating using response surface method and genetic algorithm, Journal of Bridge Engineering, 15(5), 553–64.

De Lautour, O. R., and Omenzetter, P. (2010). Nearest neighbor and learning vector quantization classification for damage detection using time series analysis. Structural Control and Health Monitoring 17(6), 614–631.

Deraemaeker, A. and Preumont A. (2006). Vibration based damage detection using large array sensors and spatial filters. Mechanical Systems and Signal Processing, 20,1615–1630.

Doebling, S. W., Farrar, C. R., and Prime, M. B. (1998). A Summary Review of Vibration-based Damage Identification Methods. Shock and Vibration Digest, 30(2), 91–105.

Dorvash, S., Pakzad, S. N., Naito, C. J., Yen, B., Hodgson, I. C., (2012). Application of state of the art in measurement and data analysis techniques for vibration evaluation of a tall building, Journal of Structure and Infrastructure Engineering, 10(5) 654-669.

Dorvash, S., Pakzad, S. N. and Cheng L. (2013a) An iterative modal identification algorithm for structural health monitoring using wireless sensor networks. Earthquake Spectra. 9(2), 339-365.

Dorvash, S., Pakzad, S.N., Labuz, E., Chang, M., Lib, X., Cheng, L. (2010). Validation of a wireless sensor network using local damage detection algorithm for beam-column connections. Proc. of SPIE Vol 7674 76719-1

Dorvash, S., Pakzad, S.N., and Labuz, E.L. (2013b). Statistics based localized damage detection using vibration response. Smart Structures and Systems, An International Journal, 14(2), 85-104.

Dorvash, S., Pakzad, S.N., Labuz, E.L., Ricles, J.M., and Hodgson, I.C. (2013c). Localized damage detection algorithm and implementation on a large-scale steel beam-to-column moment connection. Earthquake Spectra, 31(3), 1543-1566.

Ellingwood, B. R., Celik, O. C. , and Kinali, K. (2007). Fragility assessment of building structural systems in mid-America. Earthquake Engineering and Structural Dynamics 36:1935–1952.

Ellingwood, B.R., and Tekie, P.B. (2001). Fragility analysis of concrete gravity dams. Journal of Infrastructure Systems 7(2), 41–48.

El-Ouafi Bahlous, S., Abdelghani, M., Smaoui, H. and El-Borgi, S. (2007). A modal filtering and statistical approach for damage detection and diagnosis in structures using ambient vibrations measurements. Journal of Vibration and Control, 13(3), 281-308.

Farrar, C. R., Baker, W. E., Bell, T. M., Cone, K. M., Darling, T. W., Duffey, T. A., Eklund, A., and Migliori, A. (1994). Dynamic characterization and damage detection in the I-40 bridge over the Rio Grande. Los Alamos National Laboratory Report LA-12767-MS.

Fang, S. E., and Perera, R. (2009). A response surface methodology-based damage identification technique." Smart Materials and Structures, 18(6), 065009.

Federal emergency management agency. (2000). Prestandard and commentary for the seismic rehabilitation of buildings, Washington, D.C.

Federal Emergency Management Agency. (2012). Multi-hazard loss estimation methodology, Earthquake model. HAZUS-MH2.1 Technical Manual, Washington, D.C.

Friswell, M. I., Inman, D. J., and Pilkey, D. F. (1998). The direct updating of damping and stiffness matrices. AIAA J., 36(3), 491-493.

Friswell, M. I. and Mottershead, J. E. (1995). Finite element model updating in structural dynamics. Kluwer Academic Publishers, Dordrecht, the Netherlands.

Fugate, M.L., Sohn, H. and Farrar, C.R. (2001). Vibration-based damage detection using statistical process control. Mechanical Systems and Signal Processing 15, 707-721

Figueiredo, E., Figueiras, J., Park, G., Farrar, C.R. and Worden, K. (2011). Influence of the autoregressive model order on damage detection. Computer-Aided Civil and Infrastructure Engineering 26 225-238

Friedlander, B. and Porat, B. (1984). Modified Yule-Walker method of ARMA spectral estimation. IEEE Transactions on Aerospace and Electronic Systems, AES-20 (2), 158-173

Gentile, C., and Saisi, A. (2007). Ambient vibration testing of historic masonry towers for structural identification and damage assessment: Construction and Building Materials, 21, 1311–1321.

Gul, M., and Catbas, F. (2011). Damage assessment with ambient vibration data using a novel time series analysis methodology. Journal of Structural Engineering-ASCE , 137(12),1518–1526.

Guo, Q. T., and Zhang, L. M. (2004). Finite element model updating based on response surface methodology. Proc., IMAC-XXII: Conference and Exposition on Structural Dynamics , SEM, Dearborn, MI, USA.

Hawkins, D.M. and Zamba, K.D. (2005). Statistical process control for shifts in mean or variance using a change point formulation. Technometrics, 47(2), 164-173.

Haile, M., & Ghoshal, A. (2012). Application of compressed sensing in full-field structural health monitoring. Proc. SPIE 8346, Smart Sensor Phenomena, Technology, Networks and Systems Integration, San Diego, CA.

He, X. and De Roeck, G. (1997). System identification of mechanical structures by a high-order multivariate autoregressive model. Computers and Structures 64 (1–4), 341–351.

Heinonen, O., and Pajunen, S. (2011). Optimal design of stiffened plate using metamodeling techniques. Journal of Structural Mechanics, 44(3), 218-230.

Historic American Engineering Record. (1986). Washington Monument, Fifteenth Street between Independence & Constitution, Washington, District of Columbia, DC, Library of Congress: http://www.loc.gov/pictures/item/dc0968/

Hua, X., Ni, Y., Chen, Z., and Ko, J. (2009). Structural Damage Detection of Cable-Stayed Bridges Using Changes in Cable Forces and Model Updating. Journal of Structural Engineering, 135(9), 1093–1106.

Hu, X.Y., Wang, B., and Ji, H. (2013). A wireless sensor network-based structural health monitoring system for highway bridges. Computer-Aided Civil and Infrastructure Engineering, 28(3), 193-209.

Huang, C.S. (2001). Structural identification from ambient vibration measurement using the multivariate AR model. Journal of Sound and Vibration 241 (3), 337–359.

Hung, C.F., Ko, W.J., Peng, Y.T. (2004). Identification of modal parameters from measured input and output data using a vector backward auto-regressive with exogeneous model. Journal of Sound and Vibration 276 (3–5), 1043–1063.

Imregun, M., and Visser, W. J. (1991). A review of model updating techniques. Shock and Vibration Digest, 23(1), 9-20.

Jaishi, B., and Ren, X. W. (2007). Finite element model updating based on eigenvalue and strain energy residuals using multiobjective optimization technique. Mechanical Systems and Signal Processing, 21(5), 2295-2317.

Jaishi, B., Ren, W. X. (2006). Damage detection by finite element model updating using modal flexibility residual. Journal of Sound and Vibration, 290, 369–387.

Jang, S., Spencer, B. F., Rice J.A., and Wang, J. (2011). Full-scale experimental validation of high fidelity wireless measurement using a historic truss bridge. Advances in Structural Engineering, 14(1), 93-101.

Johnson, R. A., and Bhattacharyya, G. K. (2009). Statistics: principles and methods. Wiley, New York.

John Milner Associates, Inc. (2004). Washington Monument and Associated Structures Historic Structure Report. National Park Service: http://www.nps.gov/history/history/online_books/wamo/wash_hsr1.pdf

Kariya, T., and Karuta H. (2004). Generalized least Squares. Wiley, New York.

Kim, C. W. and Kawatani, M. (2008). Pseudo-static approach for damage identification of bridges based on coupling vibration with a moving vehicle. Structure

and Infrastructure Engineering: Maintenance, Management, Life-Cycle Design and Performance, 4:5, 371-379,

Kim, S, Pakzad, S.N., Culler, D., Demmel, J., Fenves, G., Glaser, S., and Turon, M. (2007) Health monitoring of civil infrastructures using wireless sensor networks. In Proc. of the 6th International Conference on Information Processing in Sensor Networks (IPSN)

Kiremidjian, A. S. , Kiremidjian, G., and and Sarabandi, P. (2011). A wireless structural monitoring system with embedded damage algorithms and decision support system. Structure and Infrastructure Engineering: Maintenance, Management, Life-Cycle Design and Performance, 7(12), 881-894.

Kumar, R. P., Oshima, T., Mikami, S. , Miyamori, Y. and Yamazaki, T. (2012). Damage identification in a lightly reinforced concrete beam based on changes in the power spectral density. Structure and Infrastructure Engineering: Maintenance, Management, Life-Cycle Design and Performance, 8(8), 715-727

Labuz, E.L., Chang, M. and Pakzad, S.N. (2010). Local Damage Detection in Beam-Column Connections Using a Dense Sensor Network, Proceedings of the ASCE's 42nd Structures Congress. Orlando, FL. 3143-3154.

Labuz, E. L., Pakzad, S.N., and Wurst, D. (2011). Localized damage detection in a large-scale moment connection using a strain gauge sensor network, Proceedings of the SPIE Sensors and Smart Structures Technologies, San Diego, CA. Vol. 7981 79813Q-1.

Lloyd, S. P. (1982). Least Squares Quantization in PCM, IEEE Trans, Information Theory, 28(2), pp. 129-137.

Lu, Y. and Gao, F. (2005). A novel time-domain auto-regressive model for structural damage diagnosis. Journal of Sound and Vibration, 283,1031–1049.

Lynch, J. P., and Kenneth, J. L. (2006) A summary review of wireless sensors and sensor networks for structural health monitoring. Shock and Vibration Digest, 38(3), 91–128.

Lynch, J. P., Sundararajan, A., Law, K. H., Kiremidjian, A.S., Kenny, T., Carryer, E. (2003). Embedment of structural monitoring algorithms in a wireless sensing unit. Structural Engineering and Mechanics, 15(3), 285–297.

Lynch, J. P., Wang, Y., Loh, K., Yi, J. H., and Yun, C. B. (2006). Performance monitoring of the Geumdang bridge using a dense network of high-resolution wireless sensors. Smart Materials and Structures, 15(6), 1561–1575.

Matarazzo, T.J., Shahidi, S.G., Chang, M., and Pakzad, S.N. (2015). Are Today's SHM Procedures Suitable for Tomorrow's Data?, Proceedings of the Society of Experimental Mechanics IMAC XXXIII, Orlando, FL.

Magalhães, F., Cunha, A., and Caetano, E. (2012). Vibration based structural health monitoring of an arch bridge: From automated OMA to damage detection, Mechanical Systems and Signal Processing, 28, 212-228.

Marwala, T., (2004). Finite element model updating using response surface method. Collection of Technical papers—AIAA/ASME/ASCE/AHS/ASC structures, structural dynamics and materials conference, 7, 5165–5173.

Marwala, T., (2010), Finite Element Model Updating Using Computational Intelligence Techniques: Applications to Structural Dynamics, Heidelberg: Springer.

Mascarenas, D., Cattaneo, A., Theiler, J., and Farrar, C. (2013). Compressed sensing techniques for detecting damage in structures. Structural Health Monitoring, 12(4), 325-338.

Mazzoni, S., Mckenna, F., Scott, M. H., and Fenves, G. (2009). OpenSees command language manual. Pacific Earthquake Engineering Research Center.

McGuire, R. K., Silva, W. J., and Constantino, C. J. (2001) Technical basis for revision of regulatory guidance on design ground motions, Rpt. NUREG/CR-6728, U.S. Nuclear Regulatory Commission.

Moaveni, B., Stavridis, A., Lombaert, G., Conte, J. P., Shing, P. B. (2012). Finite element model updating for assessment of progressive damage in a three-story infilled RC frame. Journal of Structural Engineering.

Moaveni, B., and Behmanesh, I. (2012). Effects of changing ambient temperature on finite element model updating of the Dowling Hall Footbridge. Engineering Structures, 43(10), 58-68.

Montgomery, R.H. and Loftis, J.C. (1987). Applicability of the t-test for detecting trends in water quality variables. American Water Resources Association 23 (4) 653-662.

Montgomery, D. C. (2001). Design and analysis of experiments. Wiley, New York.

Montgomery, D. C., Peck, E. A., and Vining, G. G. (2004). Introduction to linear regression analysis. Wiley, New York.

Mosavi, A. A., Dickey, D., Seracino, R. Rizkalla, S. (2012). Identifying damage locations under ambient vibrations utilizing vector autoregressive models and mahalanobis distances. Mechanical Systems and Signal Processing, 26, 254-267.

Mottershead, J. E., Link, M., and Friswell , M. I. (2010). The sensitivity method in finite element model updating: a tutorial. Mechanical Systems and Signal Processing, 25(7), 2275–2296.

Nair, K. K., Kiremidjian, A.S. and Law, K.H. (2006). Time series-based damage detection and localization algorithm with application to the ASCE benchmark structure. Journal of Sound and Vibration, 291(2) 349–368.

Nigro, M.B., Pakzad, S.N. and Dorvash, S. (2014), Localized Structural Damage Detection: A Change Point Analysis. Computer-Aided Civil and Infrastructure Engineering. DOI: 10.1111/mice.12059

Nocedal, J., and Wright, S. J. (2006). Numerical Optimization. Springer, New York.

Noh, H.Y., Nair K.K., Kiremidjian, A.S., and Loh C.H. (2009). Application of time series based damage detection algorithms to the Benchmark experiment at the National Center for Research on Earthquake Engineering (NCREE) in Taipei, Taiwan. Smart Structures and Systems, 5(1), 95–117.

Oehrlein and Associates architects. (1993). Evaluation of the Washington Monument, National Park Service:

http://parkplanning.nps.gov/document.cfm?parkID=427&projectID=31299&documentID=43344

O'Connor, S. M., Lynch, J. P., & Gilbert, A. C. (2014). Compressed sensing embedded in an operational wireless sensor network to achieve energy efficiency in long-term monitoring applications. Smart Materials and Structures, 23(8), 085014.

Paret, T.F., Rosenboom, O.A., Panian, L., Korolyk, M., Egan, J., Wells, D., Murphy., D. (2014). Seismic Vulnerability of the Washington Monument. Proceedings of the 10th National Conference in Earthquake Engineering, Earthquake Engineering Research Institute, Anchorage, AK.

Pakzad, S.N. (2010). Development and deployment of large scale wireless sensor network on a long-span bridge. Smart Structures and Systems, 6(5-6), 525-543.

Pandey, A. K. and Biswas, M. (1995). Damage diagnosis of truss structures by estimation of flexibility change. Modal Analysis – The International Journal of Analytical and Experimental Modal Analysis, 10 (2), 104-117.

PEER Ground Motion Database (2013), Pacific Earthquake Engineering Research Center, <http://peer.berkeley.edu/products/strong_ground_motion_db.html>.

Ren, W., and Chen, H. (2010). Finite element model updating in structural dynamics by using the response surface method. Engineering Structures 32(8), 2455-2465.

Ren, W., Fang, S., and Deng, M. (2011). Response surface-based finite element model updating using structural static responses. Journal of Engineering Mechanics (ASCE), 137(4), 248-257.

Ribeirio, D., Calcada, R., Delgado, R., Brehm, M., and Zabel, V. (2012). Finite element model updating of a bowstring-arch railway bridge based on experimental modal parameters. Engineering Structures, 40(7), 413-435.

Roux, W. J., Stander , N., and Haftka, R. T. (1998). Response surface approximation for structural optimization. International Journal of Numerical Methods Engineering, 42(3), 517-534.

Schultze, J. f. , Hemez, F. M., Doebling, S. W., and Sohn, H. (2001). Application of non-linear system model updating using feature extraction and parameter effect analysis. Shock and Vibration, 8, 325-337.

Scott, M.H., Fenves, G.L. (2010). Krylov Subspace Accelerated Newton Algorithm: Application to Dynamic Progressive Collapse Simulation of Frames. Journal of Structural Engineering, 136, 473–480.

Silva, S., Cogan, S., Foltete, E., and Buffe, F. (2009). Metrics for non-linear model updating in mechanical systems. Journal of the Brazilian Society of Mechanical Sciences and Engineering, 31(1), 27–34.

Shahidi, S.G. and Pakzad, S.N. (2014a). Generalized Response Surface Model Updating Using Time Domain Data, Journal of Structural Engineering. 140, SPECIAL ISSUE: Computational Simulation in Structural Engineering, A4014001.

Shahidi, S.G., and Pakzad, S.N. (2014b). Effect of Measurement Error and Excitation on Generalized Response Surface Model Updating, Engineering Structures, 75, 51-62.

Shahidi, S. G., Nigro, M.B., Pakzad, S.N., and Pan, Y. (2014). Structural damage detection and localization using multivariate regression models and two-sample control statistics, Structure and Infrastructure Engineering: Maintenance, Management, Life-Cycle Design and Performance, 11(10), 1277–1293.

Shahidi, S.G., Pakzad, S.N., Ricles, J.M., Martin, J.R., Olgun, C.G., and Godfrey, E.A. (2015a) Behavior and damage of the Washington Monument during the 2011 Mineral, Virginia, earthquake, Geological Society of America, Special Paper volume on The 2011 Mineral, Virginia, Earthquake, and Its Significance for Seismic Hazards in Eastern North America.

Shahidi, S.G., Yao, R., Chamberlain, M.B.W., Nigro, M.B., Thorsen, A., and Pakzad, S.N. (2015b). Data-driven Structural Damage Identification Using DIT, Proceedings of the Society of Experimental Mechanics IMAC XXXIII, Orlando, FL.

Shinozuka M., Feng M. Q., Lee J., Naganuma T. (2000). Statistical analysis of fragility curves, Journal of Engineering Mechanics, 126, 1224–1231.

Srivastava, M.S., and Worsley, K.J. (1986). Likelihood ratio tests for a change in the multivariate normal mean. Journal of the American Statistical Association, 81 (393), 199-204.

Sohn, H., Farrar, C.R., Hunter, N.F. and Worden, K. (2001). Structural Health Monitoring Using Statistical Pattern Recognition Techniques. ASME Journal of Dynamic Systems, Measurement and Control: Special Issue on Identification of Mechanical Systems, 123(4), 706–711.

Sullivan, J.H. and Woodall, W.H. (1996). A control chart for a preliminary analysis of individual observations. Journal of Quality Technology, 28(3), 265–278.

The Washington Post (July 9, 2012), Monumental damage, GRAPHIC: Rivero, C., SOURCE: National Park Service: http://www.washingtonpost.com/local/monumentaldamage/2012/07/09/gJQAac3FZW_graphic.html

Trimm, M. (2003). An overview of nondestructive evaluation methods. Journal of Failure Analysis and Prevention 3(3), 17-31.

Thrun, S., Burgard, W., and Fox, D. (2005). Probabilistic robotics. MIT press.

Wang, H., Li, A., Li, J. (2010). Progressive finite element model calibration of a long-span suspension bridge based on ambient vibration and static measurements. Engineering Structures, 32(9), 2546–2556.

Weber, B. and Paultre, P. (2010). Damage Identification in a Truss Tower by Regularized Model Updating. Journal of Structural Engineering, 136(3), 307–316.

Welch, B.L. (1974). The generalization of 'Student's' problem when several different population variances are involved. Biometrika 34(1–2), 28–35.

Welch, P.D. (1967). The use of fast Fourier transform for the estimation of power spectra: A method based on time-averaging over short, modified periodograms, IEEE Transactions on Audio Electroacoustics, v. AU-15, 70–73.

West, W. M. (1984). Illustration of the use of modal assurance criterion to detect structural changes in an orbiter test specimen. Proceedings of Air Force Conference on Aircraft Structural Integrity, 1–6

Wiss, Janney, Elstner Associates, Inc., and Tipping Mar, (2011), Washington Monument post-earthquake assessment. National Park Service:

http://www.nps.gov/wamo/upload/Post-Earthquake-assessment12_22_logo.pdf

Wilcox, M. (2003). The philosophy of shewhart's theory of prediction. Proceedings of the 9th research seminar: Deming scholar's program, New York.

Whelan, M. J., and Janoyan, K. D. (2009). Design of a robust, high-rate wireless sensor network for static and dynamic structural monitoring. Journal Of Intelligent Material Systems And Structures, 20(7), 849-864.

Yao, R. and Pakzad, S.N. (2012). Autoregressive statistical pattern recognition algorithms for damage detection in civil structures. Mechanical Systems and Signal Processing, 31, 355-368.

Yao, R. and Pakzad, S.N. (2013). Performance comparison of different autoregressive damage features using acceleration measurements from a truss bridge. International Workshop on Structural Health Monitoring, Stanford University, CA, USA.

Yao, R., Pakzad, S. N., Venkitasubramaniam, P., & Hudson, J. M. (2015). Iterative Spatial Compressive Sensing Strategy for Structural Damage Diagnosis as a BIG DATA Problem. In Dynamics of Civil Structures, 2, 185-190). Springer International Publishing.

Yang, Y. B., and Chen, Y. J. (2009). A new direct method for updating structural models based on measured modal data. Engineering Structures, 31(1), 32-42.

Yehia, S., Abudayyeh, O., Nabulsi, S., & Abdelqader, I. (2007). Detection of common defects in concrete bridge decks using nondestructive evaluation techniques.‖ Journal of Bridge Engineering, 12(2), 215-225.

Zamba, K.D. and Hawkins, D. M. (2006). A multivariate change-point model for statistical process control. Technometrics, 48, 539–549

Zaurin, R., and Catbas, F. N. (2010). Integration of computer imaging and sensor data for structural health monitoring of bridges. Smart Materials and Structures, 19(1), 015019.

Zhang, J., Zou, C., and Wang, Z. (2010). A control chart based on likelihood ratio test for monitoring process mean and variability. Quality and Reliability Engineering International, 26, 63-73.

Zhang, L. M., and Guo, Q. T.(2007). A case study of model updating and validation of a frame structure with highly non-linear component. Proc., IMAC-XXV: Conference and Exposition on Structural Dynamics, SEM, Orlando, FL, USA.

Zhang, L. M., Fei, Q., and Guo, Q. T. (2005). Dynamic finite element model updating using meta-model and genetic algorithm. Proc., IMAC-XXIII: Conference and Exposition on Structural Dynamics, SEM, Orlando, FL, USA.

Zhang, Q. W., Chang, C. C., and Chang, T. Y. P. (2000). Finite element model updating for structures with parametric constraints. Earthquake Engineering & Structural Dynamics, 29(7), 927–944.

Zheng, H., and Mita, A. (2007) Two-stage damage diagnosis based on the distance between ARMA models and pre-whitening filters. Smart Materials and Structures, 16, 1829–1836

Zheng, H., and Mita, A. (2009). Localized damage detection of structures subject to multiple ambient excitations using two distance measures for autoregressive models. Structural Health Monitoring, 8(3), 207–222.

Zhou, S., Bao, Y., & Li, H. (2013). Structural damage identification based on substructure sensitivity and l1 sparse regularization. In SPIE Smart Structures and Materials+ Nondestructive Evaluation and Health Monitoring (86923N-86923N). International Society for Optics and Photonics.

Zhou, Q., Luo, Y., Wang, Z. (2010). A control chart based on likelihood ratio test for detecting patterned mean and variance shifts. Computational Statistics and Data Analysis, 54, 1634-1645.

Zimmerman, A. T., and Lynch, J. P. (2009). A parallel simulated annealing architecture for model updating in wireless sensor networks. IEEE Sensors journal, 9(10), 1503-1510.

Zona, A., Barbato, M., and Fragiacomo, M. (2012). Finite element model updating and probabilistic analysis of timber-concrete composite beams. Journal of Structural Engineering,138(7), 899–910.

Zou, C., Zhang, Y., Wang, Z. (2006). A control chart based on a change-point model monitoring linear profiles. IIE Transactions 38(12), 1093-1103.

Vita

Golnaz Shahidi was born in Teharn, Iran on September 11, 1984. In 2006, she earned a B.Sc in Civil Engineering from Iran University of Science & Technology in Teharn, Iran. In 2009, she graduated from Sharif University of Technology, in Tehran, Iran with a M.Sc in Earthquake Engineering. Golnaz began her PhD studies in the Department of Civil and Environmental Engineering at Lehigh University in Bethlehem, PA in the fall of 2010. She will receive her PhD in Structural Engineering in May 2016.